NASA CR-121112
PWA[TM] - 4712

(NASA-CR-121112) APPLICATION OF HOLOGRAPHY TO THE DETERMINATION OF FLOW CONDITIONS WITHIN THE ROTATING BLADE ROW OF A COMPRESSOR (Pratt and Whitney Aircraft) 114 p HC $7.75 CSCL 20D G3/12 N73-27215 Unclas 09449

APPLICATION OF HOLOGRAPHY TO THE DETERMINATION OF FLOW CONDITIONS WITHIN THE ROTATING BLADE ROW OF A COMPRESSOR

FINAL REPORT

JULY 1973

By

R. G. Hantman, R. J. Burr
W. G. Alwang, M. C. Williams

PRATT & WHITNEY AIRCRAFT DIVISION
UNITED AIRCRAFT CORPORATION

prepared for

NATIONAL AERONAUTICS AND SPACE ADMINISTRATION

NASA Lewis Research Center
Contract NAS3-15340
T. F. Gelder, Project Manager
Fluid System Components Division

1. Report No.	2 Government Accession No.	3. Recipient's Catalog No.
CR-121112		
4. Title and Subtitle Application of Holography to the Determination of Flow Conditions Within the Rotating Blade Row of a Compressor		5 Report Date July 1973 6. Performing Organization Code
7. Author(s) R. G. Hantman, R. J. Burr, W. G. Alwang and M. C. Williams		8. Performing Organization Report No. PWA[TM]-4712 10. Work Unit No.
9. Performing Organization Name and Address Pratt & Whitney Aircraft Division United Aircraft Corporation East Hartford, Connecticut 06108		11. Contract or Grant No. NAS 3-15340 13. Type of Report and Period Covered Contractor Report
12. Sponsoring Agency Name and Address National Aeronautics and Space Administration Washington, D. C. 20546		14. Sponsoring Agency Code
15. Supplementary Notes Prepared in Cooperation with T. F. Gelder, Program Manager, Fluid System Components Division NASA-Lewis Research Center, Cleveland, Ohio		

16. Abstract

The double-pulse, double-exposure holography technique was applied to visualize the flow field within a transonic compressor rotor with a tip speed of 1800 ft/sec. The principal objective was to visualize the shock waves created in the flow field which was supersonic relative to the rotating blade row. The upstream rotor blade bow shocks and, at high speed, the outermost portion of the leading edge passage shock were successfully observed in the holograms. Techniques were devised for locating these shocks in three dimensions, and the results were compared with theoretical predictions. Density changes between the two pulses due to motion of the shocks were large and, therefore, it was not possible to resolve the fringe systems in detail for the 100% speed conditions. However, gross features of the shocks were easily observed, and the upstream shocks were well displayed. In all cases the shock angles were somewhat larger than predicted by theory, and a distinct increase in angle near the outer wall was observed, which may be attributed to endwall boundary layer effects. The location and orientation of the observed leading edge passage shocks were in good agreement with static pressure contours obtained from measurements in the outer casing over the rotor tip.

17 Key Words (Suggested by Author(s))	18. Distribution Statement
Holographic Flow Visualization Transonic Compressor Stage Shocks in Rotor	Unclassified - Unlimited

19. Security Classif. (of this report)	20. Security Classif. (of this page)	21. No. of Pages	22. Price*
Unclassified	Unclassified	114	3.00

* For sale by the National Technical Information Service, Springfield, Virginia 22151

NASA C-168 (Rev 6-71)

PRECEDING PAGE BLANK NOT FILMED

TABLE OF CONTENTS

	Page
SUMMARY	1
INTRODUCTION	1
APPARATUS AND PROCEDURES	2
A. TEST FACILITIES AND TEST COMPRESSOR	2
1. General Description of Test Rig	2
2. Rig Design Changes Required for Holography	4
B. HOLOCAMERA DESIGN AND CONSTRUCTION	5
1. General Description	5
2. Optical System Layout	5
3. FTIR Q. Switch	6
4. Other System Components	7
C. DESCRIPTION OF BENCH TESTS	7
1. FTIR Q-Switch	7
2. Bench Model	8
3. Laser Coherence Characteristics	8
4. Sensitization of Photographic Plates	9
D. HOLOGRAPHIC TEST PROCEDURE WITH COMPRESSOR	9
1. Shakedown Tests	9
2. Final Tests	10
OPTICAL ANALYSIS OF HOLOGRAMS	11
A. DESCRIPTION OF SUCCESSFUL HOLOGRAMS	11
B. ANALYTICAL METHODS OF FRINGE LOCALIZATION	12
AERODYNAMIC INTERPRETATION FROM ANALYSIS OF HOLOGRAMS	15
A. INTRODUCTION	15
B. DESCRIPTION AND ASSUMPTIONS	15
C. AERODYNAMIC ANALYSIS OF HOLOGRAMS TAKEN AT 100% SPEED	18
1. Shock Patterns at Maximum and Near Stall Flows	18
2. Comparison of Holographic Data With Blade Element Data and Rotor Tip Static Pressure Contours	19
D. AERODYNAMIC ANALYSIS OF HOLOGRAMS TAKEN AT 70% DESIGN SPEED	20
1. Shock Pattern at Intermediate and Near Stall Flows	20
2. Comparison of Holographic Data With Blade Element Data and Rotor Tip Static Pressure Contours	21
E. OTHER AERODYNAMIC DISCUSSION	22
SUMMARY OF RESULTS	23

TABLE OF CONTENTS (Cont'd)

	Page
APPENDIX I – SYMBOLS AND PERFORMANCE PARAMETER DEFINITIONS	25
1-a SYMBOLS	26
1-b PERFORMANCE PARAMETERS	31
APPENDIX II – BLADE ELEMENT AND OVERALL PERFORMANCE WITH UNIFORM INLET FLOW	35
APPENDIX III – THEORY OF HOLOGRAPHIC FLOW VISUALIZATION	43
A. INTRODUCTION	43
B. INTERPRETATION OF FRINGES IN HOLOGRAPHIC INTERFEROMETRY OF GAS FLOWS	44
1. Homologous Rays	44
2. Superposition of Plane Waves	45
C. LOCALIZATION PROBLEMS	48
1. Localization By Depth of Field	48
2. Localization of Fringes by Triangulation	48
3. Localization of Regions of Abrupt Density Changes by Triangulation	49
4. Summary of Optical Effects	49
APPENDIX IV – DETERMINATION OF VIEWING PARAMETERS AND THE DERIVATION OF THE TRIANGULATION EQUATIONS	50
A. METHOD OF DETERMINING VIEWING PARAMETERS	50
B. DETERMINATION OF THE COMMON POINT COORDINATE POSITIONS	51
C. DERIVATION OF THE TRIANGULATION EQUATIONS	51
APPENDIX V – SAMPLE CALCULATIONS AND ERROR ANALYSIS	54
A. SAMPLE CALCULATIONS	54
B. ERROR ANALYSIS	56
APPENDIX VI – PLANE RECONSTRUCTION OF SHOCK WAVES FROM THE HOLOGRAPHIC ANALYSIS	59
REFERENCES	61
ILLUSTRATIONS	65
DISTRIBUTION LIST	101

LIST OF ILLUSTRATIONS

Figure	Caption	Page
1	Optical Paths in the Transonic Fan Rig	65
2	Photograph of Fan Rig Exterior Without Viewing Window	66
3	Optical Configuration of Holocamera (Fresnel Configuration)	67
4	Optical Configuration of Holocamera (Bragg Configuration)	67
5	FTIR Q-Switch Mechanism	68
6	Schematic of Holographic Plate Transport System	68
7	Block Diagram of Holography System	69
8	Wiring Diagram for the FTIR Q-Switch Electronics	70
9	Rotor Assembly Used for Bench Tests	71
10	Single Pulse Shapes from Q-Switched Pulse Lasers	71
11	Hologram Views of Bench Model	72
12	Window Damage	73
13	Window Damage	73
14	Interior of NASA Fan Rig as Seen Without Window in Place	74
15	Interior of NASA Fan Rig as Seen With Window in Place	75
16	Photograph of the Reconstructed Image of Hologram #8	76
17	Photograph of the Reconstructed Image of Hologram #13	76
18	Photographs of the Reconstructed Image of Hologram #1	77
19	Photograph of the Reconstructed Image of Hologram #3	78

LIST OF ILLUSTRATIONS (Cont'd)

20	Photographs of the Reconstructed Image of Hologram #21	79
21	Meridional View of Compressor	80
22	The X-Axis and Z-Axis as Defined on the Window	81
23	Coordinate System and Geometry Used in Triangulation Procedure	82
24	Stage Overall Performance with Uniform Inlet Flov	83
25	Rotor Shock Patterns from Hologram 8, 70% Design Speed, Near Stall Flow	84
26	Projection of Included Angle from Conical to Radial Plane	84
27	Rotor Shock Patterns from Hologram 21, 100% Design Speed, Near Stall Flow	85
28	Rotor Shock Patterns from Holograms 1 and 3, 100% Design Speed, Maximum Flow	86
29	Rotor Blade Tip Static Pressure Contours, 100% Speed	87
30	Rotor Leading Relative Mach Number, Incidence, and Meridional Streamline Angle	88
31	Rotor Shock Patterns from Hologram 13, 70% Design Speed, Intermediate Flow	89
32	Rotor Shock Patterns from Hologram 13, 70% Design Speed, Intermediate Flow	90
33	Rotor Blade Tip Static Pressure Contours, 70% Speed	91
34	Simplified Diagram of Holographic Reconstruction of the Test Section	92
35	Picture of a Holographic Interferogram of a Flame	92
36	Ray Diagram	93
37	Principal Homologous Ray Diagram	93

LIST OF ILLUSTRATIONS (Cont'd)

38	Central Rays for Two Views Through the Tip of a Shock	94
39	Relative Positions of the Rig Window, Hologram, and Recording Camera; Geometric Relations of the Length Parameters (Appendix IV)	95
40	NASA Fan Rig, View Along Axis of Rotation	96
41	Coordinate System and Geometry Used in the Determination of the Triangulation Equations	97
42	Photographs of the Reconstructed Image of Hologram #13	98
43	Photographs of the Reconstructed Image of Hologram #21	99
44	Geometry Used for Plane Reconstruction of Shock Waves from the Holographic Analysis	100

LIST OF TABLES

Table	Caption	Page
1	Rotor Design Parameters	3
2	Stator Design Parameters	4
3	Comparison of Mach Angles Calculated From Blade Element Data and Corrected Mach Numbers According to Equation 3	17
4	Typical Variations of M′, B′ as a Function of Axial Distance Upstream of Rotor	17
5	Identification of Blade-Element Overall Performance Table Headings	36
6.1	Blade Element and Overall Performance Design	38
6.2 - 6.5	Blade Element and Overall Performance With Uniform Inlet	39

APPLICATION OF HOLOGRAPHY TO THE DETERMINATION OF FLOW CONDITIONS WITHIN THE ROTATING BLADE ROW OF A COMPRESSOR

FINAL REPORT

R. G. Hantman, R. J. Burr, W. G. Alwang, M. C. Williams
Pratt & Whitney Aircraft Division
United Aircraft Corporation

SUMMARY

The double-pulse, double-exposure holography technique was applied to visualize the flow field within a transonic compressor rotor with a tip speed of 1800 ft/sec. The rotor used in this investigation had been designed and tested under Contract NAS3-13493. The principal objective of this program was to visualize the shock waves created in the flow field which was supersonic relative to the rotating blade row. The only structural rig modification was the installation of two plastic windows in the outer casing of the rig which permitted viewing the flow just upstream of the rotor and a limited portion of the intrablade region outboard of a part span shroud. The inlet hub was painted white. The upstream rotor blade bow shocks and, at high speed, the outermost portion of the leading edge passage shock were successfully observed in the holograms. Techniques were devised for locating these shocks in three dimensions, and the results were compared with theoretical predictions. Density changes between the two pulses due to the motion of the shocks were large and therefore it was not possible to resolve the fringe systems in detail for the 100% speed conditions. However, gross features of the shocks were easily observed, and the upstream shocks were very well displayed. In all cases the shock angles were somewhat larger than predicted by theory, and a distinct increase in angle near the outer wall was observed, which may be attributed to endwall boundary layer effects. Although visualization of the intrablade region was limited by the geometry of the rig, the outer portion of the leading edge passage shock was clearly visible at the rotor design speed. The location and orientation of the observed leading edge passage shocks were in good agreement with static pressure contours obtained from measurements in the outer casing over the rotor tip. No unusual radial variation of the observed upstream bow wave structure was noted, aside from the apparent endwall effect.

INTRODUCTION

Optical visualization of flowing gases has played a major role in the development of compressor fluid mechanics. Methods such as the shadowgraph, Toepler schlieren, and Mach-Zehnder interferometer have contributed greatly to the present understanding of aerodynamics. While these classical methods are not, in general, applicable for use in advanced research compressor rigs, the advent of holography has produced new methods that can be utilized for visualization of flow within the complex geometries of these modern research rigs without many of the stringent optical requirements of older methods.

Holographic techniques for flow visualization have been under investigation at Pratt & Whitney Aircraft for several years. Work was conducted for the most part under Naval Air Systems Command (NASC) Contract N00019-69-0-0322 (Ref. 1). Under that contract, a holographic

camera had been built and successfully demonstrated. The holographic method investigated under the NASC contract, and utilized in the subject NASA program, was the double-exposure technique.

Double-exposure holographic interferograms can be obtained by producing a hologram under a non-flow condition and then making a second exposure with flow. While this approach is feasible for application in many cascades where much of the background remains stationary, it is not satisfactory for the more normal compressor test environment where portions of the rig are in motion and where vibration and thermal gradients produce changes in optical alignment between pulses. To avoid these difficulties, the system developed in Reference 1 utilized two exposures produced during flow and separated by a short time interval. Based on the results of the earlier program, it was decided that a time separation of less than ten microseconds was needed for the current program. The holograms produced by this method display the time-differences of the shocks and densities.

A holographic application to a transonic compressor rotor was conducted under NASA-Lewis Contract NAS3-15340. The objective of this program was to obtain double-pulse, double-exposure holograms to reveal features of the three-dimensional shock structure. A complete description of the holographic camera design, construction and operation is given. The optical method for analysis of the holograms is discussed in detail. Shock position and orientation with respect to the rotor blade at several spanwise locations are given. These results are compared with blade element data, static pressure contours in the outer casing over the rotor tip, and pertinent aerodynamic design principles.

APPARATUS AND PROCEDURES

A TEST FACILITIES AND TEST COMPRESSOR

1. General Description of Test Rig

This holographic application program utilized the research transonic compressor designed and tested by P&WA™ under NASA Contract NAS3-13493 (Ref. 2 and 3). As originally conceived the NAS3-13493 program did not anticipate the use of flow visualization, and minor modifications to the rig were required.

The test program was carried out in a sea-level compressor test facility. Air entered the compressor through a calibrated nozzle for flow measurements. A 72-foot straight section of 42-inch diameter pipe was run from the nozzle to a 90-inch diameter inlet plenum. Wire-mesh screen and an "egg-crate" structure were located midway through the plenum to provide a uniform pressure profile to the compressor. The compressor airflow was exhausted into a toroidal collector with valving to control throttling for the test compressor.

Design of the stage flowpath was guided by the aerodynamic objectives outlined in detail in the design report (Reference 2). The test compressor (Figure 1) was a single-stage, axial-flow design with no inlet guide vanes, thirty-eight rotor blades and sixty variable stagger-angle stator blades. The adjustable stators allowed the aerodynamic performance to be optimized as discussed in Reference 3. The stator-blade leading edge was 0.5 inches behind the

rotor trailing edge at the hub. Running tip-clearance was about 0.035 inch at the 1800 ft/sec design tip speed.

Rotor and stator aerodynamic designs are explained in Reference 2 and summarized below and in Appendix II, Table 6.1. (All symbols are defined in Appendix I.) The rotor blade consists of multiple-circular-arc sections from the hub to 32% span and precompression sections from 37% span to the tip with a transition region between. A summary of the rotor blade metal angles for 11 streamlines passing through 5, 10, 15, 30, 50, 60, 65, 70, 85, 90 and 95 percent span of the rotor blade trailing-edge passage height from the hub is given in Table 1.

TABLE 1
ROTOR DESIGN PARAMETERS
Stations 13 and 14

% Span	Dia. 13 (Inches)	Dia. 14 (Inches)	β^*_{13} (Deg.)	β^*_{14} (Deg.)	β^*_{13S} (Deg.)	Solidity
5(hub)	17.73	20.76	58.3	14.0	62.51	2.392
10	18.81	21.34	58.2	19.5	61.85	2.257
15	19.84	21.93	58.2	25.0	61.32	2.137
30	22.65	23.705	58.55	34.5	61.02	2.105
50	26.03	26.09	60.07	46.0	62.1	1.698
60	27.66	27.275	61.45	50.5	63.25	1.629
65(shroud)	28.425	27.91	62.21	52.0	64.0	1.605
70	29.17	28.52	63.2	53.5	64.75	1.572
85	31.3	30.26	66.15	56.7	67.6	1.575
90	32.01	30.86	67.1	60.0	68.6	1.587
95(tip)	32.63	31.45	67.6	64.0	69.11	1.613

NOTE: Symbol definitions appear in Appendix I.

The stator had multiple-circular-arc airfoil sections with sections near the tip being double-circular-arc. Stator exit flow was axial for the design stagger angle. A summary of the stator blade metal angles for 11 streamlines passing through 5, 10, 15, 30, 50, 60, 65, 70, 85, 90 and 95 percent span of the rotor-blade trailing-edge passage height from the hub is given in Table 2.

TABLE 2
STATOR DESIGN PARAMETERS (STATOR 2.5° OPEN)
Stations 15 and 16

% Span	Dia. 15 (Inches)	Dia. 16 (Inches)	β^*_{15} (Deg.)	β^*_{16} (Deg.)	β^*_{15S} (Deg.)	Solidity
5(hub	21.37	22.53	47.7	−16.2	50.8	2.16
10	21.88	22.92	46.4	−14.3	49.6	2.114
15	22.4	23.31	45.8	−13.3	49.2	2.083
30	24.0	24.58	46.2	−12.5	50.7	1.98
50	26.16	26.33	46.1	−12.5	51.5	1.852
60	27.23	27.2	45.6	−12.6	51.4	1.789
65	27.29	27.65	45.4	−12.6	51.4	1.761
70	28.33	28.09	45.3	−12.7	51.3	1.739
85	29.86	29.32	46.7	−15.2	52.5	1.667
90	30.38	29.73	49.0	−17.2	54.5	1.645
95(tip)	30.87	30.09	55.0	−19.5	61.0	1.631

NOTE: Optimum setting quoted from Reference 3 is the only one utilized herein.

2. Rig Design Changes Required for Holography

A 5" x 7" polycarbonate plastic window (with a minimum thickness of 0.5" in the center to approximately 1.0" at the edges) Figure 1, was provided in the rotor casing. This window was large enough to allow a view of the rotor intrablade region and some distance upstream. A three inch diameter plexiglass window was installed in the rotor casing upstream from the viewing window which served as a port through which the illuminating light beam could enter the flow annulus. Neither window was required to satisfy stringent optical specifications.

In the area of the viewing window, Figure 2, the vane actuating lever arms and unison ring were removed. A second set of lever arms pointing rearward were joined to a partial unison ring, downstream of the original one. These fore and aft unison rings were locked to the front and rear casings, respectively.

The inner wall of the flow annulus was painted flat white to enhance reflectivity of these surfaces, increasing the amount of light reflected back through the flow region to the holographic plate. This stationary surface, when illuminated by the laser light pulse, acted as the diffuse source for three dimensional visualization of the flow, Figure 1.

B. HOLOCAMERA DESIGN AND CONSTRUCTION

1. General Description

The function of the holocamera is to record the phase and intensity of a beam of coherent, monochromatic light that has been produced . a ruby laser and passed through the flow field and/or reflected from the objects under study. This information is stored on a photographic plate in the form of a hologram. To produce the hologram, the photographic plate is illuminated by two distinct beams of coherent light. One of these beams (the object beam) passes through the phase object (flow-field); the other beam functions as a phase reference. A beam originates from a single source and is split to provide the two separate beams. When the developed hologram is illuminated by monochromatic light, an image of the phase object is produced in its original three-dimension form.

To produce a hologram, the paths followed by the object and reference beams from the point of separation to the photographic plate must be nearly equal. The necessary beam lengths are obtained by means of mirrors. In addition to the mirrors which guide the beam along their proper paths, the lenses (all of which were negative, i.e. diverging beam type; see Figure 3 for the final configuration) expand the beams to their proper diameter before illuminating the test region and photographic plate.

The following design requirements were satisfied by the holocamera constructed and used in this program.

a. Diffuse illumination of the flow region, to produce a three-dimensional view of the flow phenomena, Ref. 4 & 5

b. A large solid angle of view of the flow region, to take full advantage of the three-dimemsional properties of this kind of holography.

c. Very short Q-switched pulses, to produce high quality holograms in the presence of vibration and rig motion.

d. A self-contained system capable of remote operation and suitably damped against vibration.

2. Optical System Layout

The layout of the holocamera box and optical components, as originally designed, is shown in Figure 4. Two changes to the original design of the holocamera were made as a result of

the bench testing phase of the program. The first change involved the elimination of the laser amplifier. An Optics Technology, Inc. (OTI) ruby laser head was planned for use as the amplifier. Although the amplifier system was able to produce more than 3dB amplification during bench tests, it was also found that the OTI laser head introduced undesirable modulation of the beam intensity cross section. The ability to obtain holograms of the bench model with only the Korad HP1 laser was demonstrated, and the OTI laser amplifier was therefore eliminated from the final holocamera system. Difficulties were also encountered during bench tests with the Bragg method of producing holograms (i.e., the back illumination of the photographic plate with the reference beam). This optical configuration would have allowed the placement of the photographic plate near the rig window, and, hence, provide the largest angle of view of the flow region. Bragg holography was expected to give an angle of view close to 25° in the circumferential direction, compared to 15° for conventional holography. However, the method did not produce an image of the bench model that was bright enough to permit a clear view of the flow passage. The conventional method of holography, Fresnel, was therefore used after this method was found to produce brighter images than those obtained from Bragg holograms. Figure 3 shows the final layout of the holocamera as used to obtain holograms of flow in the NASA compressor rig.

3. FTIR Q-Switch

In the initial review of the requirements of this program, it was apparent that the Pockels cell used in Reference 1 as an optical shutter would not be fast enough for the present application. As a result, the Pockels cell was replaced by a Frustrated Total Internal Reflection (FTIR) Q-switch. The FTIR Q-switch (Figure 5) was developed by E. A. Erickson at the Naval Ordnance Laboratory and is a fast-acting optical shutter which opens and closes by a change in the internal reflection at the interface of two prisms upon command of an electrical impulse. An electrical impulse produced by a pulse generator actuates transducers, which in turn produce a mechanical shock wave in prisms Nos. 1 and 2 (Figure 5). The shock wave, which has a maximum time duration of 0.5 microsecond, causes the separation of the two prisms to decrease momentarily.

The two prisms are cut and oriented such that when the laser beam is incident at the Brewster angle the beam is totally internally reflected. When the separation of the two prisms is reduced, the total internal reflection at the interface is destroyed and the laser beam passes through the prisms. Conversely, opening action causes a large percentage of the incident light to appear at output A (Figure 5) from which point it is reflected back into the cavity by the 100 percent reflecting mirror, thus increasing the cavity "Q" to support lasing action. Coherent energy then exits from the cavity at outputs B and C, with the majority of the energy appearing at B. A double pulse is produced by generating two consecutive shock waves from both transducers. The amount of laser beam energy in each pulse can be varied by controlling the amplitude of the shock wave and the time between pulses. The power supply of the FTIR Q-switch contains two independent pulsing circuits which control pulse amplitude and timing. The FTIR Q-switch is designed to produce two pulses with controlled pulse separations of 1 to 500 microseconds.

4. Other System Components

The alignment laser of Figure 3 was a Resalab 5-milliwatt HeNe continuous wave laser. The light beam produced by the pulsed laser first passed through a negative lens to begin expansion of the beam before it passed through a Hershel wedge used as the beam splitter. The Hershel wedge was used for two reasons. First, it produced two reflected beams which diverged at an angle large enough so that a reference beam could be separated and therefore the two reflected beams would not interfere to produce extraneous fringes on the photographic plate. Second, the presence of the two separated reflected beams made a beam available, in addition to the reference beam, for detection by a photodetector. The photodetector signal was fed into a Tektronix 454 oscilloscope. Photographs of the oscilloscope screen provided a record of the beam energy, the number of pulses, and the time between pulses for each hologram. Power for the detector was supplied by a small battery located next to the detector. The object beam, which contained approximately 90 percent of the output energy of the pulsed laser, left the holocamera through the beam exit port after being expanded by two additional negative lenses. After the object beam illuminated the flow passage and was reflected from the stationary hub, the beam re-entered the holocamera where it combined with the reference beam and was recorded on the photographic plate. The plate was held in the exposed position by the plate transport system.

The plate transport system, Figure 6, was capable of storing five high resolution photographic plates. The plates were individually moved into the exposure position by remote control and returned to their light-tight storage positions after each double exposure. A movable shutter prevented ambient light from entering the enclosure between exposures. Other items shown in Figure 3 include a HeNe laser used for monitoring the energy and time separation of the pulses produced by the ruby laser.

The holocamera box had two hinged doors at the side of the box which permitted independent access to the laser portion of the system and to the hologram optics. A removable top over the laser compartment permitted additional accessibility to this section of the box during alignment of the pulsed laser. A black partition was installed between the laser section and the optical compartment to prevent light from the flash-lamp in the laser head from pre-exposing the photographic plates. A block diagram of the holography system used with the NASA fan rig is shown in Figure 7.

C. DESCRIPTION OF BENCH TESTS

1. FTIR Q-Switch

Bench testing of the various holocamera components began before assembly of the complete system was started. Several difficulties were experienced with the FTIR Q-switch during these early tests, including electronic malfunctions, and maintaining proper prism separation.

The electronic malfunctions proved to be correctable only by bypassing a portion of the Q-switch pulse generator circuitry and substituting two pulse generators and the delay circuitry in a Tektronix 545 oscilloscope. Only the high voltage section of the FTIR pulse generator remained useable. A wiring diagram of the FTIR Q-switch electronics used for the final tests is shown in Figure 8.

The problem of keeping the two prisms properly separated resulted from the tendency of the prisms to lock in optical contact with each other when either too much pressure was applied to the prism during adjustment procedures or when the ambient temperature varied. The problem was alleviated by putting a thin film of ink between the prism at the outer edges and by maintaining a constant temperature around the Q-switch. Once the above alterations were made, repeatable double pulses were obtained during bench testing with pulse separations as short as one microsecond.

2. Bench Model

A complete fan rotor assembly, Figure 9, approximately the same size as the rotor in the NASA rig but with a smaller hub-tip ratio was used as part of a bench model to simulate the the view that would be encountered in the actual test configuration. Although the hub of the NASA rig was slightly larger than the rotor disk, this hub was used in the bench tests to simulate the NASA rig more accurately.

Plastic windows were used to simulate the illuminating port and viewing window on the rig casing. The pulsed laser system and the hologram optics were assembled in the same configuration planned for the rig tests, and holograms of the bench model were attempted.

3. Laser Coherence Characteristics

At first the holograms of the bench model were of poor quality. The change from Bragg holography to conventional Fresnel holography improved the results, but a further improvement in the quality of the holograms was considered necessary to be confident of extracting useful shock location information. Therefore, coherence of the laser beam, known to be a critical factor in obtaining holograms, was studied.

Measurements of the Q-switched pulse shape indicated that several longitudinal modes were oscillating. Maximum coherence of the laser beam and, in turn, a hologram of maximum quality is obtained when a single longitudinal mode is present. Single mode output has also been reported to result in more stable output properties and, in particular, to yield reproducible pulse energies (References 6, 7, and 8). Laser light emitted during single mode operations can produce high quality holograms even when the path length differences between the object and reference beams are in excess of one meter. When more than one longitudinal mode is present, the coherence length of the laser light decreases, reducing the size of the test object which can be holographically studied, and decreasing the amount of path differences which can be tolerated between the reference and object beams. A coherence length of approximately 8 to 10 inches was considered necessary to obtain holograms which could provide an image with a field of view of 15° or more. Figure 10 exemplifies the difference in pulse shape between single mode and multi-mode output when detected by a fast photodetector and displayed on a Tektronix 519 oscilloscope. A smooth unmodulated appearance, like that of the right-hand pulse, shows single mode laser operation, while the spiked appearance of the left hand pulse signifies multi-mode operation.

A 2 mm transverse mode selector aperture, which had been supplied with the laser, was replaced by a 1 mm aperture to ensure supression of all transverse modes other than the TEM_{oo}. A sheet of exposed Polaroid film was placed in the path of the light beam, and the laser with the 1 mm aperture in the optical cavity was fired. The resulting spot on the film indicated that the intensity distribution of the beam was Gaussian and therefore single transverse mode operation had been achieved. The reduction of the aperture size also had a beneficial effect on suppression of longitudinal modes. Measurement of the pulse shape with the ultra-fast detector showed a very smooth, almost unmodulated, output. The improvement of laser coherence was further substantiated by the improved quality of holograms. A disadvantage to this change in the laser cavity was the decrease in output energy from 35 millijoules to 5 millijoules. A 1.5 mm aperture was then tested. The coherence properties of the beam were found to decrease only slightly while the output energy increased to 20 mJ. The 1.5 mm aperture was therefore used in all future holography.

4. Sensitization of Photographic Plates

Early in the bench testing phase of the program, the laser-amplifier system, planned for use in the holocamera to increase available light, was found to introduce undesirable characteristics into the laser beam; therefore, the amplifier was not used during succeeding tests. As a backup measure to be used in the event that sufficient energy could not be produced by the laser to adequately expose the photographic plates, several methods of sensitizing the plates were studied during bench testing. During final tests on the NASA rig, the laser was producing enough energy to properly expose the plates; therefore, the sensitizing methods, which included presoaking the plates in various aqueous solutions (Refs. 9 and 10) and/or pre-exposing the plates, were not used.

Holograms of the bench model taken with the 1.5 mm aperture in the laser cavity and using photographic plates presensitized by soaking in water were found to be of good quality and brightness. Figure 11 shows several photographs of the bench model taken from a hologram obtained using this procedure. The Korad ruby laser, HeNe alignment laser, and all optical components were installed in the holocamera box. Once the optics had been aligned and secured, holograms of the bench model were again taken. The resulting holograms were good, indicating that the holography system was ready to be installed in the test stand.

D. HOLOGRAPHIC TEST PROCEDURE WITH COMPRESSOR

1. Shakedown Tests

The holocamera laser and optics were aligned in the compressor test stand. Initially, the laser and optics had to be aligned daily because the Q-switch prisms separation could not be properly maintained. However, once the box temperature was properly stabilized, daily realignment was not required. The performance of the holocamera during the shakedown tests with the compressor in operation, and modifications found necessary are summarized as follows:

a) The output energy of the laser was measured at 15 to 20 millijoules, with an input of 4.1 to 4.4 kV, when the laser was operated in the Q-switched mode. This energy was sufficient to expose Agfa 10E75 plates and produce good quality holograms.

b) The Q-switch produced reproducible double pulses, with 10 microsecond separations, when the temperature of the Q-switch could be stabilized to within 2 to 3 Fahrenheit degrees. Temperature stabilization was maintained by installing three strip heaters inside the camera box which produced a total of 1400 watts of heat. A thermocouple located on the Korad optical rail was monitored in the control room where the heater control (on-off switch) was also located. The camera box temperature could be maintained at approximately 70°F with stand temperature at least as low as 20°F.

c) The quality and the viewing angle of the holograms produced during the initial trial runs were improved substantially by repositioning some of the optics to reduce the difference in path lengths between the reference beam and object beam by three to four inches, and by moving the position of the plate holder towards the downstream side of the viewing window approximately one inch. Approximately one hologram in five was of desirable quality.

d) The polycarbonate viewing window was found to be damaged after several hours of rig running. A photograph of the damaged window is shown in Figure 12. The window was repolished and reinstalled in the rig; however, during subsequent test runs, the window was damaged to an even greater extent (Figure 13). Two replacement polycarbonate plastic windows were machined, one of which was installed in the rig.

e) After firing the laser 600 to 800 times (including optical system checkouts without rig in operation), the threshold voltage (minimum voltage needed to obtain coherent light from the laser) began to increase significantly and the output energy of the laser became very erratic. The ruby laser flashlamp was, therefore, replaced. Once the laser head was reassembled and the laser realigned, the threshold voltage was found to be normal again, and the output energy much more consistent.

A subsequent test run of the holography system and fan rig produced several good holograms showing three dimensional shock distributions around the fan blades at four flow conditions, two of the flow conditions were at 100% of design speed and two were at 70% of design speed.

2. Final Tests

When the final test part of the program was initiated, one hologram was taken from the first series of five and developed to determine its exposure and quality. The developed hologram was found to be of very good quality, and the test was continued. In all, five holograms were taken at each of five flow conditions, three flows at 100% design speed and two flows

at 70% design speeds. Holograms were also taken at 50% design speed and, finally, with the rig shut down. Unfortunately, when the remaining holograms were developed, none were of the quality of the first hologram developed during the test. Despite an extensive effort to bring out the exposure of the underexposed plates by using high contrast developers, extending the developing time, and slightly fogging the plates, the quality of the original hologram could not be duplicated. Since several excellent holograms had been obtained at the desired speeds and flow conditions during the shakedown tests, it was decided to use these and not repeat the final test.

The underexposure of the holograms may have been the result of the following circumstances. The hologram developed during the test was an unfortunate choice. It was chosen because the detector had shown that the plate had been exposed to three pulses; therefore, developing the plate at the test stand would not jeopardize a double-exposed plate. However, it appears likely that a fourth pulse occurred after the 100 microsecond time interval shown on the oscilloscope, which further exposed the plate. Because of similar detector voltage displayed by the oscilloscope, subsequent holograms were thought to have been exposed to an energy equivalent to that of the developed hologram, but apparently they were not.

Following the test, the holography equipment was removed from the stand, and an analysis of the holograms begun. In addition, the test compressor was moved to the optics laboratory to permit the actual rig interior to be used to provide the most accurate interpretation for the various shock front locations.

OPTICAL ANALYSIS OF HOLOGRAMS

A. DESCRIPTION OF SUCCESSFUL HOLOGRAMS

The holocamera produced several excellent double-pulse holograms of the flow within the NASA fan rig. When the holograms are illuminated with a continuous HeNe laser beam, a three-dimensional image of the interior of the flow passage, beginning within the fan blade row and extending several inches upstream from the blades is created. A photograph taken with a conventional camera and conventional lighting of the fan rig without the window is shown in Figure 14. The rotor part-span shroud is partly visible about 4 inches inboard from the tip. The region illuminated by the ruby laser, and therefore seen in the resulting holograms, is indicated by the dotted lines enclosing a circular region on the hub. The grid lines on the hub, which were painted on as a simple reference system for use when viewing the holograms, are spaced approximately one inch apart. The effects of the window, due to the curvature of the window, the grid lines on the window, and window damage resulting from heating during fan operation, can be seen by comparing the views in Figure 14 and Figure 15. In this three-dimensional image space, within and in front of the fan blade row, dark lines, or interference fringes, can be seen in the holograms, Figures 16 through 20, generally running parallel to each other and extending upstream from the blades. The interference fringes vary in appearance from fringes which seem to belong to a group or system, Figures 16 and 17 (taken at 70% design speed) to individual fringes which seem to stand apart from others, Figures 18, 19 and 20 (taken at 100% design speed).

These differences in appearance can be attributed to variations in gas density changes occurring between the two exposures of the holograms. The Q-switch was set for a 10 microsecond pulse separation for all holograms shown. However, pressure gradients and gas flow velocities were greater at the 100% speed line and, therefore, the gas density change which occurred between exposures was greatest for holograms taken at this flow condition. Large density changes resulted in the closely spaced interferences fringes and, in the case of the holograms obtained at the 100% speed line, most of the fringes were too closely spaced to be resolved. At the 70% speed line, the pulse separation and hence the density variation between exposures was sufficiently small to produce an easily resolved finite fringe system in the space corresponding to that occupied by shock waves moving upstream from the fan blades. The appearance of these fringe systems is very much like that of conventional interferograms (Ref. 11) except that the fringe system is three-dimensional.

The flow feature most evident in both holograms obtained at the 70% speed lines (Figures 16 and 17) is a shock which lies almost midway between the leading edges of each pair of adjacent blades. The fringes associated with this shock appear to be located on a plane which starts at the window and extends down 2 or 3 inches into the flow. The exact distance is difficult to determine without a more detailed study of the hologram. Fringes can be also seen in the photographs of the reconstructed images shown in Figure 17 which are associated with the leading edge bow wave and an apparent upstream wave effect of the precompression ramp of one of the blades. This set of fringes also appears to be located on a surface extending down from the window into the flow.

During the 10 microseconds between pulses, the blades and the flow field moved a noticeable distance. For the 70% and the 100% speed line holograms this distance was approximately 1/4 inch and 1/3 inch at the blade tips respectively. A careful examination of the holograms, or of photographs of the holograms, reveal definite signs of this motion, such as the double image of the blades at the leading edge, e.g., Figure 20.

The pulse separation was too great in the holograms taken at the 100% speed line, Figures 18, 19 and 20, for the complete fringe system associated with each shock wave to be observed. Instead, single or sometimes double fringes can be seen because local density gradients were small enough to result in a visible fringe spacing. These conditions generally exist only over a relatively small region of each shock; nevertheless, the regions are large enough to be easily observed with the unaided eye. As in the holograms shown in Figures 16 and 17, fringes can be seen at the window while others are up to 7 inches in from the window. The passage shocks, which appear attached to the leading edge of the fan blade and continue downstream toward the suction surface of the adjacent blade, can only be seen near the window (Figures 18A and 20). Unlike the fringes associated with the bow waves, those associated with the passage shock are irregular, rather than running along approximately straight lines.

B. ANALYTICAL METHODS OF FRINGE LOCALIZATION

The analysis of diffusely illuminated holographic interferograms, such as those produced in this program, is accomplished by photographing the reconstructed scene from various directions within the field of view. Each photograph resembles an ordinary interferogram, and information about the flow field is determined from these photographs.

In general, it has been found that if a complete 180° field of view through the flow region can be obtained the three-dimensional distribution of density change between the first and second holographic exposure can be determined (Reference 12).

In the present program, the angular field of view was restricted by the rig geometry to less than 15° and, consequently, determination of the density change distributions was not possible. Nevertheless, even within this relatively narrow field, the fringe systems observed in the holograms exhibit very pronounced localization and perspective effects. It was, therefore, possible to determine the general features of the fringe systems, such as locations where abrupt changes in fringe spatial frequency occurred.

A more complete description of the basic theory of fringe formation in holographic interferograms is given in Appendix III. The conclusions of this analysis can be summarized as follows:

1. The optical phase or fringe number observed at any point in the photograph of a holographic interferogram depends primarily on the difference in optical path (for two hologram exposures) along the central ray through the observing aperture which terminates at that point.

2. The spatial fringe frequency in the neighborhood of a given point depends on the difference in the density gradient (for two hologram exposures) transverse to the central ray terminating at that point.

3. For density changes which are localized in space and produce significant deflections of ray paths, the fringes observed tend to be localized at the same region as the density change. For more generalized density changes, fringes can be located anywhere and their location bears no simple relationship to the location of the density changes which produced them.

4. Regions in which changes in fringe frequency occur can be located independently of the fringes themselves. These regions are very important in determining shock locations because the fringes are frequently not localized at the shock positions, while the lines of demarcation between regions of different fringe frequency are located at the shocks.

5. The visibility of the recorded fringes is best when the camera is focused on the region of fringe localization. Visibility decreases as the camera aperture increases.

Based on these general principles, several techniques for determining the shock locations were tried. The method finally adopted for reducing hologram information to graphical plots of the shock profiles involved taking a series of photographs of each hologram from at least five viewing angles. Each viewing angle differed by approximately four degrees. For each of these viewing angles, several photographs were taken with varying focus and f-number so that all features of the flow field could be seen in the series of photographs.

A triangulation method was then used to determine the position of points on a feature of interest, such as a shock wave, by measuring the position of the point with respect to the

window in two photographs taken from different angles. The triangulation method was based on the principle that three equations could be easily derived corresponding to three planes upon which a single point of interest lies. Solving these equations to determine the point of intersection of the three planes yields the coordinate values of the point of interest.

The procedure used to determine the triangulation equations from the photographs of the holograms can be made clearer by studying Figures 21 and 22. A convenient coordinate system was chosen in which the window grid is considered to lie in the Y = 0 plane. The positive X-direction is along a grid line parallel to the blade direction of rotation; the positive Z-direction is along a grid line in the axial downstream direction. The origin of the coordinate system is located at the intersection of two specific grid lines, Figure 22.

The steps involved in the quantitative analysis of the holograms can be summarized as follows:

1. Determine the viewing angles, θ_{xy} and θ_{zy}, and the distance C, from which the photographs of the hologram to be analyzed were taken, Figure 23.

2. In two photographs, locate a common point on a fringe system whose position is to be determined, and measure the apparent coordinate position, (X_o, Z_o) of the point with respect to the window grid system in the photographs.

3. Insert a set of values for C_{yz}, C_{xy}, θ_{xy}, θ_{zy}, X_o and Z_o, into the pair of equations for each photograph:

$$y = \tan\left[\theta_{yz} + \tan^{-1}\left(\frac{Z_o}{C_{yz}}\right)\right](Z - Z_o) \qquad (1)$$

$$y = \tan\left\{\cot^{-1}\left[\left(\frac{X_o}{29}\right) + \cot\left(\theta_{xy} + \tan^{-1}\left(\frac{X_o}{C_{xy}}\right)\right)\right]\right\}(X - X_o) \qquad (2)$$

   where 29 is the focal length in inches of the plastic window,

   $C_{xy} = C\sin\theta_{yz}$ and $C_{yz} = C\sin\theta_{xy}$

   Of the four resulting plane equations, any three can be used to solve for the point of intersection of these planes, which corresponds to the location of the point of interest. The three equations to be used are determined by selecting those equations representing the greatest difference in viewing angle. These equations are derived in Appendix IV.

4. Repeat the above procedure for several points around the fringe system to determine the orientation and position of the corresponding shock wave. An example of the above procedure is given in Appendix V.

The accuracy of the method described above is discussed in Appendix V. The results of the error analysis were that the uncertainty in the values of X, Y, and Z were approximately 0.4 inch. However, the majority of the uncertainty in the values of X and Z was due to motion of the rotor and flow field between exposures.

AERODYNAMIC INTERPRETATION FROM ANALYSIS OF HOLOGRAMS

A. INTRODUCTION

In the following sections, the aerodynamic interpretation of the information obtained from the successful holograms is presented. The data obtained in the flow visualization program are compared with aerodynamic data obtained earlier (Reference 3) with the same test fan rig under Contract NAS3-13493. When the holographic data were being recorded, the test compressor was set as closely as practical to the overall conditions (inlet corrected flow and corrected rotor speed) run previously. The compressor test conditions in the present program can be compared in Figure 24 with those from the earlier program. The blade element data from Reference 3 nearest to the four simulated conditions in the recent holography program are given in Appendix II.

The holographic data presented are almost exclusively limited to information regarding the upstream shock system propagating from the rotor. Exceptions are the holograms obtained at 100% design speed where information regarding the leading edge passage shock and pre-compression region at the blade tip is noted. The limited results are a consequence of the restricted viewing angle resulting from the change from Bragg to Fresnel holography, the limited region of background illumination, the location of the part-span shroud on the blade which restricted the view in the intrablade region, and the viewing blockage created by the spanwise twist of the blade leading edge.

In the following sections, descriptions of the assumptions made to complete aerodynamic interpretation of the holographic data are given. The presentation of the data itself is made to show, for the various flow conditions of the transonic rotor, the nature of the observed leading edge bow and passage shock waves at several spanwise positions.

B. DESCRIPTION AND ASSUMPTIONS

The bow shock information was obtained by using the location of fringe points determined by the method described in Appendix IV. Since only certain fringe points in each hologram could be associated accurately with local density changes, there was no consistent demonstration of the shock patterns at the same radial locations for each hologram. For the shocks whose position and orientation were noted, at least two fringe points were determined at approximately the same spanwise location along the rotor blade. These fringe points were projected onto a plane tangent to a cylinder whose radius (measured from the compressor axis) was an average of the radii to the measured points. This projection was found to be suitable for most cases because the error in the Y-dimension (distance inward from the window plane) was such that the transfer of points to the same tangent plane was a reasonable approximation. In each tangent plane, two or more points were connected, indicating the shock angles determined by holographic analysis with respect to the known blade shape and orientation (see Reference 2).

Using Figure 25 as an example of the demonstration of the holographic data results to be given, the blade section in a tangent plane at a radius of 16.5 inches is shown for the 70%

speed, near stall flow conditions (hologram 8). The inlet flow and the direction of blade rotation are as shown in Figure 16 and 25. The line in Figure 25 emanating from near the blade suction surface, and extending into the upstream flow field, represents the localization of fringes from hologram 8 (see Figure 16) onto this plane. The crosses on the reconstructed fringe line (labeled "measured precompression wave") are the points determined by the localization method described in Appendix IV. The circled cross is the projection of the origin of the (X, Y, Z) coordinate system located on the outer window grid (see Figure 22) onto the tangent plane at the radius of 16.5 inches.

The measured shock angles were projected onto planes tangent to a cylinder at the radius of interest from the compressor axis. In the mid-span region, these planes correspond closely to blade section planes, which are tangent to nearly axial meridional streamlines. The orientation in the tangent plane of each shock with respect to the blade can then be determined and compared with angles calculated from blade element data. In the tip region, however, the angle ϵ of the meridional streamline with respect to the compressor axis approached values at the rotor leading edge approximately -20°; at the hub approximately 36.3°. Thus a correction between an angle measured in a tangent plane at a given radius and that determined in a tangent plane at the conical angle ϵ was made. This was done using Eq. (3), which can be derived by noting that the projection μ of the angle $\bar{\mu}$ between two lines in a conical plane at an angle ϵ with the respect to a radial plane (see Figure 26) is given by:

$$h_1 \sin \frac{\bar{\mu}}{2} = \frac{h_3}{2} = h_2 \sin \frac{\mu}{2}; \quad \frac{h_2}{h_1} = \cos \epsilon$$

so that

$$\sin \frac{\mu}{2} = \frac{1}{\cos \epsilon} \sin \frac{\bar{\mu}}{2} \qquad (3)$$

This formula was used to compare the bow wave angle $\mu_{meas.}$ deduced from the holograms with the projection μ of the Mach angle $\bar{\mu} = \arcsin(1/M'_{13})$. (The angle $\mu_{meas.}$ is the Mach angle measured with respect to the relative flow direction in each tangent plane). The value of the relative Mach number M'_{13} was obtained from the blade element data on a neighboring streamline at an angle ϵ to the compressor axis. Since the computed Mach wave is based on the axisymmetric value of leading edge Mach number, it is proper to consider this wave as the leading edge asymptotic Mach wave, as in Figure 27. The comparison between the angle μ and $\bar{\mu}$ is shown in Table 3 for the four flow conditions and the eight radial planes onto which all the holographic data were projected. The indicated streamline angles ϵ did not vary significantly enough among the four flow conditions to warrant using other than design values. In addition, the relative Mach numbers used to calculate the angle $\bar{\mu}$ in Table 4 are those calculated by the streamline analysis at approximately the rotor leading edge (Appendix II). The points determined by the analyses of the holograms were located four inches or less axially upstream of the rotor leading edge. For these points, the relative Mach number was subject to change from variations in the stream tube thickness and radial location. The Mach number and relative air angle variations as functions of upstream axial position are shown in Table 4 for several streamlines for the 70% and 100% design speed near stall conditions, as calculated by the streamline analysis. These are given as typical variations

for other speeds and pressure ratios. Variations can be appreciable, especially with regard to the air angle β'. Changes in relative Mach numbers (and Mach angles) from those calculated in the rotor leading edge plane are of lesser magnitude. Therefore, no entirely direct comparison between shock angles deduced from the holograms and Mach angles calculated from rotor leading edge Mach numbers was possible.

TABLE 3

COMPARISON OF MACH ANGLES CALCULATED FROM BLADE ELEMENT DATA AND CORRECTED MACH NUMBERS ACCORDING TO EQUATION 3

		100% Speed Conditions				70% Speed Conditions			
		Near Stall		Maximum Flow		Near Stall		Intermediate Flow	
Dia. (in.)	ϵ	$\bar{\mu}$	μ	$\bar{\mu}$	μ	$\bar{\mu}$	μ	$\bar{\mu}$	μ
21.2	19.5	56.4°	60.0°	55.74	59.4				
22.6	14.0	51.38	53.0	50.53	52.2	Subsonic Inlet Relative Mach Number			
24.0	8.6	47.2	47.8	46.55	47.2				
26.14	0.5	42.68	42.7	42.10	42.1				
27.86	− 6.5	40.03	40.2	39.63	39.8	79.5°	80.0°	76.7°	77 2°
28.98	−10.7	38.65	39.4	38.30	39.0	71.7	73.0	70.3	71.6
30.68	−16.4	36.91	38.6	36.53	38.1	64.83	68.0	63.6	66.8
32.12	−21.3	35.43	37.8	35.08	37.4	60.41	64.8	59.6	64.0

KEY:
$\bar{\mu} = \sin^{-1}(1/M'_{13})$
μ derived from Eq. 3

TABLE 4

TYPICAL VARIATIONS OF M' β' AS A FUNCTION OF AXIAL DISTANCE UPSTREAM OF ROTOR

100% Speed Condition Near Stall

Axial Location	Diameter of Streamline at Blade Leading Edge (in.)											
	19.92		22.73		26.04		28.3		31.2		33.02	
(in.)	M'	β'	M'	β'	M'	β'	M'	β'	M'	β'	M'	β'
L. E.	1.128	62.1	1.294	62.36	1.468	63.95	1.574	65.7	1.687	69.9	1.765	70.41
−1.0	1.05	64.9	1.226	65.62	1.41	67.67	1.526	69.77	1.666	72.8	1 753	74.6
−2.25	.998	67.1	1.184	68.2	1.386	70.5	1.515	72.64	1.676	75.5	1.774	77.3
−4.0	.969	67.0	1.156	69.56	1.368	72.7	1.508	74.9	1.685	77.7	1.794	79.4

70% Speed Condition – Near Stall

Axial Location	Diameter of Streamline at Blade Leading Edge (in.)											
	19.97		22.75		26.03		28.29		31.2		33.02	
(in.)	M'	β'	M'	β'	M'	β'	M'	β'	M'	β'	M'	β'
L. E.							1.03	70.7	1.12	73.0	1.18	74.23
−1.0			SUBSONIC				1.027	73.25	1.13	75.71	1.20	77.1
−2.25			RELATIVE				1.03	75.1	1.15	77.4	1.22	78.8
−4.0			FLOW				1.035	76.8	1.16	79.2	1.24	80.67

Finally, the comparison of the shock angles (approximated in the holographic analysis as straight lines between measured fringe points) with Mach angles assumes that each bow wave under scrutiny has attenuated to a Mach wave at the Mach angle of the upstream asymptotic flow field. As the following presentation of data demonstrates, many of the measured fringe points were close enough to the blade leading edge that this condition was not met.

C. AERODYNAMIC ANALYSIS OF HOLOGRAMS TAKEN AT 100% SPEED

1. Shock Patterns at Maximum and Near Stall Flows

At the 100% design speed condition, holographic data were successfully obtained at the maximum flow condition (hologram 1, Figure 18 and hologram 3, Figure 19) and at the near-stall condition (hologram 21, Figure 20). For the near-stall condition, hologram 21 provided information regarding both bow and passage shocks (Figure 27 a, b, c, d). Also included are the leading edge suction surface incidence and Mach angles from blade element data, corrected according to equation 3. It should be noted that this flow condition was on an overall performance basis, closest to design performance goals. The passage shock at the blade tip (Figure 27a) was observed at an angle of 73.0° to the blade suction surface compared to the design value of 74.4°. In addition, from Figure 20a (a photograph taken of hologram 21 focused at the blade tip), a region of density change is distinguished to the right of the observed leading edge tip by a difference in intensity from neighboring regions, and not by a regular fringe system. This region appears to cover the area that the precompression ramp would be expected to influence. The difference between the extent of this observed region and the design intent is that Figure 20 shows some effect forward of the blade leading edge, with this difference possibly caused by blade shape irregularities or by various endwall effects (e.g., tip clearance, endwall boundary layer and secondary flows, radial flows).

Another interesting feature can be seen in Figure 27a, b taken from hologram 21. At the tip, $r = 16.06$ inches, the measured bow shock is at a larger angle with respect to the relative flow direction than at the smaller radial position, $r = 15.34$ inches. As smaller radial positions are approached, the bow shock again swings out to larger angles with respect to relative flow direction. This is, of course, a consequence of decreasing Mach number, and resulting higher Mach angles for decreasing radial positions along the blade span. The large Mach angle at the tip section, therefore, indicates a local decrease in Mach number. This tip effect probably is caused by the endwall boundary layer where the relative Mach number is less than the value outside the boundary layer due to the decreased axial velocity. The angle measured from the holographic data appears to give some average effect of the reduced Mach number in the endwall region. The values of relative Mach number and incidence given by the blade element data are outside the endwall region and, therefore, do not reflect endwall reduced Mach numbers and increased leading edge incidences. The comparisons of the angles of the bow waves deduced from the holograms and the leading edge asymptotic Mach waves thus appear generally poorer at the tip than at lower radial planes for the results shown in Figure 27. This conclusion is generally true for each of the holograms.

For the maximum flow condition at 100% design speed, holograms 1 and 3 (Figures 18 and 19) provide a variety of information regarding the upstream bow waves and the tip passage shock, as shown for several radial locations in Figure 28. The design value of the angle between

the passage shock and blade suction surface was 74.4° with an inlet relative Mach number of 1.77. For hologram 1, the measured angle was 60° The shock appears to be attached and swept back, definitely indicating a started flow condition. The fact that the shock is more oblique than design intent is consistent with this flow point being at a lower than design value of static pressure ratio.

In observing the results for all holograms taken at the 100% design speed condition, Figures 27 and 28, it is apparent that the measured bow waves are at a larger angle with respect to the tangential direction than the corrected calculated leading edge Mach waves. This result has been largely explained by Table 4, where the changes in calculated relative Mach number M' and air angle β' at and upstream of the rotor leading edge are given. The listings in Table 4 infer differences of the angle between the local Mach wave and the tangential direction, $(\mu + \beta' - 90°)$, as large as 10° between rotor leading edge and a station four inches upstream. This order of change does not explain the still larger differences (e.g. 20° in Fig. 28a for a tip radial position) in measured and calculated angles in Figures 27 and 28. At radial positions away from the tip, however, the correction in angle inferred by Table 4 does bring the measured and calculated angles within closer agreement.

Some differences between holographically measured angles and calculated angles may exist because the holographic results do not compare the same blade passage. As the compressor was set at its operating points, holograms were taken at random times; no attempt was made to visualize the same blade passage each time. Therefore, blade-to-blade differences may introduce some errors when comparing holographically measured results with inlet average calculated values.

2. Comparison of Holographic Data with Blade Element Data and Rotor Tip Static Pressure Contours

The rotor tip static pressure contours obtained from Reference 3 are shown in Figure 29a for 100% speed, maximum flow condition and in Figure 29b for 100% speed, near stall condition. A strong leading edge passage shock at the blade tip can be observed from Figure 29a, followed by an expansion region which accelerates the flow and gives rise to a trailing edge shock. The holographic data provide information about the leading edge passage shock only, giving no indication of its reflection or other downstream phenomena due to the limited field of view. The angle of the oblique passage shock from the suction surface leading edge has a design value of 74.4°, compared with an angle of 60° from hologram 1 (Figure 28a). The average shock angle that can be drawn using static pressure contours is approximately 64° (Figure 29a), which is in close agreement with the result of hologram 1. This indicates that at maximum flow condition the passage shock is swept back further than at the design (near stall) condition. Again, this is the expected result at lower than design values of back pressure.

From Figure 29b, the static pressure contour for the near stall condition (also the closest to design performance goals on an overall rotor performance basis) shows a suction surface flow expansion before the precompression ramp, followed by a compression in the vicinity of the ramp. There is, however, no evidence here of a focus of compression waves near the tip of the adjacent blade. As noted earlier, the hologram taken at this condition, (hologram 21, Figure 20), indicated some density changes extending from the vicinity of the precompression ramp to a region near the leading edge of the following blade. The leading edge passage shock

from Figure 29b seems to be directed toward the maximum suction surface camber point at an angle almost at the design intent of 74.4°. The angle for this shock, measured from the hologram, is approximately 73°, which shows excellent agreement from all sources of comparison. The activity downstream of the leading edge shocks, seen in Figure 29b, was not observed in the holograms. It was in this region, for design speed conditions, that much of the major shock structure was altered when throttle conditions were changed.

In summary, the results from the holograms taken at 100% design speed condition show the upstream bow waves at larger angles with respect to the tangential direction than would be indicated by the Mach wave angles calculated from rotor leading edge corrected Mach numbers. The angle differences are as large as 22°, with maximum discrepancy near the blade tip. This has been partly explained by the variation in upstream relative Mach and air angle shown in Table 4. All results indicate that the leading edge shocks, both passage and bow waves, remain attached at the tip over the entire compressor flow range. This is further confirmed from the leading edge suction surface incidence and Mach numbers as calculated in the blade element data (Figure 30). The small additional incidence at the near stall point, which results in decreased flow, is not apparent in a tip shock detachment when viewing results of the holograms. Some shock detachment is noted at lower spanwise positions for both maximum flow and near stall flow, which is expected from the effect of decreasing Mach number. This is evidenced by larger values of suction surface incidence i_s in the mid-span region, especially in the near stall case. It may be concluded, therefore, that in the tip region the blade passage flow was started over the entire flow range. The change in the angle of the leading edge passage shock between maximum flow and near stall flow shows the effect of back pressure. This behavior is also seen in the rotor tip static pressure contours. No irregular radial shock structure could be discerned from the holograms taken at 100% speed, except for the previously discussed endwall effect on the bow wave angle.

D. AERODYNAMIC ANALYSIS OF HOLOGRAMS TAKEN AT 70% DESIGN SPEED

1. Shock Patterns at Intermediate and Near Stall Flows

At the 70% design speed condition, holographic data were successfully obtained at the near stall condition (hologram 8, Figure 16) and at the intermediate condition (hologram 13, Figure 17). For the near stall condition, the only fringes that could be located apparently emanated from the blade suction surface, approximately at the mid-point of the uncovered portion of the blade suction surface. Figure 16 shows a photograph focused at the blade tip of the fringe system of hologram 8. The reconstruction of this fringe system at the tip radius 15.5 inches is given in Figure 25a, and at a radius of 14.49 inches in Figure 25b. Also included are the leading edge suction surface incidences, calculated from blade element data, (Figure 30). These reconstructed fringe lines are interpreted as manifestations of precompression waves and their coalescence off the blade suction surface at inlet Mach number levels far below design values. That is, at the 70% speed conditions, the blade was running at higher than design incidences, but at lower Mach numbers, so that compression waves off the concave precompression ramp missed the leading edge of the following blade. Since these waves tend to converge, it would be expected that a shock would result in the upstream field. The lines indicated in Figures 25a and b from the fringe system apparently represent some average location of this compression system generated by the suction surface precompression ramp. No information regarding the leading edge bow shock system for hologram 8 could be determined.

For the intermediate flow condition at 70% design speed recorded by hologram 13, Figure 17 information was obtained regarding both the bow shock system and a similar compression system created by the precompression ramp as noted for hologram 8. Hologram 13 possesses a rather classic interference pattern, permitting further analysis of the hologram itself, using two interpretive methods. The first, described in Appendix IV, was used in analyzing the previously discussed holograms. The second method was an attempt to generalize the technique by using three fringe points to define a shock surface (i.e., a plane) in space. Intersection of such a surface with any blade plane would describe the shock shape in that plane. A description of the second technique is given in Appendix VI, as applied for hologram 13.

Figure 31a, b, c, d indicate the pointwise reconstruction of the shock system at various radial positions. Also included for comparison are the leading edge suction surface incidences and Mach angles corrected to Equation 3. The reconstructed fringe lines which appear between the lines representing bow waves again would seem to result from the precompression ramp wave system at reduced Mach numbers associated with the 70% design speed, intermediate flow condition.

The plane reconstruction of the bow shocks from holographic data, described in Appendix VI, for hologram 13 is presented in Figures 32a, b, c, d for four radial positions. Where possible, the pointwise reconstruction shown in Figure 31 has been superposed for comparison. There is generally fair agreement in the results of the two techniques. Agreement, for example, between the angle of the bow wave on the left blade determined by plane reconstruction and either the wave determined by the "point" reconstruction, or the leading edge asymptotic Mach wave direction, is excellent. The discrepancy between angles for the bow waves from the plane reconstruction off the adjacent blades is attributable to errors in determining the points which define the shock plane. These errors arise if, say, two points defining the shock plane are chosen near the blade tip and a third chosen at a much smaller radius. The plane reconstruction of the shock surface then proved most satisfactory near the tip, with discrepancies occurring at the smaller spanwise radii. A more general shock surface than a plane is needed to adequately define the bow waves in hologram 13, although the plane reconstruction method apparently produces reasonable results for the left blade, since regular fringe patterns were obtained in this hologram. For more complex fringe patterns obtained for the 100% design speed conditions, the plane reconstruction method is not applicable.

2. Comparison of Holographic Data With Blade Element Data and Rotor Tip Static Pressure Contours

The rotor blade tip static pressure contours are shown in Figure 33a for the 70% speed, near stall condition, and in Figure 33b for a 70% speed, intermediate condition. Figure 33b shows a strong leading edge passage shock, slightly detached from the blade, and some indications of a trailing edge shock. These phenomena are not apparent from holograms 8 and 13 because of the limited field of view. Figure 33b indicates that in the forward portion of the blade suction surface there were relatively large upstream pressures, followed by the leading edge passage shock. These upstream pressures appear to be associated with the "mid-shock" located between bow shocks in the intermediate flow condition (hologram 13, Figures 31 and 32) and the near stall condition (hologram 8, Figure 25). The tip static pressure contours do not supply any information about the location or shape of the upstream bow waves.

In summary, the results of the holograms taken at the 70% design speed condition show an upstream effect of a precompression ramp at Mach numbers below design levels. The limited bow shock wave data from hologram 13, Figures 31 and 32 generally show the waves at a larger angle with respect to the tangential direction than the corrected leading edge Mach wave angle. This result is similar to that obtained for the 100% design speed cases and can be similarly explained.

Finally, the holographic results at this 70% speed condition do not give conclusive evidence of the location of the bow waves with respect to the rotor blade leading edge. From the results of hologram 13, Figures 31 and 32, it appears that the bow wave was attached at the blade tip, and became progressively more detached proceeding inward from the tip. The blade element results, however, for the leading edge suction surface incidence at 70% speed, Figure 30, show significantly larger than design (100% speed) incidences. Such large incidences are consistent with more significant shock detachment at the lower speeds. Further holographic data are needed to reconcile the discrepancy between these results at the blade tip, although qualitative agreement is seen at smaller radial elevations.

E. OTHER AERODYNAMIC DISCUSSION

In all sets of data from the various holograms, no unusual radial variations of the bow wave structure were observed, with the exception of the end wall effect seen for the 100% speed at near stall (Figure 27). At 70% speed, the bow shock was detached over most of the span, and indicated relatively small spanwise variations. The relative "flatness" of this shock surface suggested a plane reconstruction of the shock surface described in Appendix VI. At 100% speed, the bow shocks were attached over the outer part of the span, with increasing detachment as lower radial positions were reached. No discontinuous behavior in these radial shock patterns was observed.

In the discussion of the 100% speed data in Section C herein, the statement is made that the flow in the outer region of the rotor appears to be started over the range from maximum flow to near-stall flow. In this context, the term "started" is intended to mean that upstream conditions into the blade passage are independent of the throttle, or back pressure, condition across the blade row. For a fixed inlet relative Mach number, these upstream conditions were a function only of the blade geometry. In the present case, at 100% speed, the leading edge passage shock remains oblique over the entire flow range with an essentially fixed relative Mach number and air angle, so that the flow is presumed to remain started. Small changes in relative air angle can result for a started passage due to finite leading edge bluntness effects and to effective changes in suction surface geometry due to boundary layer growth. This is verified by the blade element data shown in Figure 30, where maximum calculated differences in incidences (or relative air angles β'_{13}) of about one degree are shown for flow variations ranging from maximum flow to the near surge point.

The previously noted variation of oblique shock angle (i.e., strength) with back pressure observed in the holograms does not contradict the fact that the flow remains started, since the inlet conditions are affected only to a small measure. In the Design Report of this fan stage (Reference 2), it was stated that the flow would only start if the normal shock at the channel entrance during the starting process were based on a Mach number lower than the leading

edge asymptotic Mach number. This argument was based on the Kantrowitz-Donaldson contraction ratio for starting, (References 13 and 14). If the rotor had not started at 100% speed, the maximum flow rate would have been lower than design, and the flow would have dropped significantly as the throttle was closed from the maximum flow condition. This was not the case; in fact, the stage had a 2.3% overflow from design value at the maximum flow conditions, (Reference 3). Evidence from the holograms indicates that in the outer region of the rotor the flow was started for all conditions at 100% speed and unstarted at 70% speed (except near the blade tip). These results are consistent with the Mach number change resulting from the speed change and the corresponding required area for starting.

In Reference 15, a shadowgraph technique used to analyze the shock patterns and performance of two supersonic compressor rotors is described. The compressor, with a hub-to-tip ratio of 0.75, was tested with a set of sharp leading edge, and a set of rounded leading edge, blades. The shadowgraphs generally showed the tip bow and passage shock patterns only, since this technique does not permit three-dimensional resolution possible with double-pulse holography. The conclusions were that, as the flow in the rotor starts, no discontinuity in compressor performance occurs, and that it is possible for the compressor to have a decrease in weight flow while the flow remains started. The previously described analysis of the holographic data recorded at 100% speed is in agreement with this latter conclusion. Unfortunately, the present results do not cover as broad a flow and throttle setting range as reported in Reference 15. A complete variation such as that presented in Reference 15 is needed to fully understand the starting process, especially since the holographic technique stores information for later and prolonged observation of three-dimensional effects.

SUMMARY OF RESULTS

The technique of double-pulse, double-exposure interferometric holography was successfully applied to visualize the flow field ahead of and within a limited region of transonic compressor rotor with a tip speed of 1800 ft/sec. The major results were:

1. Successful holograms of the flow within and ahead of the transonic rotor were obtained. The three-dimensional nature of the bow shock structure was determined, using techniques devised for locating fringe positions in the holograms. The orientation of the leading edge passage shock near the blade tip was also found.

2. The pulse separation used for the holograms was limited to 10 microseconds because of temperature and reliability problems with the FTIR Q-switch. Pulse separations of one microsecond or less would increase the visibility of the flow in regions where large density gradients have reduced fringe spacing to unresolvable values. Also, by varying the pulse separation over a wide range of values, shock waves of almost any strength could be sequentially viewed at all radial locations.

3. Flow features generally could be seen only in the upstream portion of the blade passage. An increase in the size of the intrablade region that could be viewed would be brought about by viewing the flow field against a stationary portion of the rig other than the hub, such as possible struts or the casing upstream of the rotor.

4. Crazing of the viewing window during tests reduced the visibility of the flow field. The material used for the manufacture of the viewing window, polycarbonate plastic, should be replaced by a material with greater high temperature tolerance, such as a fused quartz.

5. Fewer than 10% of the holograms taken resulted in clear pictures of the flow field. A pulsed laser with greater coherence stability than was available for these tests would increase the number of good holograms obtained during each test run.

6. Blades were not always in the most convenient positions for viewing the surrounding flow field. It would be advantageous to include the capability of timing the laser pulses with a blade position indicator (for the first pulse) to ensure that blades are in the proper viewing position when the holograms are exposed. This procedure would also permit the viewing of any blade which might be of particular interest.

7. At the 100% speed near stall flow, the closest to the design goal on an overall performance basis, the leading edge passage shock angle determined from the holograms agreed closely with both the design value and the observed angle from rotor tip static pressure contours. At the maximum flow condition, the observed passage shock was more oblique, consistent with the lower than design static pressure at the rotor exit. This result is also in qualitative agreement with rotor tip static pressure contours. Also at 100% speed, the analysis of the holograms indicated that, in the outer portion of the blade span, the flow remains started with attached shocks from the maximum flow condition to near stall flow. This result is in general agreement with calculated leading edge blade element values of Mach numbers and incidences. At lower positions along the blade span, progressive shock detachment was noted.

8. The measured bow wave angles from the holographic data for both 70% and 100% of design speed were generally too large compared with those calculated from leading edge blade element data. In some cases, however, agreement was quite satisfactory. In the tip endwall region, larger bow shock angles were measured than those at lower depths, presumably due to the reduced velocity in the casing boundary layer.

9. The effect of precompression ramp of the blading was seen at 70% speed as a coalescence of waves, and at 100% speed as a broad region, quite close to the design intent except for some effect ahead of the blade leading edge.

10. At 70% speed, the holograms appeared to indicate attached bow waves at the rotor tip, which was not in agreement with relatively large blade element values of leading edge incidences. No explanation for this difference can be made.

APPENDIX I

SYMBOLS AND PERFORMANCE PARAMETER DEFINITIONS

APPENDIX I-a

SYMBOLS

a	–	distance between two points on the hub
A	–	area, ft^2
b	–	distance on the viewing window between two points associated with two lines of sight
B	–	camera position
C	–	distance from camera lens to holographic image of the viewing window
d	–	distance between window and rig hub
D	–	diffusion factc. (u.ıed D, Table 5)
f	–	focal length of viewing window; f-stop of lens
g_c	–	conversion factor, 32.17 lb_m ft/lb sec^2
ID	–	Inside Diameter, inches
i_m	–	incidence angle, angle between inlet air direction and line tangent to blade mean camber line at leading edge, degrees (labelled INCM, Table 6)
i(r)	–	field intensity in the image plane (Appendix III only)
i_s	–	incidence angle, angle between inlet air direction and line tangent to blade suction surface at leading edge, degrees (labelled INCS, Table 6)
J_1	–	first order Bessel function
k	–	light propagation vector
l	–	pathlength of central ray through phase object (Appendix III)
m	–	slope of a line
M	–	Mach number
MCA	–	Multiple-Circular-Arc
n	–	index of refraction
N (k,r)	–	plane wave spectrum (Appendix III only)

N	–	rotor speed, rpm ($N/\sqrt{\theta}$)
OD	–	outside diameter inches
O	–	point on lens (Appendix III only)
P	–	total pressure, psfa
P	–	point in the image of the flow region (Appendix III only)
P'	–	conjugate point of P
p	–	static pressure, psfa
r	–	radius from compressor centerline, inches
r	–	position vector (Appendix III only)
$R_{1,2}$	–	radii of curvature of viewing window (Appendix IV only)
R	–	gas constant for air, ft lb/lb_m °R
S	–	point on diffuse source of light (Appendix III only)
$s_{1,2}$	–	distance of object or image from imaging lens (window) (Appendix IV only)
SL	–	Streamline Number
T	–	total temperature, °R
t	–	static temperature, °R
t	–	displacement vector (Appendix III only)
U(r)	–	field amplitude (Appendix III only)
U	–	rotor speed, ft/sec
V	–	air velocity, ft/sec
V	–	fringe visibility (Appendix III only)
Vm	–	meridional velocity $(Vr^2 + Vz^2)^{1/2}$, ft/sec
W	–	weight flow, lb_m/sec

X,Y,Z	–	coordinate system used in optical analysis of holograms
α	–	angle between deflected central ray and y - z plane (refer to Figure 38)
β	–	absolute air angle, $\cot^{-1}$ (Vm/V_θ), degrees
β	–	angle between deflected central ray and x - z plane (refer to Figure 37) (Appendix III only)
β'	–	relative air angle, $\cot^{-1}$ (Vm/V_θ'), degrees
γ	–	ratio of specific heats for air, 1.4
$\Delta\beta$	–	air turning angle, degrees
δ	–	ratio of inlet total pressure to standard pressure of 2116.22 lbs/ft^2
$\delta°$	–	deviation angle, angle between exit air direction and tangent to blade mean camber line at trailing edge, degrees
ϵ	–	angle between tangent to streamline projected on meridional plane and axial direction, degrees
κ	–	small orthogonal addition to the light propagation vector
ζ	–	axial coordinate defined in Appendix VI
η	–	efficiency, % (listed η_{ad}, Table 5)
θ	–	viewing angle measured between plane of window and line of sight (refer to Figure 23, Appendix IV)
θ'	–	angle between the line of sight and the X-axis
θ	–	ratio of inlet total temperature to standard temperature of 518.6°R
λ	–	wavelength of light
$\bar{\mu}$	–	Mach angle, $\sin^{-1}$ $(1/M')$
μ	–	corrected Mach angle, according to Eq. (3)
μ_{MEAS}	–	upstream shock angle as measured from hologram
ρ	–	mass density, lb_m/ft^3
$\sigma_x, \sigma_y, \sigma_z$	-	standard deviations (Appendix V only)
σ	–	solidity, ratio of chord to spacing

σ – shock surface (Appendix III only)

ϕ (k,r) – phase of wave vector

Φ – angle between line of sight through feature of interest and line of sight through origin of (x,y,z) system (Refer to Figure 41)

ψ – angle between y-axis and line of sight through image or object (Refer to Figure 41)

$\bar{\omega}$ – total pressure loss coefficient (labelled loss coefficient, Table 5)

ω – angular velocity of rotor, radians/sec

ω – angular aperture of viewing system (Appendix III only)

Ω – aperture function

Superscripts:

$'$ – relative to moving blades

* – designates blade metal angle

$^{\circ}$ – degrees of arc

Subscripts:

ad – adiabatic

p – polytropic or profile

r – radial direction

meas. – measured quantity from holographic data

m – meridional direction (in z-r plane)

x,y,z – coordinate directions used in optical analysis of holograms

s – suction surface

θ – tangential direction

0 – plenum chamber stagnation value

11 – instrumentation plane upstream of rotor

13 – station at rotor leading edge

14 – station at rotor trailing edge

15 – station at stator leading edge

16 – station at stator trailing edge

17 – instrument plane downstream of stator

APPENDIX 1-b

PERFORMANCE PARAMETERS

a) Relative total temperature

$$T'_{13} = t_{13} \left[1 + \frac{\gamma - 1}{2} (M'_{13})^2\right] \qquad \text{(rotor in)}$$

$$T'_{14} = T'_{13} + \left[\frac{(\omega r_{14})^2 - (\omega r_{13})^2}{\frac{2\gamma}{\gamma - 1} R g_c}\right] \qquad \text{(rotor out)}$$

b) incidence angle based on mean camber line

$$i_m = \beta'_{13} - \beta'^{*}_{13} \qquad \text{(rotor)}$$

$$i_m = \beta_{15} - \beta^{*}_{15} \qquad \text{(stator)}$$

c) Deviation

$$\delta^{\circ} = \beta'_{14} - \beta'^{*}_{14} \qquad \text{(rotor)}$$

$$\delta^{\circ} = \beta_{16} - \beta^{*}_{16} \qquad \text{(stator)}$$

d) Diffusion factor

$$D = 1 - \frac{V'_{14}}{V'_{13}} + \frac{r_{14} V_{\theta 14} - r_{13} V_{\theta 13}}{(r_{14} + r_{13}) \sigma V'_{13}} \qquad \text{(rotor)}$$

$$D = 1 - \frac{V_{16}}{V_{15}} + \frac{r_{15} V_{\theta 15} - r_{16} V_{\theta 16}}{(r_{15} + r_{16}) \sigma V_{15}} \qquad \text{(stator)}$$

e) Loss coefficient

$$\bar{\omega} = \frac{P'_{13}\left[\dfrac{T'_{14}}{T'_{13}}\right]^{\frac{\gamma}{\gamma-1}} - P'_{14}}{P'_{13} - p_{13}} \qquad \text{(rotor)}$$

$$\bar{\omega} = \frac{P_{15} - P_{16}}{P_{15} - p_{15}} \qquad \text{(stator)}$$

f) Loss parameter

$$\frac{\bar{\omega}\cos\beta'_{14}}{2\sigma} \qquad \text{(rotor)}$$

$$\frac{\bar{\omega}\cos\beta_{16}}{2\sigma} \qquad \text{(stator)}$$

g) Polytropic efficiency

$$1)\ \eta_p = \frac{\dfrac{\gamma-1}{\gamma}\ln\left[\dfrac{P_{14}}{P_{13}}\right]}{\ln\left[\dfrac{T_{14}}{T_0}\right]} \qquad \text{(rotor)}$$

$$2)\ \eta_p = \frac{\frac{\gamma - 1}{\gamma} \ln \left[\frac{p_{16}}{p_{15}} \right]}{\ln \left[\frac{t_{16}}{t_{15}} \right]} \qquad \text{(stator)}$$

h) Adiabatic efficiency

$$\eta_{ad} = \frac{\left[\frac{P_{14}}{P_{13}} \right]^{\frac{\gamma - 1}{\gamma}} - 1}{\left[\frac{T_{16}}{T_0} \right] - 1} \qquad \text{(rotor)}$$

$$\eta_{ad} = \frac{\left[\frac{P_{16}}{P_{11}} \right]^{\frac{\gamma - 1}{\gamma}} - 1}{\left[\frac{T_{16}}{T_0} \right] - 1} \qquad \text{(stage)}$$

APPENDIX II

BLADE-ELEMENT AND OVERALL PERFORMANCE WITH UNIFORM INLET FLOW

TABLE 5

IDENTIFICATION OF BLADE-ELEMENT OVERALL PERFORMANCE TABLE HEADINGS

ROTOR

SPEED CODE ①

SL	EPSI-1 DEGREE	EPSI-2 DEGREE	V-1 FT/SEC	V-2 FT/SEC	VM-1 FT/SEC	VM-2 FT/SEC	Vθ-1 FT/SEC	Vθ-2 FT/SEC	B-1 DEGREE	B-2 DEGREE	M-1	M-2	U-1 FT/SEC	U-2 FT/SEC	M'-1	M'-2	V'-1 FT/SEC	V'-2 FT/SEC
②	ϵ_{13}	ϵ_{14}	V_{13}	V_{14}	V_{m13}	V_{m14}	$V_{\theta 13}$	$V_{\theta 14}$	β_{13}	β_{14}	M_{13}	M_{14}	U_{13}	U_{14}	M'_{13}	M'_{14}	V'_{13}	V'_{14}

SL	INCS DEGREE	INCM DEGREE	DEV DEGREE	TURN DEGREE	RHOVM-1	RHOVM-2	D-FAC	OMEGA-B TOTAL	LOSS-P TOTAL	PT2/PT1	%EFF-P TOT-ST	%EFF-A TOT-ST	B'-1 DEGREE	B'-2 DEGREE	Vθ'-1 FT/SEC	Vθ'-2 FT/SEC
②	i_{s13}	i_{m13}	δ°_{14}	$\Delta\beta$	$\rho_{13}V_{m13}$	$\rho_{14}V_{m14}$	D	$\overline{\omega}$	$\frac{\overline{\omega}\cos\beta'_{14}}{2\sigma}$	P_{14}/P_{13}	η_p	η_{ad}	β'_{13}	β'_{14}	$V'_{\theta 13}$	$V'_{\theta 14}$

TO/TC INLET	PO/PO INLET	EFF-AD INLET %	EFF-P INLET %	WC1/A1 LBM/SEC SQFT
T_{14}/T_{11}	P_{14}/P_{11}	η_{ad}	η_p	$\frac{W\sqrt{\theta}}{\delta A_{13}}$

STATOR

SPEED CODE ①

SL	EPSI-1 DEGREE	EPSI-2 DEGREE	V-1 FT/SEC	V-2 FT/SEC	VM-1 FT/SEC	VM-2 FT/SEC	Vθ-1 FT/SEC	Vθ-2 FT/SEC	B-1 DEGREE	B-2 DEGREE	M-1	M-2	PT2/PT1	TT2/TT1
②	ϵ_{15}	ϵ_{16}	V_{15}	V_{16}	V_{m15}	V_{m16}	$V_{\theta 15}$	$V_{\theta 16}$	β_{15}	β_{16}	M_{15}	M_{16}	P_{16}/P_{13}	T_{14}/T_{13}

SL	INCS DEGREE	INCM DEGREE	DEV DEGREE	TURN DEGREE	RHOVM-1	RHOVM-2	D-FAC	OMEGA-B TOTAL	LOSS-P TOTAL	PT2/PT1	%EFF-P STATC-ST	%EFF-A TOT-STG	%EFF-P TOT-STG
②	i_{s15}	i_{m15}	δ°_{16}	$\Delta\beta$	$\rho_{15}V_{m15}$	$\rho_{16}V_{m16}$	D	$\overline{\omega}$	$\frac{\overline{\omega}\cos\beta_{16}}{2\sigma}$	P_{16}/P_{15}	η_{pS}	η_{ad}	η_p

NCORR INLET RPM	WCORR INLET LBM/SEC	TO/TO INLET	PO/PO INLET	EFF-AD INLET %	EFF-P INLET %
$N\sqrt{\theta}$	$W\sqrt{\theta}/\delta$	T_{14}/T_{11}	P_{16}/P_{11}	η_{ad}	η_p

NOTES (TABLE 5 CONTINUED)

①

CODE	% DESIGN SPEED
50	50
70	70
80	80
95	95
10	100
15	105

②

SL	% SPAN OF DESIGN STREAM-LINES AT ROTOR TRAILING EDGE	ROTOR DIAMETERS (INCHES)		STATOR DIAMETERS (INCHES)	
		INLET	EXIT	INLET	EXIT
1	5 (HUB)	17.73	20.76	21.37	22.53
2	10	18.81	21.34	21.88	22.92
3	15	19.84	21.93	22.4	23.31
4	30	22.65	23.705	24.0	24.58
5	50	26.03	26.09	26.16	26.33
6	60	27.66	27.275	27.23	27.20
7	65	28.425	27.91	27.29	27.65
8	70	29.17	28.52	28.33	28.09
9	85	31.3	30.26	29.86	29.32
10	90	32.01	30.86	30.38	29.73
11	95 (TIP)	32.63	31.45	30.87	30.09

TABLE 6.1: BLADE ELEMENT AND OVERALL PERFORMANCE - DESIGN

SPEED CODE 10

Rotor

SL	EPSI-1 DEGREE	EPSI-2 DEGREE	V-1 FT/SEC	V-2 FT/SEC	VM-1 FT/SEC	VM-2 FT/SEC	VØ-1 FT/SEC	VØ-2 FT/SEC	B-1 DEGREE	B-2 DEGREE	M-1	M-2	U-1 FT/SEC	U-2 FT/SEC	M'-1	M'-2	V'-1 FT/SEC	V'-2 FT/SEC
1	29.781	31.056	477.4	1044.7	477.4	538.0	.0	848.5	.0	57.3	.4355	.8913	964.2	1127.0	.9815	.5081	1075.9	606.7
2	25.826	27.188	517.4	981.8	517.4	565.4	.0	802.6	.0	54.6	.4739	.8226	1022.9	1160.5	1.0499	.5607	1146.5	669.2
3	21.921	23.327	555.7	961.8	555.7	573.0	.0	772.5	.0	53.2	.5104	.8048	1079.0	1192.6	1.1147	.5945	1213.7	710.6
4	11.310	12.627	639.3	912.0	639.3	562.1	.0	718.1	.0	51.9	.5922	.7577	1231.8	1289.1	1.2856	.6657	1387.8	801.3
5	-1.295	2.010	705.9	861.9	705.9	544.9	.0	667.8	.0	50.8	.6590	.7097	1415.6	1418.8	1.4767	.7640	1581.8	927.9
6	-7.043	-2.708	720.3	843.6	720.3	541.4	.0	646.9	.0	50.0	.6736	.6920	1504.2	1483.3	1.5597	.8173	1667.8	996.9
7	-9.106	-5.417	718.0	837.2	718.0	538.8	.0	640.7	.0	49.8	.6713	.6851	1545.8	1517.8	1.5935	.8423	1704.4	1029.4
8	-11.097	-7.422	710.8	832.7	710.8	537.2	.0	636.3	.0	49.6	.6640	.6798	1586.3	1551.0	1.6238	.8659	1738.3	1060.7
9	-17.421	-19.812	679.5	818.6	679.5	504.3	.0	649.9	.0	51.5	.6323	.6608	1702.2	1695.6	1.7056	.9046	1832.8	1120.6
10	-19.209	-17.341	669.9	819.7	669.9	463.1	.0	670.3	.0	54.8	.6177	.6521	1740.8	1678.3	1.7311	.8878	1863.4	1109.2
11	-19.913	-16.139	655.9	812.9	655.9	387.0	.0	719.9	.0	61.1	.6087	.6426	1774.5	1710.3	1.7567	.8442	1891.9	1068.0

SL	INCS DEGREE	INCH DEGREE	DEV DEGREE	TURN DEGREE	RHOVM-1	RHOVM-2	D-FAC	OMEGA-A TOTAL	LOSS-P TOTAL	PT2/ PT1	ØEFF-P TOT-ST	ØEFF-A TOT-ST	B'-1 DEGREE	B'-2 DEGREE	VØ'-1 FT/SEC	VØ'-2 FT/SEC
1	.50	4.71	14.25	35.83	33.27	52.90	.6156	.2143	.0403	2.3400	90.55	89.37	63.06	27.23	-969.2	-280.5
2	.69	4.42	12.69	30.57	35.48	56.74	.5843	.1455	.0275	2.3400	92.80	91.91	62.64	32.06	-1022.9	-357.9
3	.57	4.11	11.35	26.30	37.43	58.38	.5732	.1151	.0219	2.3400	93.70	92.92	62.29	36.00	-1079.0	-420.1
4	1.24	3.79	10.53	17.32	41.27	59.11	.5643	.0990	.0184	2.3400	93.30	92.47	62.38	45.35	-1231.8	-571.0
5	1.41	3.41	8.74	9.45	43.84	58.84	.5388	.1305	.0184	2.3400	91.42	90.35	63.50	54.05	-1415.6	-751.0
6	1.27	3.10	6.97	7.49	44.33	58.96	.5207	.1119	.0187	2.3400	90.41	89.22	64.47	56.98	-1504.2	-836.4
7	1.22	2.94	6.66	6.85	44.26	58.74	.5133	.1209	.0198	2.3400	89.35	88.03	65.15	58.30	-1545.8	-877.1
8	1.15	2.76	6.55	6.54	44.01	58.55	.5049	.1319	.0212	2.3400	88.21	86.75	65.91	59.37	-1586.3	-914.7
9	.55	2.05	6.12	5.36	42.88	54.63	.4986	.1881	.0273	2.3400	82.82	80.70	68.15	62.85	-1702.2	-1000.8
10	.39	1.39	5.26	4.34	42.31	49.67	.5157	.2349	.0314	2.3400	78.77	76.15	68.91	64.87	-1740.8	-1007.9
11	.38	1.83	5.23	1.06	41.95	40.81	.5501	.3023	.0345	2.3400	73.32	70.03	69.47	68.41	-1774.5	-995.4

TO/TO INLET	PO/PO INLET	EFF-AD INLET %	EFF-P INLET %	C1/A1 LBM/SEC SQFT
1.3166	2.3403	86.8	88.13	38.95

SPEED CODE 10

Stator

SL	EPSI-1 DEGREE	EPSI-2 DEGREE	V-1 FT/SEC	V-2 FT/SEC	VM-1 FT/SEC	VM-2 FT/SEC	VØ-1 FT/SEC	VØ-2 FT/SEC	B-1 DEGREE	B-2 DEGREE	M-1	M-2	PT2/ PT1	TT2/ TT1
1	26.850	4.963	1036.3	883.0	831.3	883.0	871.8	.0	54.6	.0	.8721	.5519	2.2199	1.3093
2	23.210	4.501	1011.7	685.2	642.0	685.2	781.2	.0	52.2	.0	.8514	.5555	2.2436	1.2976
3	19.778	4.202	991.2	689.5	640.9	686.5	756.1	.0	50.9	.0	.8327	.5572	2.2610	1.2982
4	10.785	3.084	941.8	683.7	619.1	680.7	709.6	.0	49.2	.0	.7853	.5518	2.2851	1.2970
5	2.318	1.223	895.8	680.7	599.0	680.7	666.1	.0	48.0	.0	.7406	.5502	2.2971	1.3090
6	-1.101	.289	880.7	684.3	596.7	684.3	647.8	.0	47.4	.0	.7256	.5541	2.3012	1.3081
7	-2.328	-.974	877.1	693.7	596.6	690.7	645.3	.0	47.2	.0	.7211	.5570	2.3028	1.3120
8	-3.773	-1.635	875.2	695.5	598.1	695.5	639.0	.0	46.9	.0	.7181	.5599	2.3033	1.3172
9	-10.037	-2.764	878.7	718.3	590.9	716.3	650.4	.0	48.0	.0	.7145	.5715	2.2979	1.3444
10	-12.407	-3.120	886.6	729.5	569.4	729.5	679.6	.0	50.5	.0	.7154	.5767	2.2930	1.3706
11	-15.261	-3.987	895.3	748.0	514.6	748.0	733.2	.0	55.5	.0	.7136	.5831	2.2877	1.4118

SL	INCS DEGREE	INCH DEGREE	DEV DEGREE	TURN DEGREE	RHOVM-1	RHOVM-2	D-FAC	OMEGA-A TOTAL	LOSS-P TOTAL	PT2/ PT1	ØEFF-P STATC-ST	%EFF-A TOT-STG	%EFF-P TOT-STG
1	1.01	3.99	13.71	59.65	60.74	76.61	.5180	.1320	.0305	.9485	81.47	83.63	86.33
2	0.02	3.20	11.88	52.22	63.16	78.00	.4993	.1095	.0257	.9588	83.89	87.08	88.49
3	-.07	2.51	10.88	50.91	64.00	78.84	.4858	.0926	.0222	.9662	85.70	88.73	89.93
4	-3.77	0.47	10.00	49.20	63.88	79.12	.4645	.0709	.0178	.9765	87.84	89.47	90.61
5	-5.93	-.59	10.07	48.04	63.39	79.17	.4399	.0602	.0163	.9817	87.96	88.04	89.34
6	-6.46	-.73	10.10	47.36	63.59	79.56	.4259	.0562	.0157	.9834	87.89	87.07	88.48
7	-6.64	-.77	10.18	47.15	63.57	79.76	.4209	.0544	.0154	.9841	87.81	86.04	87.56
8	-6.68	-.86	10.29	46.92	63.66	79.89	.4171	.0541	.0156	.9843	87.98	84.68	86.39
9	-7.76	-1.54	12.76	44.01	61.97	79.94	.4141	.0673	.0187	.9820	84.35	77.77	80.17
10	-7.62	-1.38	14.86	53.45	59.79	79.46	.4217	.0695	.0211	.9799	81.93	72.11	75.10
11	-8.61	-2.03	17.11	55.53	51.83	78.64	.4343	.0778	.0239	.9777	78.57	64.55	68.33

NCORR INLET RPM	WCORR INLET LBM/SEC	TO/TO INLET	PO/PO INLET	EFF-AD INLET %	EFF-P INLET %
12964.	173.83	1.3166	2.2846	84.0	85.64

TABLE 6.2: BLADE ELEMENT AND OVERALL PERFORMANCE WITH UNIFORM INLET

Rotor

RUN N0908, SPEED CODE 70, POINT NO 3

SL	EPSI-1 DEGREE	EPSI-2 DEGREE	V-1 FT/SEC	V-2 FT/SEC	VM-1 FT/SEC	VM-2 FT/SEC	VO-1 FT/SEC	VO-2 FT/SEC	B-1 DEGREE	B-2 DEGREE	M-1	M-2	U-1 FT/SEC	U-2 FT/SEC	M'-1	M'-2	V'-1 FT/SEC	V'-2 FT/SEC
1	29.175	31.013	300.1	762.7	300.1	508.4	.0	568.6	.0	47.8	.2780	.6666	673.1	788.2	.6682	.4841	740.3	553.8
2	24.825	26.954	331.1	730.9	331.1	507.7	.0	525.8	.0	45.6	.2991	.6387	714.2	810.2	.7112	.5085	787.2	582.0
3	20.560	23.159	351.2	690.4	351.2	489.9	.0	492.1	.0	44.8	.3177	.6058	753.3	832.6	.7517	.5205	831.1	596.6
4	9.676	12.199	389.0	643.5	389.0	460.2	.0	441.4	.0	43.2	.3527	.5596	859.9	900.0	.8556	.5700	943.8	655.4
5	-2.628	1.194	408.8	615.2	408.8	444.5	.0	425.3	.0	43.7	.3711	.5317	988.3	99?.6	.9708	.6214	1069.5	719.1
6	-7.933	-3.813	409.1	603.3	409.1	421.8	.0	431.3	.0	45.5	.3713	.5188	1050.2	1035.5	1.0230	.6337	1127.0	736.9
7	-10.831	-6.018	406.8	596.0	406.8	418.7	.0	424.0	.0	45.2	.3692	.5120	1079.2	1059.6	1.0467	.6539	1153.3	761.2
8	-12.226	-8.320	403.6	584.3	403.6	418.3	.0	407.8	.0	44.1	.3662	.5020	1107.5	1082.8	1.0696	.6823	1178.7	794.1
9	-17.298	-15.348	391.0	523.1	391.0	368.4	.0	371.4	.0	44.8	.3545	.4482	1188.4	1148.9	1.1342	.7371	1251.0	860.3
10	-18.185	-17.514	386.4	508.5	386.4	348.8	.0	370.0	.0	46.1	.3503	.4348	1215.3	1171.7	1.1559	.7474	1275.3	874.2
11	-18.519	-18.982	383.4	500.9	383.4	336.2	.0	371.3	.0	47.3	.3474	.4274	1238.9	1194.1	1.1752	.7584	1296.8	888.8

SL	INCS DEGREE	INCM DEGREE	DEV DEGREE	TURN DEGREE	RHOVM-1	RHOVM-2	D-FAC	OMEGA-B TOTAL	LOSS-P TOTAL	PT2/ PT1	%EFF-P TOT-ST	%EFF-A TOT-ST	B'-1 DEGREE	B'-2 DEGREE	VO'-1 FT/SEC	VO'-2 FT/SEC
1	2.14	6.36	10.10	41.62	22.68	43.71	.4364	.0254	.0049	1.5910	98.72	98.6.	64.71	23.09	-673.1	-219.6
2	2.91	6.24	9.53	35.50	24.22	43.47	.4323	.0072	.0014	1.5629	99.50	99.4	64.46	28.96	-714.2	-284.4
3	2.65	6.19	9.89	29.85	25.55	42.37	.4403	.0264	.0051	1.5283	98.04	97.94	64.37	34.52	-753.3	-340.5
4	4.23	6.73	9.44	21.10	27.98	40.56	.4430	.0598	.0113	1.4866	94.40	94.11	65.37	44.26	-859.9	-458.6
5	5.45	7.46	6.51	15.73	29.21	38.36	.4515	.1318	.0239	1.4619	85.61	84.85	67.55	51.82	-980.3	-565.2
6	5.61	7.44	4.99	13.81	29.23	35.89	.4666	.1843	.0323	1.4501	79.25	78.16	68.80	54.99	-1050.2	-604.2
7	5.53	7.25	4.87	12.95	29.09	35.58	.4573	.1896	.0326	1.4447	78.00	76.87	69.46	56.91	-1079.2	-635.6
8	5.33	6.94	9.24	12.04	28.89	35.59	.4375	.1809	.0302	1.4364	78.04	76.92	70.09	58.05	-1107.5	-676.0
9	4.10	5.60	7.58	7.39	28.10	31.31	.4053	.1913	.0264	1.3946	74.03	72.81	71.70	64.31	-1188.4	-777.4
10	3.63	5.03	6.46	6.02	27.82	29.61	.4030	.2057	.0263	1.3874	71.79	70.49	72.09	66.07	-1215.3	-801.6
11	3.37	4.87	4.21	5.06	27.62	28.53	.3998	.2175	.0259	1.3864	70.15	68.78	72.46	67.40	-1238.9	-822.8

TO/TO INLET	PO/PO INLET	EFF-AD INLET %	EFF-P INLET %	WCI/AI INLET LBM/SEC SQFT
1.1365	1.4668	84.75	85.53	26.14

Stator

RUN .0908, SPEED CODE 70, POINT NO 3

SL	EPSI-1 DEGREE	EPSI-2 DEGREE	V-1 FT/SEC	V-2 FT/SEC	VM-1 FT/SEC	VM-2 FT/SEC	VO-1 FT/SEC	VO-2 FT/SEC	B-1 DEGREE	B-2 DEGREE	M-1	M-2	PT2/ PT1	TT2/ TT1
1	27.641	4.857	802.8	736.3	584.9	735.7	549.9	-29.3	45.8	-2.2	.7052	.6418	1.4903	1.1431
2	24.466	4.465	763.8	737.3	560.9	735.9	509.7	-45.2	43.8	-3.4	.6702	.6450	1.5131	1.1356
3	21.406	4.036	728.9	714.2	547.6	712.2	481.1	-53.6	42.8	-4.2	.6384	.6245	1.5022	1.1313
4	12.515	2.689	675.6	656.4	516.0	654.1	436.2	-54.1	40.7	-4.7	.5894	.5714	1.4725	1.1278
5	3.016	.489	647.2	620.2	489.0	619.4	424.0	-31.8	41.0	-2.9	.5610	.5359	1.4496	1.1366
6	-.455	-.723	637.4	610.8	469.0	610.4	431.6	-21.9	42.6	-2.1	.5498	.5253	1.4391	1.1445
7	-2.309	-1.355	631.7	606.3	466.3	605.7	426.2	-26.9	42.4	-2.5	.5445	.5214	1.4331	1.1437
8	-4.346	-1.927	622.8	598.5	467.5	597.3	411.5	-37.8	41.4	-3.6	.5369	.5152	1.4237	1.1403
9	-11.441	-2.891	577.1	556.1	437.6	553.9	376.3	-54.6	41.1	-5.6	.4966	.4775	1.3741	1.1382
10	-14.392	-3.188	570.5	552.7	428.6	549.6	376.5	-58.1	41.9	-6.0	.4901	.4737	1.3638	1.1412
11	-17.103	-3.426	570.0	559.5	425.5	556.0	379.4	-62.4	42.6	-6.3	.4889	.4794	1.3614	1.1430

SL	INCS DEGREE	INCM DEGREE	DEV DEGREE	TURN DEGREE	RHOVM-1	RHOVM-2	D-FAC	OMEGA-B TOTAL	LOSS-P TOTAL	PT2/ PT1	%EFF-P STATC-ST	%EFF-A TOT-STG	%EFF-P TOT-STG
1	-5.36	-2.37	13.99	48.0C	49.05	60.17	.2447	.2176	.0502	.9381	-20.21	84.50	85.31
2	-5.06	-2.68	10.94	47.28	48.10	61.40	.1998	.1037	.0243	.9727	-44.14	92.67	93.06
3	-6.46	-3.05	9.10	47.05	46.44	59.93	.1924	.0643	.0154	.9844	-44.20	93.94	94.25
4	-9.78	-5.54	7.80	45.38	43.97	55.76	.2082	.0397	.0100	.9917	30.23	91.50	91.92
5	-10.50	-5.16	9.63	43.91	41.35	52.54	.2312	.0371	.0100	.9929	57.25	82.04	82.92
6	-8.69	-2.97	10.55	44.68	39.29	51.32	.2392	.0335	.0093	.9938	60.52	75.86	77.03
7	-8.86	-2.99	10.14	44.98	39.00	50.85	.2397	.0368	.0104	.9933	54.02	75.39	76.58
8	-9.91	-3.92	9.18	45.02	39.12	50.11	.2363	.0314	.0090	.9945	50.10	75.73	76.88
9	-12.18	-5.96	9.65	46.70	36.46	45.71	.2582	.0773	.0230	.9882	-15.97	68.80	70.13
10	-13.63	-7.38	11.35	47.94	35.[illegible]	45.01	.2665	.1094	.0330	.9835	-67.38	65.66	67.09
11	-18.56	-12.42	13.28	48.97	[illegible]	45.26	.2591	.1187	.0363	.9821	-199.09	64.44	65.92

NCORR INLET RPM	WCORR INLET LBM/SEC	I	EFF-AD INLET %	EFF-P INLET %
8702.	116.63	1..	.28	82.19

TABLE 6.3: BLADE ELEMENT AND OVERALL PERFORMANCE WITH UNIFORM INLET

Rotor

RUN NO908, SPEED CODE 70, POINT NO 5

SL	EPSI-1 DEGREE	EPSI-2 DEGREE	V-1 FT/SEC	V-2 FT/SEC	VM-1 FT/SEC	VM-2 FT/SEC	VO-1 FT/SEC	VO-2 FT/SEC	B-1 DEGREE	B-2 DEGREE	M-1	M-2	U-1 FT/SEC	U-2 FT/SEC	M'-1	M'-2	V'-1 FT/SEC	V'-2 FT/SEC
1	29.208	30.773	285.4	753.0	285.4	470.9	.0	587.1	.0	50.9	.2573	.6559	674.4	789.7	.6601	.4462	732.3	512.3
2	24.031	26.614	307.4	725.7	307.4	477.7	.0	546.3	.0	48.4	.2774	.6321	715.5	811.7	.7027	.4760	778.7	546.4
3	20.402	22.859	326.8	696.4	326.8	467.7	.0	515.9	.0	47.4	.2952	.6050	754.7	834.2	.7428	.4921	822.4	565.7
4	9.052	12.126	360.7	643.0	360.7	420.6	.0	479.4	.0	48.1	.3264	.5563	861.5	901.7	.8453	.5205	934.0	601.7
5	-3.086	1.203	377.1	618.3	377.1	400.4	.0	471.1	.0	49.6	.3416	.5308	990.1	992.4	.9598	.5643	1059.5	657.3
6	-8.213	-3.537	377.6	615.6	377.6	384.2	.0	481.0	.0	51.3	.3421	.5260	1052.1	1037.5	1.0126	.5777	1117.8	676.2
7	-10.380	-5.971	375.8	611.3	375.8	382.2	.0	477.0	.0	51.2	.3404	.5215	1081.2	1061.6	1.0368	.5959	1144.6	698.5
8	-12.472	-8.307	373.0	601.2	373.0	380.4	.0	465.6	.0	50.6	.3378	.5126	1109.5	1084.8	1.0601	.6196	1170.6	726.8
9	-17.426	-15.390	361.8	552.2	361.8	329.9	.0	442.9	.0	52.9	.3274	.4685	1190.6	1151.0	1.1261	.6628	1244.3	781.2
10	-18.206	-17.558	357.8	540.4	357.8	315.2	.0	439.0	.0	53.8	.3238	.4578	1217.6	1173.8	1.1483	.6773	1269.1	799.6
11	-18.898	-19.033	355.2	529.8	355.2	299.1	.0	437.2	.0	55.1	.3214	.4479	1241.2	1196.3	1.1679	.6897	1291.0	815.9

SL	INCS DEGREE	INCM DEGREE	DEV DEGREE	TURN DEGREE	RHOVM-1	RHOVM-2	D-FAC	OMEGA-B TOTAL	LOSS-P TOTAL	PT2/ PT1	%EFF-P TOT-ST	%EFF-A TOT-ST	B'-1 DEGREE	B'-2 DEGREE	VO'-1 FT/SEC	VO'-2 FT/SEC
1	3.84	8.05	9.90	43.51	21.12	41.32	.4925	.0141	.0027	1.6207	99.35	99.33	66.40	22.89	-674.4	-202.0
2	4.16	7.89	9.26	37.42	22.63	42.20	.4786	-.0138	-.0027	1.5995	100.82	100.90	66.11	28.68	-715.5	-265.4
3	4.24	7.78	9.26	32.06	23.94	41.42	.4792	-.0043	-.0008	1.5739	100.11	100.14	65.96	33.90	-754.7	-318.2
4	5.83	8.33	9.60	22.54	26.17	37.90	.5059	.0753	.0142	1.5299	93.52	93.15	66.97	44.43	-861.5	-422.3
5	7.08	9.09	7.16	16.70	27.23	35.11	.5172	.1565	.0280	1.5123	84.59	83.70	69.17	52.48	-990.1	-521.3
6	7.15	8.98	5.28	15.06	27.26	33.47	.5299	.2032	.0354	1.5120	79.49	78.29	70.35	55.29	-1052.1	-556.4
7	7.02	8.74	5.06	14.25	27.14	33.27	.5221	.2106	.0360	1.5105	78.22	76.95	70.95	56.70	-1081.2	-584.6
8	6.78	8.39	5.47	13.26	26.96	33.14	.5063	.2087	.0346	1.5045	77.66	76.37	71.54	58.28	-1109.5	-619.3
9	5.42	6.92	7.97	8.33	26.24	28.69	.4830	.2330	.0317	1.4734	73.06	71.58	73.03	64.69	-1190.6	-708.1
10	4.81	6.31	6.76	7.00	25.98	27.43	.4760	.2400	.0304	1.4691	71.78	70.28	73.38	66.38	-1217.6	-734.8
11	4.61	6.11	4.94	5.57	25.81	26.04	.4695	.2501	.0289	1.4665	70.47	68.87	73.70	68.13	-1241.2	-759.0

TO/TO INLET	PO/PO INLET	EFF-AD INLET %	EFF-P INLET %	WC1/A1 LBM/SEC SQFT
1.1520	1.5232	84.05	84.94	24.40

Stator

RUN NO908, SPEED CODE 70, POINT NO 5

SL	EPSI-1 DEGREE	EPSI-2 DEGREE	V-1 FT/SEC	V-2 FT/SEC	VM-1 FT/SEC	VM-2 FT/SEC	VO-1 FT/SEC	VO-2 FT/SEC	B-1 DEGREE	B-2 DEGREE	M-1	M-2	PT2/ PT1	TT2/ TT1
1	27.404	4.974	784.8	651.7	541.1	651.6	568.4	-11.5	48.9	-1.0	.6863	.5618	1.5348	1.1481
2	24.267	4.656	751.7	645.9	533.5	644.9	529.5	-35.5	46.7	-3.1	.6569	.5582	1.5458	1.1412
3	21.402	4.291	722.7	624.0	517.0	622.3	505.0	-47.1	45.8	-4.3	.6306	.5390	1.5358	1.1381
4	13.022	3.099	667.5	572.1	470.2	570.4	473.8	-43.1	45.8	-4.3	.5788	.4916	1.5126	1.1391
5	4.368	.863	642.8	543.8	439.3	543.4	469.3	-22.4	47.0	-2.4	.5532	.4637	1.4995	1.1513
6	.312	-.417	641.8	544.6	424.8	544.5	481.0	-11.0	48.5	-1.2	.5497	.4623	1.4992	1.1615
7	-1.864	-1.105	639.1	543.8	423.2	543.7	478.9	-13.2	48.5	-1.4	.5466	.4613	1.4970	1.1627
8	-3.926	-1.741	631.6	537.1	423.0	536.7	469.0	-19.9	48.0	-2.1	.5399	.4556	1.4894	1.1616
9	-11.276	-2.835	595.0	493.8	390.7	491.5	448.7	-47.1	49.3	-5.5	.5066	.4170	1.4448	1.1646
10	-14.841	-3.156	589.2	487.4	384.6	484.9	446.4	-49.9	49.9	-5.8	.5010	.4110	1.4344	1.1670
11	-17.231	-3.397	584.5	490.6	377.5	487.7	446.3	-52.4	50.7	-6.1	.4962	.4134	1.4306	1.1685

SL	INCS DEGREE	INCM DEGREE	DEV DEGREE	TURN DEGREE	RHOVM-1	RHOVM-2	D-FAC	OMEGA-B TOTAL	LOSS-P TOTAL	PT2/ PT1	%EFF-P STATIC-ST	%EFF-A TOT-STG	%EFF-P TOT-STG
1	-2.25	.74	15.22	49.88	46.59	57.16	.3350	.1907	.0440	.9482	47.88	87.96	88.64
2	-2.98	.20	11.29	49.81	46.36	57.43	.3125	.1206	.0283	.9696	60.25	93.88	94.22
3	-3.43	-.02	9.07	50.10	45.09	55.75	.3164	.0959	.0229	.9772	67.36	94.43	94.73
4	-4.71	-.46	8.20	50.06	41.06	51.48	.3359	.0520	.0131	.9895	82.46	90.25	90.77
5	-4.52	.82	10.21	49.31	38.09	48.72	.3617	.0449	.0121	.9916	85.82	81.22	82.23
6	-2.77	2.96	11.45	49.70	36.58	48.41	.3670	.0456	.0127	.9916	85.31	75.95	77.25
7	-2.76	3.11	11.29	49.92	36.38	48.24	.3662	.0458	.0130	.9916	84.83	75.09	76.43
8	-3.32	2.67	10.68	50.10	36.37	47.54	.3671	.0449	.0125	.9920	84.70	74.57	75.93
9	-3.84	2.28	9.80	54.78	33.39	42.82	.4197	.1120	.0334	.9822	66.40	67.37	68.98
10	-5.68	.57	11.51	55.73	32.79	41.95	.4301	.1440	.0435	.9776	57.32	65.02	66.71
11	-10.51	-4.37	13.55	56.75	32.13	41.99	.4249	.1573	.0481	.9757	50.70	63.94	65.68

NCORR INLET RPM	WCORR INLET LBM/SEC	TO/TO INLET	PO/PO INLET	EFF-AD INLET %	EFF-P INLET %
8718.	100.87	1.1520	1.4973	80.43	81.48

TABLE 6.4: BLADE ELEMENT AND OVERALL PERFORMANCE WITH UNIFORM INLET

Rotor

RUN NO908, SPEED CODE 10, POINT NO 1

SL	EPSI-1 DEGREE	EPSI-2 DEGREE	V-1 FT/SEC	V-2 FT/SEC	VM-1 FT/SEC	VM-2 FT/SEC	Vθ-1 FT/SEC	Vθ-2 FT/SEC	B-1 DEGREE	B-2 DEGREE	M-1	M-2	U-1 FT/SEC	U-2 FT/SEC	M'-1	M'-2	V'-1 FT/SEC	V'-2 FT/SEC
1	29.411	31.175	497.9	1030.6	497.9	672.2	.0	781.2	.0	49.0	.4550	.8758	961.7	1126.0	.9895	.6421	1083.0	755.5
2	25.236	27.266	544.4	1018.3	544.4	676.4	.0	761.2	.0	48.1	.4995	.8636	1020.3	1157.5	1.0610	.6649	1156.4	783.9
3	20.996	23.629	587.0	993.8	587.0	674.0	.0	730.4	.0	47.1	.5407	.8415	1076.1	1189.5	1.1293	.6905	1225.8	815.5
4	9.772	13.153	670.5	918.7	670.5	649.6	.0	649.7	.0	45.0	.6233	.7736	1228.6	1285.8	1.3011	.7656	1399.6	909.2
5	-2.450	2.199	718.9	828.1	718.9	573.5	.0	597.3	.0	46.2	.6722	.6886	1411.9	1415.1	1.4815	.8307	1584.4	998.9
6	-7.266	-2.689	726.3	808.8	726.3	568.1	.0	575.8	.0	45.3	.6798	.6706	1500.3	1479.4	1.5601	.8849	1666.9	1067.4
7	-9.490	-5.166	724.6	807.7	724.6	580.8	.0	561.2	.0	43.9	.6780	.6697	1541.8	1513.9	1.5941	.9251	1703.6	1115.7
8	-11.777	-7.556	719.7	800.3	719.7	586.3	.0	544.7	.0	42.7	.6730	.6637	1582.2	1547.0	1.6255	.9630	1738.2	1161.2
9	-17.952	-15.118	691.1	729.0	691.1	532.8	.0	497.5	.0	42.6	.6440	.6022	1697.7	1641.3	1.7081	1.0424	1833.0	1261.8
10	-19.203	-17.500	679.7	692.6	679.7	479.4	.0	499.9	.0	45.6	.6325	.5687	1736.3	1673.9	1.7351	1.0411	1864.6	1268.1
11	-19.158	-19.160	674.3	645.3	674.3	401.1	.0	505.6	.0	51.1	.6270	.5258	1769.9	1705.9	1.7614	1.0311	1894.0	1265.6

SL	INCS DEGREE	INCM DEGREE	DEV DEGREE	TURN DEGREE	RHOVM-1	RHOVM-2	D-FAC	OMEGA-B TOTAL	LOSS-P TOTAL	PT2/ PT1	%EFF-P TOT-ST	%EFF-A TOT-ST	B'-1 DEGREE	B'-2 DEGREE	Vθ'-1 FT/SEC	Vθ'-2 FT/SEC
1	-.64	3.58	13.90	35.04	34.41	64.70	.4750	.0853	.0159	2.3053	95.90	95.41	61.93	26.89	-961.7	-344.9
2	-.68	3.05	10.70	31.14	36.86	65.50	.4898	.0837	.0161	2.2992	95.46	94.91	61.27	30.13	-1020.3	-396.3
3	-.95	2.59	9.45	26.69	38.94	65.57	.4923	.0827	.0161	2.2662	94.95	94.36	60.77	34.08	-1076.1	-459.2
4	-.08	2.42	9.54	16.69	42.53	63.39	.4858	.1029	.0194	2.1470	91.84	90.94	61.06	44.36	-1228.6	-636.1
5	.94	2.95	9.66	8.06	44.29	54.96	.4866	.1858	.0313	1.9980	82.33	80.57	63.03	54.98	-1411.9	-817.8
6	1.04	2.86	7.73	6.49	44.54	54.36	.4674	.1951	.0319	1.9756	80.44	78.52	64.23	57.74	-1500.3	-903.6
7	.98	2.70	6.84	6.43	44.48	55.76	.4493	.1861	.0303	1.9799	80.88	79.00	64.91	58.48	-1541.8	-952.6
8	.08	2.49	6.66	6.17	44.31	56.45	.4319	.1780	.0285	1.9749	81.18	79.33	65.64	59.47	-1582.2	-1002.3
9	.22	1.72	7.94	3.15	43.31	51.33	.3972	.1869	.0255	1.8940	78.36	76.38	67.82	64.66	-1697.7	-1143.8
10	-.14	1.36	7.78	1.04	42.88	45.80	.4024	.2218	.0269	1.8538	74.11	71.81	68.43	67.39	-1736.3	-1174.0
11	-.28	1.22	8.03	-2.41	42.68	37.91	.4119	.2651	.0265	1.8048	69.00	66.37	68.81	71.22	-1769.9	-1200.3

TO/TO INLET	PO/PO INLET	EFF-AD INLET %	EFF-P INLET %	WC1/A1 LBM/SEC SQFT
1.2715	2.0511	83.78	85.31	39.85

Stator

RUN NO908, SPEED CODE 10, POINT NO 1

SL	EPSI-1 DEGREE	EPSI-2 DEGREE	V-1 FT/SEC	V-2 FT/SEC	VM-1 FT/SEC	VM-2 FT/SEC	Vθ-1 FT/SEC	Vθ-2 FT/SEC	B-1 DEGREE	B-2 DEGREE	M-1	M-2	PT2/ PT1	TT2/ TT1
1	27.876	4.972	1090.6	982.5	782.9	975.9	759.3	-113.5	46.7	-6.5	.9354	.8291	1.9141	1.2820
2	24.888	4.627	1071.0	1029.3	773.0	1023.2	741.4	-111.6	45.9	-6.1	.9158	.8744	2.0525	1.2823
3	22.023	4.120	1044.4	1045.3	762.1	1038.7	714.2	-117.4	44.8	-6.3	.8910	.8917	2.1298	1.2784
4	13.752	2.458	968.3	980.5	725.1	973.9	641.7	-113.9	42.1	-6.6	.8207	.8325	2.0898	1.2678
5	4.516	.059	881.4	894.1	649.7	885.7	595.6	-122.4	42.6	-7.9	.7376	.7493	1.9657	1.2714
6	-.085	-1.112	864.2	880.9	643.6	872.3	576.7	-122.7	41.9	-8.0	.7210	.7364	1.9397	1.2730
7	-2.264	-1.673	864.1	883.5	654.6	875.5	564.0	-118.8	40.8	-7.7	.7211	.7394	1.9376	1.2715
8	-4.188	-2.192	860.1	882.5	662.1	873.2	549.0	-128.0	39.7	-8.3	.7181	.7394	1.9274	1.2686
9	-10.445	-3.108	812.5	834.1	637.9	824.0	503.2	-129.5	38.6	-8.9	.6773	.6959	1.8130	1.2651
10	-13.198	-3.358	789.1	785.9	604.0	775.8	507.8	-125.2	40.6	-9.1	.6542	.6498	1.7267	1.2734
11	-16.537	-3.444	756.8	769.8	553.9	759.0	515.7	-128.0	43.8	-9.5	.6230	.6341	1.6870	1.2778

SL	INCS DEGREE	INCM DEGREE	DEV DEGREE	TURN DEGREE	RHOVM-1	RHOVM-2	D-FAC	OMEGA-B TOTAL	LOSS-P TOTAL	PT2/ PT1	%EFF-P STATC-ST	%EFF-A TOT-STG	%EFF-P TOT-STG
1	-4.40	-1.42	9.76	53.19	71.94	80.70	.2809	.3924	.0901	.8303	-68.14	72.11	74.48
2	-3.82	-.64	8.28	51.98	71.84	87.72	.2249	.2536	.0593	.5930	-523.51	80.63	82.44
3	-4.49	-1.08	6.98	51.13	71.34	91.50	.1891	.1472	.0350	.9401	*******	86.45	87.79
4	-8.34	-4.10	5.87	48.76	68.42	88.72	.1801	.0656	.0165	.9766	252.57	87.38	88.60
5	-8.89	-3.55	4.70	50.45	60.35	80.26	.2019	.0456	.0122	.9863	194.25	78.36	80.28
6	-9.45	-3.73	4.59	49.87	59.64	78.57	.2063	.0654	.0181	.9809	234.38	76.20	78.27
7	-10.53	-4.67	4.95	48.49	60.81	78.72	.2010	.0767	.0215	.9775	237.15	76.50	78.54
8	-11.60	-5.61	4.46	48.04	61.65	78.27	.1920	.0685	.0195	.9804	179.33	76.65	78.66
9	-14.70	-8.48	6.36	47.46	58.91	71.66	.1986	.1262	.0374	.9677	227.39	69.82	72.19
10	-15.02	-8.77	8.24	49.66	54.97	65.64	.2339	.2252	.0675	.9471	738.92	61.72	64.47
11	-17.43	-11.29	10.15	53.24	49.65	63.16	.2471	.2821	.0855	.9351	826.01	57.92	60.84

NCORR INLET RPM	WCORR INLET LBM/SEC	TO/TO INLET	PO/PO INLET	EFF-AD INLET %	EFF-P INLET %
12431.	177.79	1.2715	1.9633	78.18	80.12

TABLE 6.5: BLADE ELEMENT AND OVERALL PERFORMANCE WITH UNIFORM INLET

Rotor

RUN NO908, SPEED CODE 10, POINT NO 6

SL	EPSI-1 DEGREE	EPSI-2 DEGREE	V-1 FT/SEC	V-2 FT/SEC	VM-1 FT/SEC	VM-2 FT/SEC	V0-1 FT/SEC	V0-2 FT/SEC	B-1 DEGREE	B-2 DEGREE	M-1	M-2	U-1 FT/SEC	U-2 FT/SEC	M'-1	M'-2	V'-1 FT/SEC	V'-2 FT/SEC
1	29.378	31.292	491.9	1031.2	491.9	620.0	.0	824.0	.0	52.8	.4492	.8703	963.8	1128.5	.9882	.5829	1082.1	690.7
2	25.118	27.429	533.0	1001.7	533.0	628.2	.0	780.2	.0	50.9	.4885	.8447	1022.5	1160.0	1.0569	.6191	1153.1	734.1
3	20.848	23.751	570.6	974.1	570.6	618.7	.0	752.4	.0	50.4	.5248	.8193	1078.5	1192.1	1.1222	.6384	1220.1	759.0
4	9.860	12.967	645.0	916.1	645.0	572.0	.0	715.6	.0	51.3	.5978	.7619	1231.3	1288.6	1.2884	.6734	1390.0	809.7
5	-2.296	1.947	691.7	871.9	691.7	538.7	.0	685.6	.0	51.9	.6446	.7164	1415.0	1418.3	1.4678	.7472	1575.0	909.4
6	-7.635	-2.953	697.6	865.1	697.6	535.4	.0	679.4	.0	51.7	.6506	.7069	1503.6	1482.7	1.5458	.7888	1657.6	965.3
7	-10.088	-5.501	693.8	858.9	693.8	540.6	.0	667.4	.0	50.8	.6467	.7008	1545.2	1517.2	1.5789	.8219	1693.8	1007.2
8	-12.517	-7.995	686.4	848.6	686.4	542.0	.0	652.9	.0	50.1	.6392	.6916	1585.7	1550.4	1.6092	.8546	1727.9	1048.5
9	-18.566	-15.439	652.5	791.5	652.5	452.8	.0	649.2	.0	54.7	.6053	.6366	1701.5	1644.9	1.6905	.8798	1822.3	1093.9
10	-19.486	-17.636	641.2	775.7	641.2	411.1	.0	657.8	.0	57.5	.5941	.6201	1740.1	1677.6	1.7182	.8789	1854.5	1099.5
11	-19.324	-19.184	636.0	763.1	636.0	368.5	.0	668.3	.0	60.7	.5889	.6063	1773.8	1709.6	1.7449	.8776	1884.4	1104.6

SL	INCS DEGREE	INCM DEGREE	DEV DEGREE	TURN DEGREE	RHOVM-1	RHOVM-2	D-FAC	OMEGA-B TOTAL	LOSS-P TOTAL	PT2/ PT1	%EFF-P TOT-ST	%EFF-A TOT-ST	B'-1 DEGREE	B'-2 DEGREE	V0'-1 FT/SEC	V0'-2 FT/SEC
1	-.30	3.91	12.93	36.34	34.08	62.90	.5416	.0453	.0085	2.4506	97.99	97.73	62.26	25.92	-963.8	-304.5
2	-.14	3.59	11.53	30.85	36.28	64.53	.5334	.0210	.0040	2.4192	98.91	98.77	61.80	30.95	-1022.5	-379.9
3	-.24	3.30	10.61	26.24	38.16	63.94	.5381	.0315	.0061	2.3846	98.09	97.85	61.48	35.24	-1078.5	-439.7
4	.91	3.41	10.17	17.05	41.51	59.42	.5639	.1052	.0196	2.3163	92.52	91.61	62.05	45.00	-1231.3	-573.1
5	1.87	3.88	8.37	10.28	43.33	56.09	.5551	.1626	.0283	2.2797	86.64	85.03	63.96	53.69	-1415.0	-732.7
6	1.99	3.82	6.21	8.98	43.55	55.74	.5447	.1846	.0314	2.2847	84.20	82.30	65.19	56.21	-1503.6	-803.2
7	2.01	3.73	5.76	8.54	43.41	56.41	.5295	.1848	.0310	2.2839	83.80	81.05	65.94	57.40	-1545.2	-849.8
8	1.99	3.60	5.88	8.05	43.13	56.66	.5136	.1841	.0302	2.2748	83.41	81.43	66.75	58.69	-1585.7	-897.5
9	1.46	2.96	8.50	3.83	41.82	46.69	.5120	.2512	.0335	2.1988	76.35	73.65	69.06	65.23	-1701.5	-995.8
10	1.06	2.56	8.05	1.96	41.35	42.13	.5168	.2817	.0338	2.1826	73.51	70.52	69.62	67.66	-1740.1	-1019.8
11	.88	2.38	7.01	-.23	41.13	37.56	.5211	.3114	.0327	2.1737	70.95	67.70	69.97	70.20	-1773.8	-1041.3

TO/TO INLET	PO/PO INLET	EFF-AD INLET %	EFF-P INLET %	WC1/A1 LBM/SEC SQFT
1.3153	2.2952	84.77	86.42	38.81

Stator

RUN NO908, SPEED CODE 10, POINT NO 6

SL	EPSI-1 DEGREE	EPSI-2 DEGREE	V-1 FT/SEC	V-2 FT/SEC	VM-1 FT/SEC	VM-2 FT/SEC	V0-1 FT/SEC	V0-2 FT/SEC	B-1 DEGREE	B-2 DEGREE	M-1	M-2	PT2/ PT1	TT2/ TT1
1	27.815	4.798	1072.8	782.4	716.5	782.0	798.5	-26.6	50.7	-1.9	.9114	.6405	2.2599	1.2971
2	24.773	4.420	1038.2	785.5	707.8	783.7	759.6	-53.1	49.1	-3.8	.8804	.6452	2.2972	1.2894
3	21.817	4.025	1009.7	768.2	690.0	765.5	737.1	-64.3	48.5	-4.7	.8534	.6304	2.2917	1.2877
4	13.088	2.734	949.9	730.9	634.3	729.7	707.1	-41.8	48.6	-3.3	.7934	.5955	2.2804	1.2962
5	4.007	.481	907.7	699.5	597.4	698.5	683.3	-37.1	48.9	-3.0	.7490	.5643	2.2518	1.3132
6	.054	-.686	903.2	701.5	594.4	700.9	680.1	-30.4	48.8	-2.5	.7414	.5635	2.2503	1.3239
7	-1.879	-1.274	899.0	703.7	598.9	702.9	670.4	-33.3	48.2	-2.7	.7370	.5654	2.2500	1.3241
8	-3.650	-1.817	891.9	697.9	603.1	696.9	657.1	-37.2	47.5	-3.1	.7306	.5603	2.2364	1.3245
9	-9.877	-2.893	853.0	641.8	545.3	639.0	656.0	-59.9	50.5	-5.3	.6908	.5084	2.1339	1.3464
10	-12.840	-3.224	845.5	629.2	518.1	627.3	668.1	-47.9	52.7	-4.3	.6807	.4953	2.1046	1.3600
11	-16.243	-3.463	840.7	631.6	492.3	630.2	681.5	-41.7	54.9	-3.7	.6731	.4959	2.0937	1.3676

SL	INCS DEGREE	INCM DEGREE	DEV DEGREE	TURN DEGREE	RHOVM-1	RHOVM-2	D-FAC	OMEGA-B TOTAL	LOSS-P TOTAL	PT2/ PT1	%EFF-P STATC-ST	%EFF-A TOT-STG	%EFF-P TOT-STG
1	-.47	2.52	14.31	52.56	70.40	85.54	.4434	.1838	.0424	.9233	69.70	88.13	89.39
2	-.64	2.55	10.58	52.86	70.69	87.41	.4234	.1223	.0287	.9515	77.73	92.48	93.30
3	-.79	2.62	8.60	53.21	69.47	86.05	.4259	.0993	.0237	.9621	81.50	92.75	93.53
4	-1.82	2.42	9.24	51.91	64.45	82.72	.4269	.0430	.0109	.9854	91.31	89.49	90.62
5	-2.58	2.76	9.53	51.93	60.88	78.50	.4439	.0406	.0110	.9875	91.51	83.17	84.95
6	-2.47	3.26	10.12	51.33	60.50	78.11	.4427	.0490	.0137	.9851	89.49	80.32	82.40
7	-3.06	2.80	9.97	50.94	61.03	78.24	.4380	.0489	.0138	.9852	89.22	80.26	82.34
8	-3.83	2.16	9.74	50.53	61.54	77.28	.4392	.0492	.0141	.9854	89.00	79.49	81.64
9	-2.75	3.47	9.92	55.85	54.47	68.27	.5024	.0978	.0292	.9737	80.38	69.64	72.63
10	-2.91	3.33	13.01	56.99	51.20	65.86	.5184	.1276	.0386	.9663	75.02	65.66	68.98
11	-6.31	-.17	15.87	58.63	48.23	65.44	.5159	.1410	.0432	.9633	71.68	63.75	67.23

NCORR INLET RPM	WCORR INLET LBM/SEC	TO/TO INLET	PO/PO INLET	EFF-AD INLET %	EFF-P INLET %
12459.	173.17	1.3153	2.2365	81.82	83.73

APPENDIX III

THEORY OF HOLOGRAPHIC FLOW VISUALIZATION

A. Introduction

The method of holography first described by Gabor in 1948 (16) and subsequently developed by Leith and Upatnieks (17), Stroke (18), and many others is finding increasingly widespread application to practical engineering problems.

The conventional methods like the shadowgraph, the Toepler schlieren, and the Mach-Zehnder interferometer for the observation of compressible gas flow are based on the principle that variations in gas density are accompanied by variations in index of refraction which modify light wavefronts traversing the gas. The various visualization techniques employ different means by which the modifications of the light wavefronts are made visible as intensity variations on a screen or photographic plate. In conventional visualization methods the illuminating light beam is monodirectional; consequently properties of the flow field are averaged along one particular light path direction, and the results are interpretable only when the flow is two-dimensional. The essential requirement for three-dimensional flow visualization is illumination from a multiplicity of directions. With holography, this can be achieved in a variety of ways (Refs. 19-31).

One principal property of holography is its ability to store and reconstruct both the amplitude and phase of light wavefronts of almost arbitrary complexity. Because of this property alone, holography can be employed for intermediate storage of the wavefronts which traverse a phase object (i.e., a transparent medium with spatial variations in refractive index). Subsequent visualization can then be accomplished using the holographically reconstructed image of the phase object rather than the object itself. This approach offers numerous operational advantages since a hologram can be made of a transient event, with visualization accomplished later at leisure.

A second property of holography which opens some entirely new flow visualization possibilities is its ability to record wavefronts at different times and reconstruct them simultaneously. Since both amplitude and phase information is recorded, reconstructions of wavefronts which differ in phase, produce interferograms. One extremely important practical result of this second property of holography is that it eliminates the need for the precise optics used in interferometry. One hologram can be made to record an arbitrary wavefront traversing a flow test region before the flow is started, and a second exposure can be made with flow present. The resulting double-exposure hologram can then be used to reconstruct both wavefronts simultaneously, producing an interferogram that displays only the difference between the two wavefronts. Since only the differences are significant, any imperfection in the original wavefront recorded without flow is of no consequence.

The above property of holography, in conjunction with the exceptional coherence of laser light, also provides the prerequisites for three-dimensional flow visualization, since it makes possible wide-angle diffuse illumination of a flow region. The traversing wavefronts, though

exceedingly complex, can be holographically stored and used to produce interferograms. The fringes in such holographic interferograms are generally highly localized; consequently, they usually yield qualitative three-dimensional information when directly observed. In addition, quantitative information on the three-dimensional density distribution in the flow can be obtained provided the angle of view approaches 180° (Ref. 12). The hologram can be used to obtain a series of interferograms of the test region from a large number of directions. Each is comparable to a single interferogram obtained from Mach-Zehnder interferometer and gives the density distribution averaged over one particular light path. In the present program, a narrow field of view was used due to practical limits on window size, and consequently, it was not possible to obtain three-dimensional density distributions. It was possible, however, to locate the position of density gradients associated with shocks.

B. Interpretation of Fringes in Holographic Interferometry of Gas Flows

To utilize holographic interferometry for the study of gas density distributions, it is necessary to understand how the interference fringes observed in reconstructed images are related to the changes in density which occurred in the test region. The theory of holographic interferometry has evolved rapidly over the past few years and there is now a reasonably complete explanation for generalized displacement and deformation of diffuse reflecting surfaces. The theory has not yet, however, been extended to include phase objects such as gas density variations, which are the primary phenomena of interest in flow visualization. To provide a basis for describing the method of analysis used in this program and to explain the primary optical effects observed, the extension of present theory to include phase objects will be briefly described.

The basis for our analytical procedure can be explained by reference to Figure 34, which shows a simplified diagram of the reconstruction of a hologram of the flow test region and a recording of the reconstructed scene at the film plane of the camera lens. For simplicity, the reference beam illuminating the hologram is not shown. It is assumed that the hologram perfectly reconstructs the light field emanating from the scene. The camera is shown focused on the plane containing the point P in the test object.

If two exposures have been made, between which some relatively small changes in the scene occur, then the photograph obtained at plane F will contain an image of the scene in which interference fringes are observed, as in Figure 35. For the purpose of flow visualization we need to know how these fringes are related to changes in density of the gas in the test region. The pertinent properties of the fringes are:

1) The fringe number and spatial frequency.
2) The fringe visibility or contrast.
3) The fringe location in three-dimensional space.

1. Homologous Rays

Consider the central ray of the image-forming bundle which originates at the point S_1 on the diffuse background, Figure 36, passes through the object point P, then the center of the aperture 0_1 and terminates at the point P^1 in the film plane. On the second exposure this

same ray might be deflected due to the phase object, i.e. density variation in the test section, so that its path is as shown in Figure 36, that is S_1O_2. A general principle of holographic interferometry is that interference fringes of good visibility will be observed in the reconstructed scene only if the image-forming rays are homologous. By definition, (Ref. 32), pairs of homologous rays must originate at precisely the same point on the diffuser surface and must terminate at either the same point P^1 in the film plane or at a point close enough to P^1 so that the optical fields in the immediate vicinity of P^1 are homologous. Homologous fields are locally congruent in the sense that the apparent intensity of the two fields is virtually the same except for a small displacement.

That is, $$i_2(r') \cong i_1(r' - t'_o) \qquad \text{(III-1)}$$

where

$i_2(r')$ = Intensity in first optical field near P^1

$i_1(r')$ = Intensity in second optical field near P^1

t_o' = A small displacement

In Figure 36, the camera could be focused on any plane in the object but the ray pairs terminating at P^1 will not be homologous unless the camera is focused near P, the crossing point or point of closest approach of the original central ray $S_1 O_1 P^1$, and the apparent path of the deflected ray $S_2O_2P^1$. In this case the fringes would have the greatest visibility near P in the object.

2. Superposition of Plane Waves

In order to describe the interference phenomena in more detail, it is convenient to represent the optical fields as superposition of plane waves. The field intensity at P^1 is produced by a field amplitude U_1 (r) at P, and a second field U_2 (r), the apparent field at r on the second exposure.

$$i(r) = |U_1(r) + U_2(r)|^2 \qquad \text{(III-2)}$$

The fields can be represented by a superposition of plane waves

$$U_1(r) = \iint \Omega(k, r)\, N_1(k, r) \exp(i\, k \cdot r)\, dk \qquad \text{(III-3)}$$

$$U_2(r) = \iint \Omega(k, r)\, N_2(k, r) \exp(ik \cdot r)\, dk$$

where N_1 (k, r), N_2 (k, r) are the plane wave spectra for the initial and final field

at r and Ω (k, r) is the aperture function defined as

$$\Omega(k, r) = \begin{cases} 1 & \text{for propagation directions within the collecting aperture} \\ 0 & \text{otherwise} \end{cases}$$

and where the two angular spectra are related (Ref. 33) as follows:

$$N_2 (k) = N_1 (k) \exp [i\phi (k, r)] \tag{III-4}$$

For small numerical apertures the vector k can be represented by its central value plus a small orthogonal difference vector, (κ).

$$k = k_o + \kappa \tag{III-5}$$

The alteration of the plane wave spectrum by the phase object is predominantly described by phase change along the central ray and the rotation of the entire plane wave spectrum (Figure 37).

$$\phi (k , r) = \phi_o (k_o, r_o) + \phi_r (k_o, \Delta k_o, r_o, t) + \Delta\phi (k_o, \kappa, r_o, t) \tag{III-6}$$

where

$\phi_o (k_o, r_o)$	= phase change along the central ray thru r_o
$\phi_r (k_o, \Delta k_o, r_o, t)$	= phase change due to rotation of the apparent ray through the angles α, β
$\Delta\phi (k_o, \kappa, r_o, t)$	= phase effects which vary with direction from the central ray κ and distance from the position r_o
r	$= r_o + t$

Each of these terms has significance with respect to the observed fringe system. The first term $\phi_o (k_o, r_o)$ is the phase difference along the central ray path.

$$\phi_o (k_o, r_o) = \frac{2\pi}{\lambda} \int_\ell [n_2 (r) - n_1 (r)] \, d\ell \tag{III-7}$$

where ℓ is the path of the central ray through the phase object and n_1 and n_2 are the index of refraction spatial distributions at the time of the first and second exposures.

Using equation (III-7), quantitative three-dimensional density distributions can be determined from a series of interferograms taken from a single hologram. Methods have been devised for solving the set of simultaneous integral equations which result, and an example of the analysis of an unsymmetric flame by one such method is given in Reference 12. This technique can be used only if a field of view approaching 180° is available. For cases in which the field of view is restricted, information on the spatial location of fringes can be obtained by using perspective and depth-of-focus effects.

The second term in equation (III-6) describes the phase effects due to rotation of the plane wave spectrum and is related to index of refraction gradients transverse to the line of sight.

$$\phi_r(k_o, \Delta k_o, r_o, t) \quad = \Delta k_o \cdot t = \frac{2\pi}{\lambda} \quad (\alpha t_x + \beta t_y) \tag{III-8}$$

where α is the angle of the deflected central ray with respect to the ZY plane and β is the angle with respect to the XZ plane. This term is the major factor in determining the fringe orientation and frequency in the neighborhood of r:

α and β are calculated in the same way as in Schlieren photography, i.e.:

$$\alpha = \int_\ell \frac{\delta (n_2 - n_1)}{\delta x} d\ell \tag{III-9}$$

$$\beta = \int_\ell \frac{\delta (n_2 - n_1)}{\delta y} d\ell$$

The remaining term, $\Delta\phi$, describes the effects of the plane wave spectrum which differ for different propagation directions k and with position t in ways more complicated than the common phase change and rotation accounted for in equations III-7 and III-8. Treating these two effects separately:

$$\Delta\phi = \delta \phi_k + \delta\phi_t \tag{III-10}$$

where the magnitude of $\delta\phi_k$ depends on the complexity of the phase object and the size of the collecting aperture. If phase changes along the cone of directions within the collection aperture vary rapidly from the central value, then phase relationships will become garbled at P^1. This effect increases as the aperture is increased, which reduces the visibility of the observed fringes, the visibility decreasing as the aperture and thus the maximum value of k increases.

The magnitude of $\delta\phi_t$ depends on the variation of the plane wave spectrum with position, and the distance (t_o) of the closest point of approach of the pairs of homologous rays. Since the angular range of the planewave spectrum is controlled by the size of the aperture, the magnitude of $\delta\phi_t$ also increases with aperture. Again, as $\delta\phi_t$ increases, the visibility of the observed fringes decreases.

If the phase object is relatively simple so that $\delta\phi_k$ is small, the fringe visibility will depend only on $\delta\phi_t$ and will be approximately*

$$V = \frac{2 J_1 [\frac{4\pi}{\lambda} t_o \omega]}{(4\pi/\lambda) t_o \omega} \tag{III-11}$$

where	V	$= (i_{max.} - i_{min.})/(i_{max.} + i_{min.})$ = Visibility
	J_1	= 1st order Bessel function
	t_o	= closest point of approach of the homologous rays at P
	ω	= angular aperture of the viewing system = $\dfrac{\kappa \text{ max.}}{\lvert k_o \rvert}$

• This is a consequence of the Van Cittert-Zernike theory and is discussed in Reference 34 for deformation of real objects.

C. Localization Problems

1. Localization by Depth of Field

From the previous discussion it can be seen that the phase, ϕ, or fringe number observed at any point P^1 in the film plane depends primarily on the change in optical path along the central ray through the observing aperture which terminates at P^1. The fringes will tend to be localized near the region of intersection of the homologous rays terminating at P^1. If the density change is itself localized and produces significant angular deflections, then the fringes and the phase object will be located in the same place.

In order to locate the object in depth it should be possible to use a large aperture viewing system (i.e., with shallow depth of field) and focus on the plane which yields maximum visibility fringes. It is found that this approach generally will not work well for the following reasons:

a) Pronounced depth of focus effects will not be observed unless the angular deflections are relatively large. If angular deflections are small, as in Figure 37, homologous rays can remain close over the entire path from the source to the film plane, with no definite point of closest approach.

b) If angular deflections are large, localization by depth of field is possible. Unfortunately, the improvement in fringe visibility expected by focusing on the plane containing the region of closest approach (P_1P_2, Figure 37) is more than offset by the reduction in visibility due to use of the large aperture required to achieve a shallow depth of field.

2. Localization of Fringes by Triangulation

An alternative to the use of a shallow depth of field viewing system for localization is to view the scene from two or more different directions using an optical system of small enough aperture to show good visibility fringes and at the same time having the coordinate lines of a grid system placed elsewhere in the scene. The spatial location of observed structures can then be obtained by measuring their apparent displacement with respect to the grid when observed from two directions. This technique is used in the present program and described

in detail in Appendix IV. Again, the fringes will tend to be localized near the intersection of homologous rays. For isolated density changes, therefore, the fringes will be located in the region of density change. This is the case in the holographic interferogram shown in Figure 35, for example.

For the case of a general density change distributed through space, fringes can exist anywhere but their location in space is not simply related to the position of the density changes which produce them. In this latter case it is still frequently possible to locate by triangulation regions in which abrupt changes in density occur.

3. Localization of Regions of Abrupt Density Change by Triangulation

Figure 38 illustrates the recording of a scene with the camera at two different locations. The line σ represents a simplified shock surface marking a density change, $n_o \rightarrow n_1$. With the camera in position A, by the principles previously discussed, we should expect an abrupt change in fringe frequency from one side to the other of point $P_{A'}$. Similarly, with the camera in position B an abrupt change in fringe frequency occurs at $P_{B'}$. Thus, though the fringes themselves may not be localized in the shock plane at the tip of the blade, the observed discontinuity in fringe frequency is determined by triangulation to be at that location.

This statement is made assuming that the region in which the density or index of refraction change has occurred is confined to a relatively narrow sheet of space as seen from the viewing direction. This holds, for example, in the case of shock waves which have traveled only a small distance between exposures and can be viewed separately; i.e., without the line of sight passing through more than a single strong shock front. If these conditions are met, then all sharp discontinuities in density can be localized. This has been the basis for the analysis discussed in Appendix IV.

4. Summary of Optical Effects

1. The phase change at any point P^1 in the film plane is determined by the change in optical path along the central ray terminating at that point (Eq. III-7).

2. The spatial fringe frequency in the neighborhood of P^1 depends on the angular deflection of the central ray, which in turn is due to the gradient of the index of refraction transverse to the central ray (Eq. III-9).

3. The visibility of the observed fringes is best when the camera is focused near the point of intersection of homologous rays which may be located where the density gradient exists in simple objects. However, it can, in general, be located anywhere in space (Eq. III-11).

4. The visibility of the fringes decreases with increasing aperture of the viewing system (Eq. III-11). This effect is enhanced if the phase object is complex.

APPENDIX IV

DETERMINATION OF THE VIEWING PARAMETERS AND THE DERIVATION OF THE TRIANGULATION EQUATIONS

A. Methods for Determining Viewing Parameters (θ_{xy}, θ_{yz}, and C)

Photographs taken of a hologram correspond to photos taken directly of the fan rig from positions approximated in Figure 39. The angle at which the origin is viewed in a particular photo was determined, θ_{yz} in the Y-Z and θ_{xy} in the X-Y plane independently, from the relative positions of the window grid with respect to the hub grid. This was accomplished by carefully measuring the position on the hub grid upon which the origin of the window grid had been superimposed, as seen in the photo in question. The angle between the Y-axis and the line connecting the point on the hub with the origin on the window was then determined by plotting these points on scale drawings of the fan rig. Scale drawings of the fan rig in the X-Y plane, Figure 40, and the Y-Z plane, Figure 21, were used to obtain the angles θ_{xy} and θ_{yz}, respectively for five sets of photographs taken of each hologram at different viewing angles.

Also determined for each set of photographs was the distance, C, from the camera lens to the origin of the coordinate system, i.e., the window. By measuring the relative sizes of the two grid systems in the photographic image and using the known distance from the window to the hub, the distance C was calculated. This avoids the necessity of correcting for the wavelength difference between the ruby and HeNe lasers. Also, the distance from the holographic plate to the rig window was not accurately measured before the holocamera was removed from the test stand. The distance, d, between the grids was accurately known in both the X-Y and the Y-Z planes and, therefore, the distance between the camera and the window was calculated from the ratio (see Figure 39):

$$\frac{b_z}{a_z} = \frac{C_{yz}}{(d_{yz} + C_{yz})}$$

where:

b_z is the distance in the direction of the Z-axis between two points associated with two lines of sight on the viewing window.

a_z is the distance in the direction of the Z-axis between two points (corresponding to the two lines of sight) on the hub.

C_{yz} is the distance, in the YZ plane, between the point of observation and the rig window.

d_{yz} is the distance, in the YZ plane, between the window and the hub.

Therefore, for the component of C in the Y-Z plane:

$$C_{yz} = \frac{d_{yz}\, b_z}{(a_z - b_z)}$$

This measurement should be obtained for the Y-Z plane first, because no correction for window curvature is made in this plane. The total value of C is then obtained from the relationship:

$$C = C_{yz}/\cos(90° - \theta_{xy}) = \frac{C_{yz}}{\sin\theta_{xy}}$$

By the same reasoning: $C = \dfrac{C_{xy}}{\sin\theta_{yz}}$

B. Determination of the Common Point Coordinate Positions

The procedure for locating common points in two different photographs involves locating discontinuities in the fringe frequency, as discussed in Appendix III, Section C.3. A point on a line of fringe frequency discontinuity identified in any one photograph can then be located in any other photograph in which the fringe frequency discontinuity can be seen, knowing the relative change in viewing angles between the two photographs. Once the point has been located in both photographs, the (X_0, Z_0) coordinate position on the window grid system can be measured in each photograph. This procedure is demonstrated in Appendix V.

C. Derivation of the Triangulation Equations

Refer to Figure 41 for the following derivation. A general equation for the projection of a straight line on the Y-Z plane is:

$$y = m\,(Z - Z_0) \qquad \text{IV-1}$$

where m is the slope of the line and Z_0 is the Z axis intercept of the line. The slope m, can be written

$$m = \tan\theta$$

where θ is the angle between the line of sight and the Z-axis. As can be seen in Figure 41, $\theta = \Phi_{yz} + \theta_{yz}$, where Φ_{yz} is the angle between the line of sight passing through the feature of interest and the line of sight passing through the origin. For a small Φ_{yz} and for values of θ_{yz} close to 90°, Φ_{yz} can be determined by the expression

$$\Phi_{yz} = \tan^{-1}(Z_0/C_{yz})$$

where Z_0 is the apparent position of the point of interest, as seen in the photo, measured along the z axis. It should also be clear that Z_0 is the value of z axis intercept of the line of sight. Therefore, the equation corresponding to the projection on the Y-Z plane of the line of sight passing through a point of interest in the flow field can be expressed as in equation 1, p. 14, by substituting the values of Φ_{yz} and θ_{yz} into equation (IV-1).

Similarly, the equation for a projection of a line in the X-Y plane is

$$y = \tan\theta' (X - X_0) \tag{IV-2}$$

where X_0 is the X-axis intercept of the line of sight. However, the value of θ' must be determined by using an extra step which corrects for the curvature of the window in the X-Y plane.

The window is a negative lens, in the X-Y plane, with a focal length f given by the equation (Ref. 35).

$$1/f = (n-1)(1/R_1 - 1/R_2)$$

where n = index of refraction of the window material; R_1, R_2 = radii of curvature of the two surfaces of the window. A value of n = 1.57 was used for the index of refraction of polycarbonate plastic, and $R_1 = \infty$, $R_2 = 16.5$ inches were used as the values for the curvature of the window surfaces. These numbers give a value of f = -29 inches.

A point located a distance s_1 from a lens with a focal length f will be imaged at a point located a distance s_2 from the lens, Figure 41. The equation which describes this relationship can be written (Ref. 35).

$$\frac{1}{s_1} + \frac{1}{s_2} = \frac{1}{f} \; .$$

This equation can be used to correct the angular change produced by the window, in the line of sight passing through a point located at s_1 in the flow field, (Fig. 41). Clearly

$$\tan\psi_1 = \frac{X_0}{s_1}$$

$$\tan\psi_2 = \frac{X_0}{s_2}$$

where ψ_1, is the angle between the Y-axis and the line of sight passing through s_1, and ψ_2 is the angle between the Y-axis and the apparent line of sight, as viewed from outside the window, which passes through the image at s_2. Substituting for s_1 and s_2, where s_2 is considered negative for a negative lens:

$$\frac{1}{f} = \frac{1}{X_0}(\tan\psi_1 - \tan\psi_2) \tag{IV-3}$$

therefore:

$$\psi_1 = \tan^{-1} [(\frac{X_o}{f}) + \tan \psi_2]$$

It can be seen that:

$$\psi_1 = 90° - \theta'$$

$$\psi_2 = 90° \quad (\theta_{xy} + \phi) = 90° - [\theta_{xy} + \tan^{-1} (\frac{X_o}{C_{xy}})]$$

And therefore:

$$\tan \psi_1 = \cot (90° - \psi_1) = \cot (\theta')$$

$$\tan \psi_2 = \cot (90° - \psi_2) = \cot [\theta_{xy} + \tan^{-1} (\frac{X_o}{C_{xy}})]$$

Substituting for ψ_1 and ψ_2 in equation (IV-3), θ' is given by:

$$\theta' = \cot^{-1} [(\frac{X_o}{f}) + \cot [\theta_{xy} + \tan^{-1} (\frac{X_o}{C_{xy}})]$$

Using the above equation to substitute for θ' in equation (IV-2) will result in equation 2, p. 14. Equations 1 and 2, p. 14, represent two planes whose intercept defines a line of sight passing through a point of interest in the flow field. Examples of the use of equations 1 and 2 to determine the locations of points within a flow field are given in Appendix V.

APPENDIX V

SAMPLE CALCULATIONS AND ERROR ANALYSIS

A. Sample Calculations

The following examples demonstrate the use of the procedures described in Appendix IV to determine the location of points on a shock wave surface. Two photographs from each of two holograms, one at 70% design speed and one at 100% design speed, were chosen as examples because they demonstrate the use of the triangulation method for both types of fringe systems encountered in the holographic images.

Figure 42 includes two photos taken of a hologram obtained at a 70% speed line from two viewing directions. The values of the viewing parameters for view A were:

$\theta_{xy} = 93.3°$

$\theta_{yz} = 94.8°$

C = 13.9 inches

and for view B the values were:

$\theta_{xy} = 100.9°$

$\theta_{yz} = 95.0°$

C = 15.6 inches

Lines forming the boundary between regions of the fringe system with differing fringe spacing have been identified by dotted lines.

The task of identifying these reference lines in each photograph shown was easily done because the fringe system has nearly the same appearance in both photographs. However, if a question arises concerning the identification of a reference line, it can be resolved by g ·ng back to the hologram and viewing the image directly, and changing the viewing position in a manner similar to that done for the photos. The gradual change in appearance and position of a reference line can then be directly observed, clearing up questions concerning the identification of a reference line on the photograph.

The task of identifying identical points on a reference line as seen from two different viewing angles was further simplified by changing the viewing angles only along lines parallel to either the X or Z axis. It can be seen that these two photos were both taken in almost the identical XY plane since the θ_{yz} values are nearly the same. It can, therefore, be assumed that the points which lie on the apparent edge of the mid-shock surface in view A, Figure 42a, will also appear to lie under a grid line parallel to the X-axis in view B, Figure 42b.

The values in inches of X_o and Z_o corresponding to the points marked by an ⓧ in photographs A and B (Figure 42) are:

$$A: \quad (X_o, Z_o) = (0.19, -1.0)$$

$$B: \quad (X_o, Z_o) = (0.11, -1.0)$$

When these values were inserted into equations 1 and 2, page 14, and the equations solved for (X, Y, Z) the following values were obtained:

$$(X, Y, Z) = (0.25, -0.71, -0.99)$$

Similarly for the point indicated by an 0 in the photographs;

$$A: \quad (X_o, Z_o) = (-0.088, -1.0)$$

$$B: \quad (X_o, Z_o) = (-0.389, -1.0)$$

and, therefore:

$$(X, Y, Z) = (0.05, -2.86, -0.97)$$

Points ⓧ and 0 of Figure 42 are indicated in Figure 31a and c respectively. The procedure used to plot these points was given on page 15.

The appearance of the fringes in the hologram shown in Figure 43, hologram 21, is different than that of the previous example and the identification of the common points in the two photographs is more difficult. Because a fringe system such as that seen in this hologram cannot be identified, each observable fringe must be used as a reference line. One such fringe is identified in the two photographs in Figure 43 by a dotted line. As stated previously, problems in identifying the same feature from two viewing angles can usually be resolved by viewing the hologram directly.

The values of the viewing parameters for photo A were:

$$\theta_{xy} = 87.5°$$

$$\theta_{yz} = 90.35°$$

$$C = 13.7 \text{ inches}$$

and for photo B the values were:

$$\theta_{xy} = 99.4°$$

$$\theta_{yz} = 90.5°$$

$$C = 17.2 \text{ inches}$$

A point on the dotted reference line has been identified by an ⓧ. After measuring the values of X_0 and Z_0 for the point in each photograph:

$$A: \quad (X_0, Z_0) = (1.216, 0.)$$

$$B: \quad (X_0, Z_0) = (0.582, 0.0)$$

the following values of (X, Y, Z) were determined:

$$(X, Y, Z) = (1.63, -4.74, 0.03)$$

This point has also been plotted in Figure 27c and identified by an ⓧ.

B. Error Analysis

The accuracy with which the position of a point on a shock wave can be determined is dependent primarily on three factors.

1. Accuracy of the triangulation method.

   The accuracy of the triangulation method was tested experimentally by checking the accuracy with which the position, within the flow passage of the fan rig, of a target could be determined using this method. A small cardboard strip with 2 small dots placed on the surface was used as the target for the measurements. The target was placed approximately three inches inside the window of the fan rig. Photographs of the target, taken through the window, were obtained from three viewing angles. The apparent positions of the dots were carefully measured in each of the photos and this information was used to solve equations 1 and 2 (Page 14) for (X, Y, Z). The results agreed with the direct measurements of the dot positions to within 1/20 inch for the X, Z coordinates and to within 1/10 inch for the Y coordinate.

2. An uncertainty in relating the position of the fringe system to the position of the fan blades was introduced because of motion occurring between laser pulses.

   The distance the fan blades move between laser pulses places an upper limit on this uncertainty. Distance varied from approximately 1/4 inch to 1/3 inch as the line was increased from 70% to 100% of the design speed. The uncertainty in blade position contributes primarily to an error in the determination of the X, Y, Z coordinates. A shorter pulse separation is an obvious means to reduce the error.

3. Errors involved in locating a point on a shock wave from two different viewing angles.

   This error varies greatly from hologram to hologram and even between points on a single shock wave.

   The conditions under which the location of abrupt density changes can be accurately determined has been qualitatively stated in Appendix III and in the case of very

complicated flow fields, such as those considered herein, these conditions are probably never ideally met. However, it is possible in many instances to determine the extent to which the conditions set forth in Appendix III are met. For example, when a point on a shock wave can be seen from three or more viewing directions the determination of the position of the point on the shock front can be carried out using three or more sets of data. If the coordinates of the point determined from each set of viewing angles agree within the limits of error established by error factors #1 and #2, the conditions stated in Appendix III were met to a considerable extent. However, if a complex index of refraction change occurring in the flow field invalidates the assumption, the reference line will shift in space as the viewing angle is changed, and the results from each set of data will probably be contradictory. It was the experience in this program that, for most cases in which this check could be carried out, the results obtained from differing sets of viewing angles agreed very closely. There were cases which did not cross-check. However, the cause could generally be traced to the fact that the line of sight passing through the shock whose position was being determined was also passing through another shock located between the point of interest and the window.

The variation in X, Y, Z values obtained using more than one set of viewing angles is probably the best available means of judging the confidence one can place in the results.

Several values of the coordinates (X, Y, Z) were computed for 4 points in the hologram shown in Figure 42 using as many sets of data as were permitted by viewing conditions. The average value obtained for the coordinates of each point was determined and the difference between each coordinate and the appropriate average value was calculated. The standard deviations determined from this process, using every available set of data (11 cases) were;

$$\sigma_x = 0.09 \text{ inches}$$

$$\sigma_y = 0.69 \text{ inches}$$

$$\sigma_z = 0.015 \text{ inches}$$

If the data were restricted to those views obtained from X-Y plane pairs, the values of the standard deviations would be much smaller.

$$\sigma_x = 0.016 \text{ inches}$$

$$\sigma_y = 0.26 \text{ inches}$$

$$\sigma_z = 0.014 \text{ inches}$$

These results were more consistent since the angle of the shock waves permits greater accuracy in determining the position of common points in the photographs paired in the X-Y plane. In many of the photographs from which the above results were obtained, the visibility of the fringe system in the regions in which the measurements were ob-

tained was rather poor. Generally there is only one pair of views from which a clear view of a particular region of a fringe system can be obtained. This is why usually only one set of data was used in determining each point used on a shock position. The accuracy of these results may have been better than the standard deviation would indicate, because the data used to obtain the standard deviations included many points whose positions could not be clearly viewed.

APPENDIX VI

PLANE RECONSTRUCTION OF SHOCK WAVES FROM THE HOLOGRAPHIC ANALYSIS

In Appendix IV, the method by which points on fringes seen on the holograms were located in space was described. The aerodynamic interpretations discussed in pages 15–22 are, for the most part, limited to shock lines connecting points located in space at approximately the same radial position. These shock lines could then be drawn with respect to the known blade shape and orientation in each radial plane.

In general, however, it is preferable to locate all such fringe points, and then mathematically determine,if possible, a surface in space on which all points lie. In this way, the intersection of the shock surface and any blade plane could, in principle, be constructed. In the following analysis, the derivation is given for the necessary equations to define the line of intersection of a plane, which approximates the three-dimensional shock, and a plane on which the blade is defined.

In Figure 44a, the tangent plane on which the blade definition is given at a representative radius $r = r_0$ is shown. The value R is the radius from the compressor axis to the window at the axial location of the origin of the (X,Y,Z) coordinate system (Figure 44a, b,c). This (X, Y, Z) coordinate system was defined in Appendix IV. If a tangent plane parallel to the X-axis is chosen (whose normal is a radial line at $\theta = 0$, $r = r_0$) it can be seen (Figure 44a) that the difference between the X-displacement, $r_0 \sin \theta_0$, on that plane and the circumferential distance $r_0 \theta_0$ is small for small values of θ (less than 10°). In the present application θ_0 is small enough that the tangent plane closely approximates the "unrolled" cylinder with radius r_0.

The blade plane, with its normal in the radial direction at $\theta = 0$, $r = r_0$, can be described according to the equation

$$\left(-\frac{\cos \epsilon_T}{R - r_0}\right) Y + \left(\frac{\sin \epsilon_T}{R - r_0}\right) Z = 1 \qquad \text{(VI-1)}$$

where $\epsilon_T = 19.3°$, the angle between the O.D. casing at the window location and the compressor axis (Fig. 44).

The general shock surface is described by a plane of the form

$$aX + bY + cZ = 1 \qquad \text{(VI-2)}$$

The constants a, b, and c are found by locating three sets of (X,Y,Z) coordinates in space, and using these in equation (VI-2) to solve the three resulting linear equations simultaneously. The (X,Y,Z) coordinates are located by the method described in Appendix IV.

The line of intersection of the planes described by equations (VI-1) and (VI-2) can be found by taking the vector cross-product between the normals of these planes. The line of intersection, therefore, may be written.

$$X = \frac{(b \sin \epsilon_T + c \cos \epsilon_T)\, Y - (\sin \epsilon_T - c\,(R\text{-}r_o))}{-\, a \sin \epsilon_T} = \frac{(b \sin \epsilon_T + c \cos \epsilon_T)\, Z - (b(R\text{-}r_o) + \cos \epsilon_T)}{-\, a \cos \epsilon_T}$$

(VI-3a)

$$\text{Or,} \quad Y = \frac{(-\, a \sin \epsilon_T)\, X + (\sin \epsilon_T - c\,(R\text{-}r_o))}{b \sin \epsilon_T + c \cos \epsilon_T} \; ; Z = \frac{(-\, a \cos \epsilon_T)\, X + (b\,(R\text{-}r_o) + \cos \epsilon_T)}{b \sin \epsilon_T + c \cos \epsilon_T}$$

(VI-3b)

The axial coordinate $\zeta = Z \cos \epsilon_T + Y \sin \epsilon_T$, Figure 44b, is defined in a direction which lies parallel to the tangent plane at $r = r_o$ (and therefore parallel to the compressor axis of rotation). With the use of equation (VI-3b),

$$\zeta = \frac{1}{b \cos \epsilon_T + c \sin \epsilon_T} \left\{ -\, a X + [1 - (R\text{-}r_o)\,(c \sin \epsilon_T - b \cos \epsilon_T)] \right\} \qquad \text{(VI-4)}$$

This represents a straight line in the tangent plane at any radius $r = r_o$, with X measured as the distance in the tangential direction (to within the approximation $r_o \sin \theta_o \cong r_o\, \theta_o$) and ζ measured as the axial location along the compressor axis (with $\zeta = 0$ at the origin of the X, Y, Z system).

With the use of equation (VI-4), and having the constants a, b, c determined as previously described, the shock line intersection for any value r_o can be drawn. With the blade shape and orientation also known, the relative positions of the shock and blade can be shown. For hologram 13, some representative results are shown in Figure 32, and compared to the "point reconstruction" described in Appendix IV and used for all successful holograms. From visual observation of the holograms, it was concluded that only hologram 13 showed shock surfaces which appeared nearly flat enough to approximate as planes.

REFERENCES

1. Alwang, W., et. al., *Optical Techniques For Flow Visualization and Flow Field Measurements in Aircraft Turbomachinery* Item 2, Final Report (PWA 4276) Prepared Under Contract N0001969-69-C-0322 for Naval Air Systems Command, Dept. of the Navy, August 1971.

2. Morris A.L., Halle, J.E., and Kennedy, E.E., *High-Loading, 1800 ft/sec Tip Speed, Transonic Compressor Fan Stage-1. Aerodynamic and Mechanical Design,* Contract NAS3-13493, NASA, CR-120907, 1972.

3. Morris, A.L. and Sulam, D.H., *High Loading, 1800 ft/sec Tip Speed, Transonic Compressor Fan Stage - Final Report,* Contract NAS3-13493, NASA CR-120991, 1973.

4. Tanner, L.H., *The Scope and Limitations of Three-Dimensional Holography of Phase Objects,* J. Sci. Inst., v. 44 (1967) p. 1011.

5. Cain, D., Sammartino, E., Cavanaugh, L.A., and Alwang, W.G., *Holographic Flow and Sound Visualization,* Instrumentation in the Aerospace Industry, v. 16, Instrument Society of America, (1970), p. 111-125.

6. Danue, V., Sacchi, C.A., and Svelto, O., *Single Transverse and Longitudinal Mode Q-Switched Ruby Laser,* IEEE J. of Quant. Elect., v. QE-2 no. 8, August 1966, p. 290-293.

7. Bradley, D.J., Engwell, M.S., and McCullough, A.W., *Direct Spectroscopic Detection of Ruby Laser Giant Pulse Off-Axial Mode Structure,* Appl. Phys. Letters, v. 9 no. 4, August 15, 1966, p. 150-152.

8. Hercher, M., *Single Mode Operation of a Q-Switched Ruby Laser,* Appl. Phys. Letters, v. 7 no. 2, July 15, 1965, p. 39-41.

9. Leonard, C.D. & Smirl, A.L., *Holographic Recording with Limited Laser Light, Applied Optics,* Vol. 10, No. 3, March 1971, pp. 625-631.

10. Biedermann, K., *Attempts to Increase the Holographic Exposure Index of Photographic Materials,* Applied Optics, Vol. 10, No. 3, March 1971, pp. 584-595.

11. Cambel, A. B., Jennings, B.H., *Gas Dynamics,* Dover Publications, New York, 1958, p. 299-301.

12. Alwang, W., et. al., *Optical Techniques For Flow Visualization and Flow Field Measurements In Aircraft Turbomachinery,* Item 1 Final Report (PWA 3942) Prepared Under Contract N00019-69-C-0322 for Naval Air Systems Command, Dept. of the Navy, June 1970, pp. 12-23.

REFERENCES (Cont'd)

13. Kantrowitz, A. and Donaldson, C. du P., *Preliminary Investigation of Supersonic Diffusers,* NACA ACR L5D20, 1945.

14. Kantrowitz, A., *The Supersonic Axial-Flow Compressor,* NACA Report 974, 1946.

15. Goldberg, T. J. and Sterrett, J.R., *Use of Shadowgraph Technique in the Analysis of the Performance of Two Supersonic Axial-Flow Compressor Rotors Operating Over a Mean Radius Relative Mach Number Range of 0.85 to 1.7,* NACA RM L56A05, 1958.

16. Gabor, D., *New Microscopic Principle,* Nature, v. 161 (1948), p. 777.

17. Leith, E.N., and Upatnieks, J., *Wavefront Reconstruction with Diffused Illumination and Three-Dimensional Objects,* J. Opt. Soc. Am., v. 54 (1964), p. 1295.

18. Stroke, F.W., and Falconer, D.G., *Attainment of High Resolution in Wavefront-Reconstruction Imaging,* Appl. Phys. Letters, v. 13 (1964), p. 306.

19. Horman, M.H., *An Application of Wavefront Reconstruction to Interferometry,* Appl. Optics, v. 4 (1965), p. 333.

20. Brooks, R.E., Heflinger, L.O., and Wuerker, R.F., *Interferometry with a Holographically Reconstructed Comparison Beam,* Appl. Phys. Letters, v. 7 (1965), p. 248.

21. Heflinger, L.O., Wuerker, R.F., and Brooks, R.E., *Holographic Interferometry,* J. Appl. Phys., v. 37 (1966), p. 642.

22. Chau, H.H.M., and Mullaney, G.J. *Holographic Moire Patterns; their Application to Flow Visualization in Aerodynamics,* Appl. Optics., v. 6 (1967), p. 1428.

23. Siebert, L.D., and Geister, D.E., *Pulsed Holographic Interferometry vs. Schlieren Photography,* AIAA Journal, v. 6 (1968), p. 2194.

24. Witte, A. B., and Wuerker, R.F., *Laser Holographic Interferometry Study of High Speed Flow Fields,* AIAA 4th Aerodynamic Testing Conference Paper No. 69-347 (1969).

25. Tanner, L.H., *Some Applications of Holography in Fluid Mechanics,* J. Sci. Inst., v. 43 (1966), p. 81.

26. Holds, J.H., and Fush, A.E., *A Refined Analysis of a Holographic Interferogram,* J. Appl. Phys., v. 38 (1967), p. 5408.

27. Tanner, L.H., *The Scope and Limitations of Three-Dimensional Holography of Phase Objects,* J. Sci. Inst., v. 44 (1967), p. 1011.

28. Philbert, M., and Surget, J., *Application of the Holographic Interferometer in a Wind Tunnel,* La Recherche Aerospatiale, Jan-Feb 1968, p. 55.

REFERENCES (Cont'd)

29. Smigielski, P., and Royer, H., *Applications of Holography in Aerodynamics,* L'Onde Electrique, v. 48 (1968), p. 223.

30. Mallick. S., and Roblin, M. L., *Shearing Interferometry by Wavefront Reconstruction Using a Single Exposure,* Appl. Phys. Letters, v. 14 (1969), p. 61.

31. Cain, D., et. al. *Holographic Flow and Sound Visualization,* Instrumentation in the Aerospace Industry, v. 16, Instrument Society of America, Pittsburgh (1970).

32. Walles, S., *On The Concept of Homologous Rays in Holographic Interferometry Of Diffusely Reflecting Surfaces,* Optica Acta, Vol. 17, No. 12, 1970, p. 899-913.

33. Stetson, K.A., *A Rigorous Treatment of the Fringes of Hologram Interferometry,* Optik, 29, No. 4, 1969, p. 386-400.

34. Tsuruta, T., et. al., *Formation & Localization of Holographically Produced Interference Fringes,* Optica Acta, 16, No. 6, 1969, pp. 723-733.

35. Sommerfeld, A.. *Optics,* Academic Press Inc., New York (1954), p. 343.

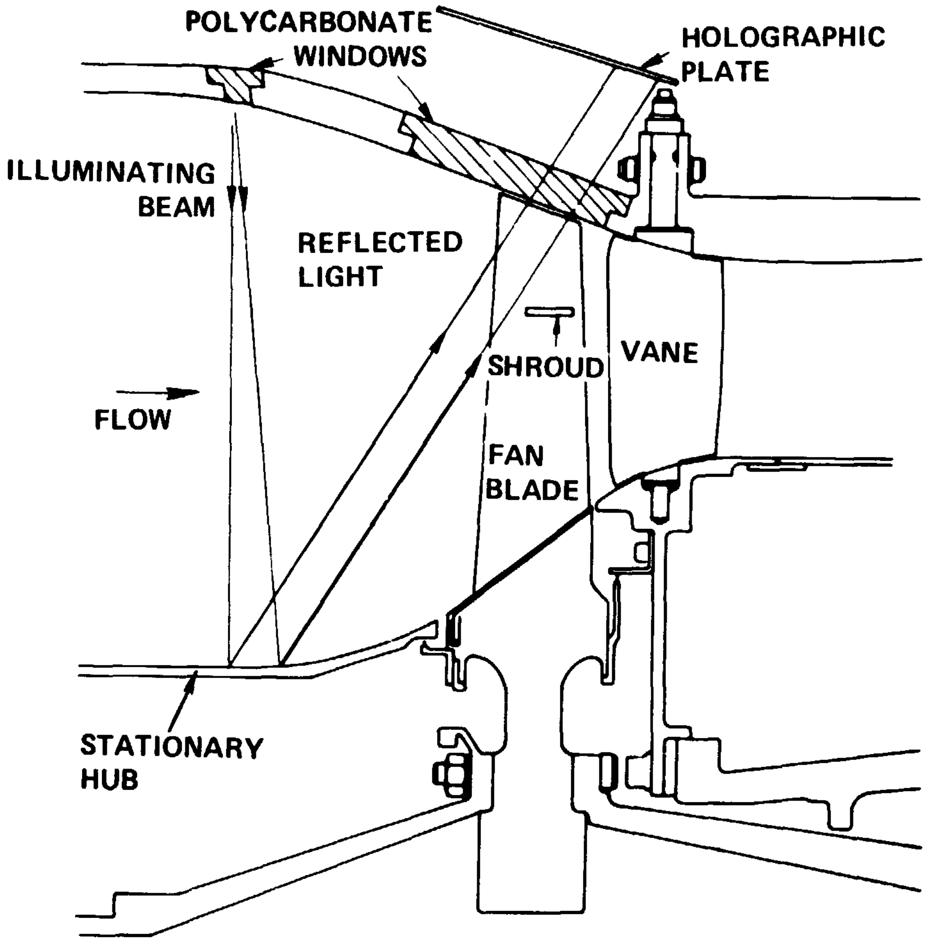

Figure 1 Optical Paths in the Transonic Fan Rig

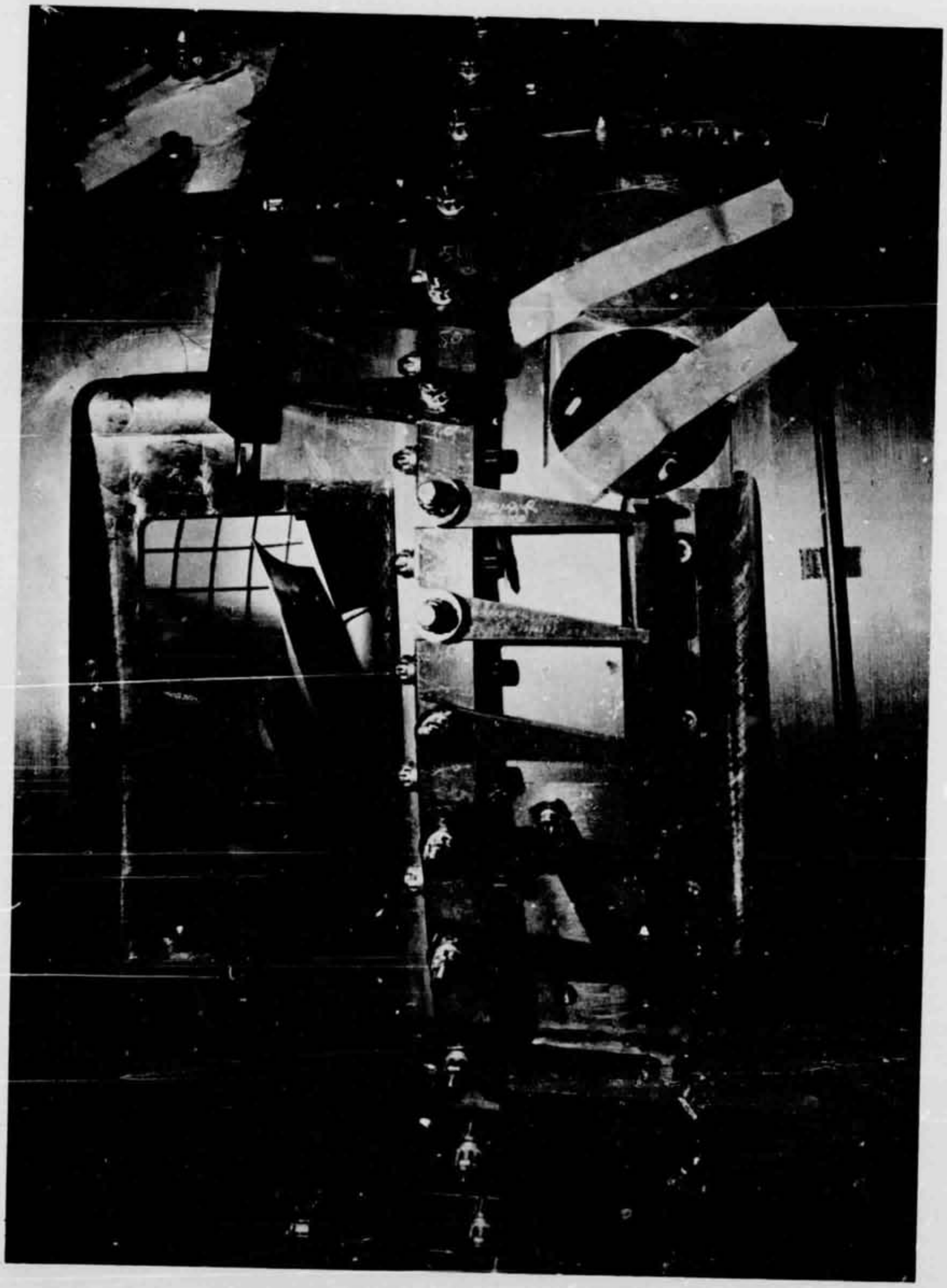

Figure 2 Photograph of Fan Rig Exterior Without Viewing Window

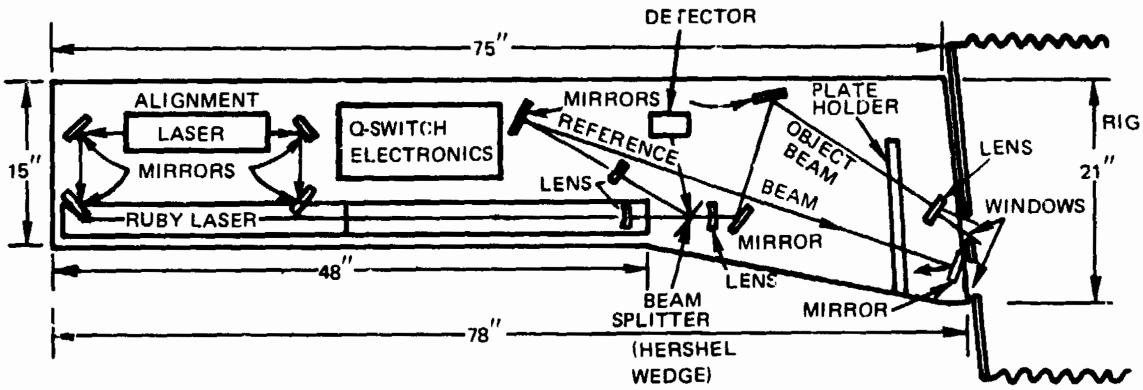

Figure 3 Optical Configuration of Holocamera (Fresnel Configuration)

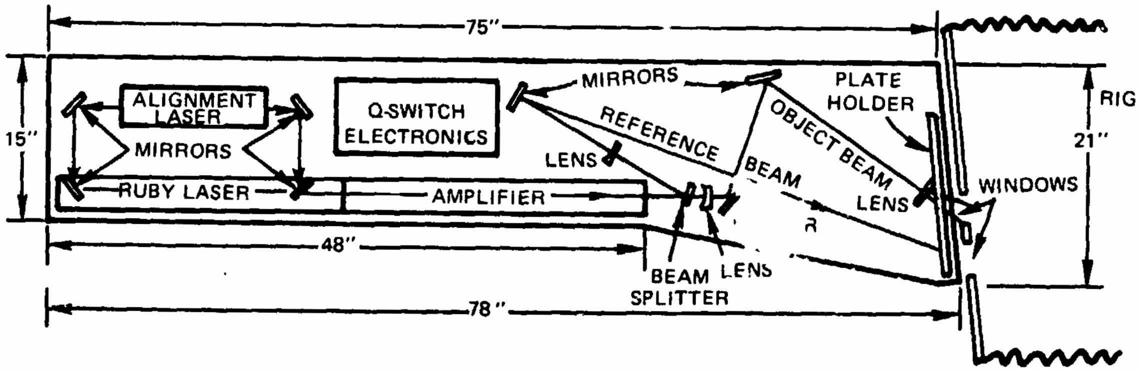

Figure 4 Optical Configuration of Holocamera (Bragg Configuration)

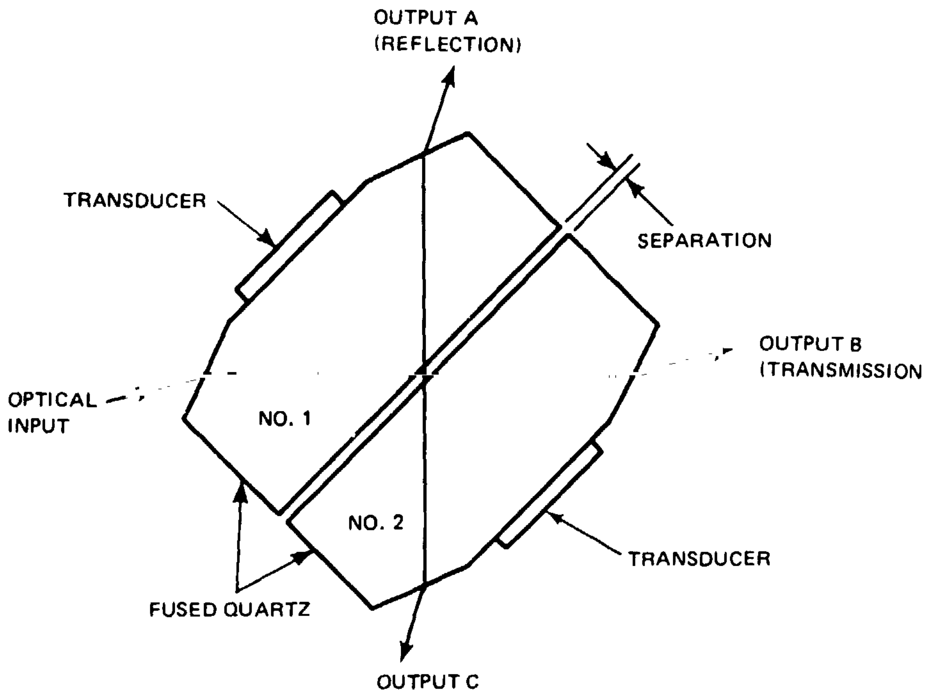

Figure 5 FTIR Q-Switch Mechanism

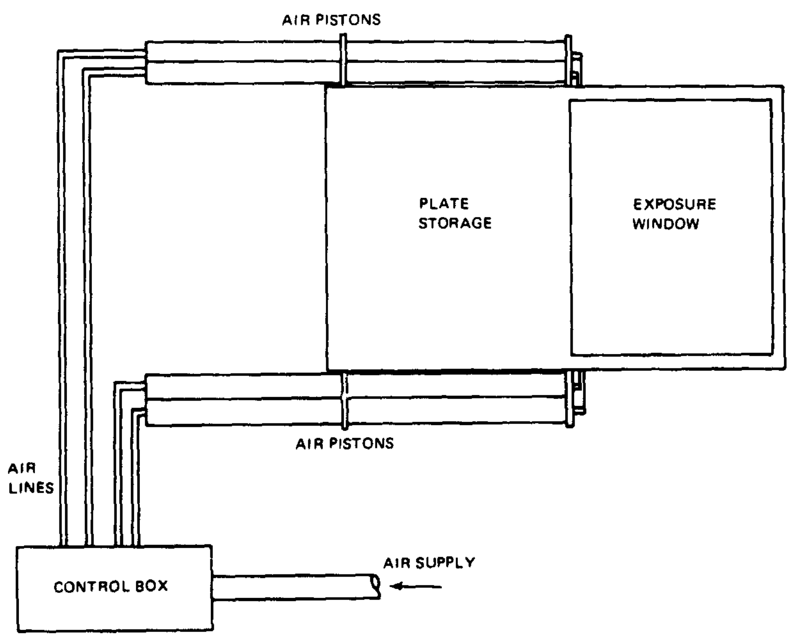

Figure 6 Schematic of Holographic Plate Transport System

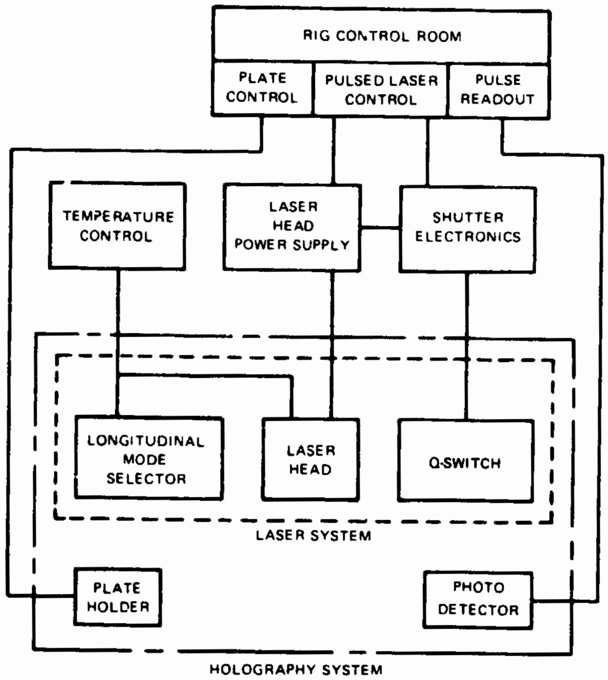

Figure 7 Block Diagram of Holography System

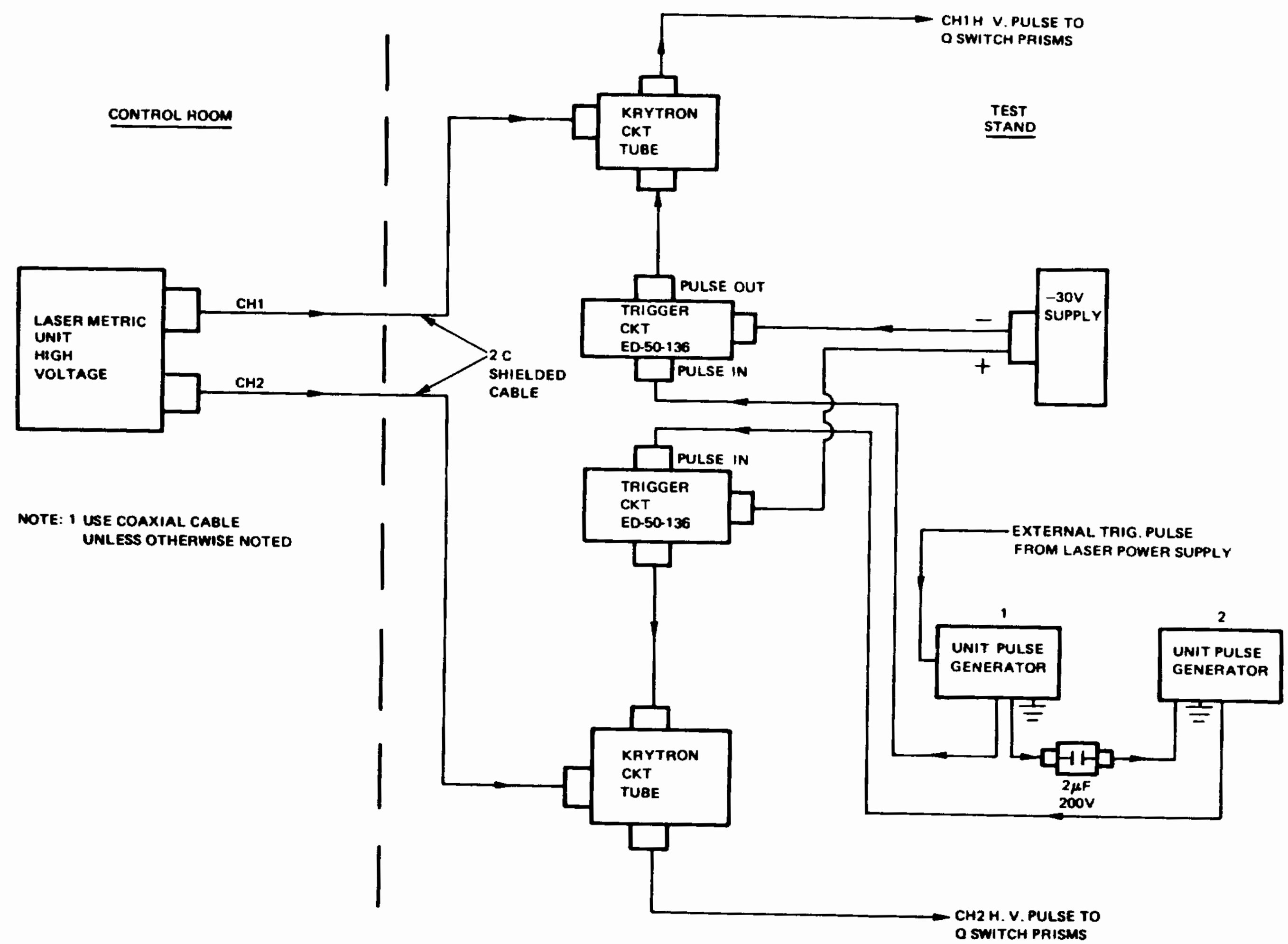

Figure 8 Wiring Diagram for the FTIR Q-Switch Electronics

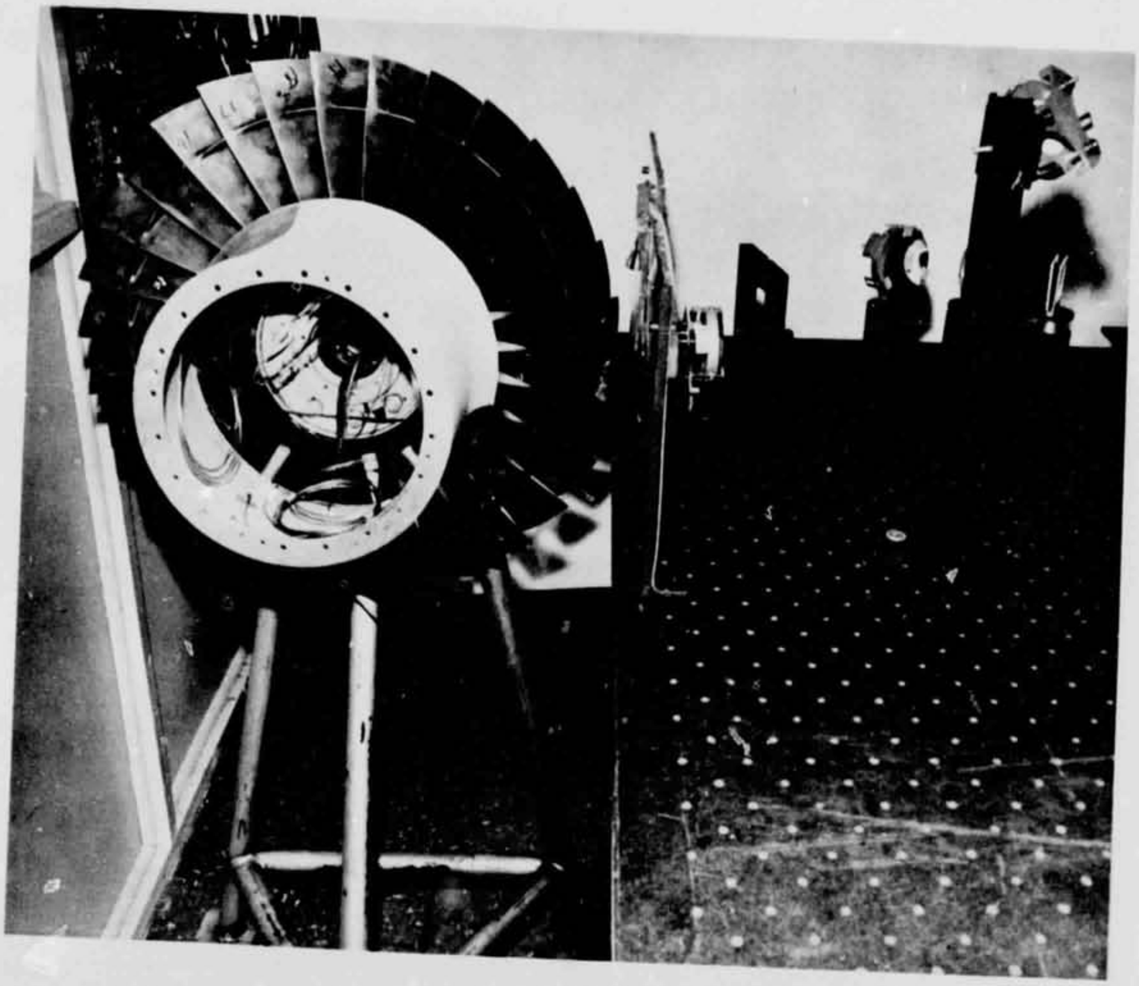

Figure 9 Rotor Assembly Used for Bench Tests

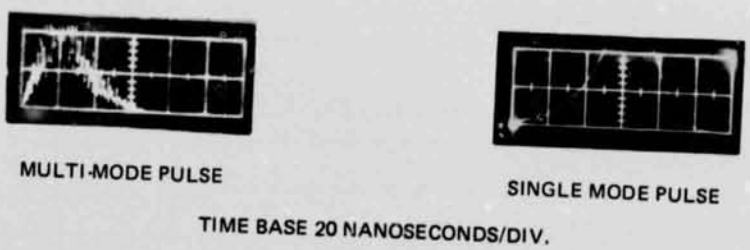

Figure 10 Single Pulse Shapes from Q-Switched Pulse Lasers

HUB IN FOCAL PLANE

SHROUD IN FOCAL PLANE

LEADING EDGE, NEAR TIP, IN FOCAL PLANE

HIGH F-NUMBER VIEW

Figure 11 Hologram Views of Bench Model (Recorded at Four Focal Planes Within the Holographic Image)

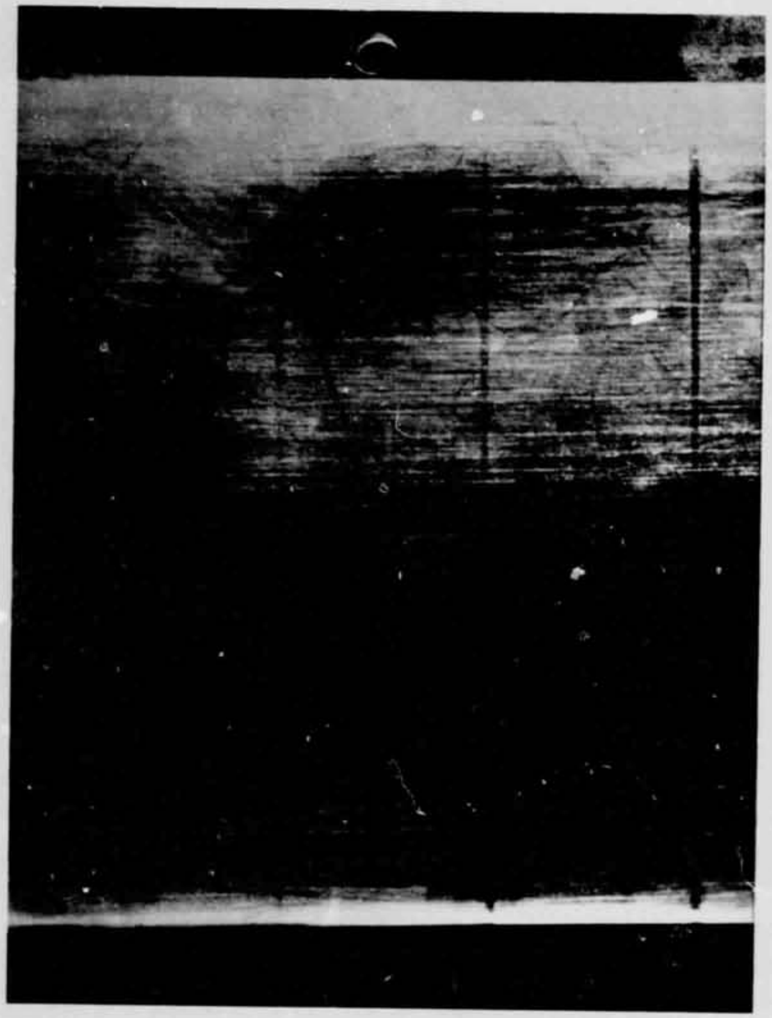

Figure 12 Window Damage

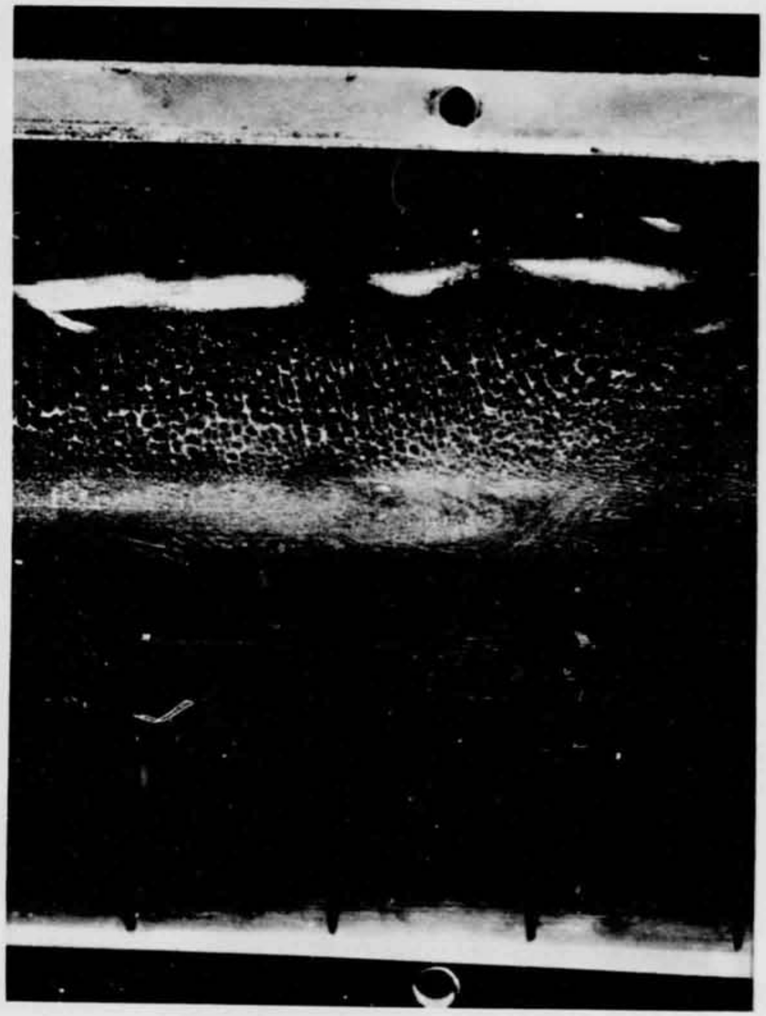

Figure 13 Window Damage

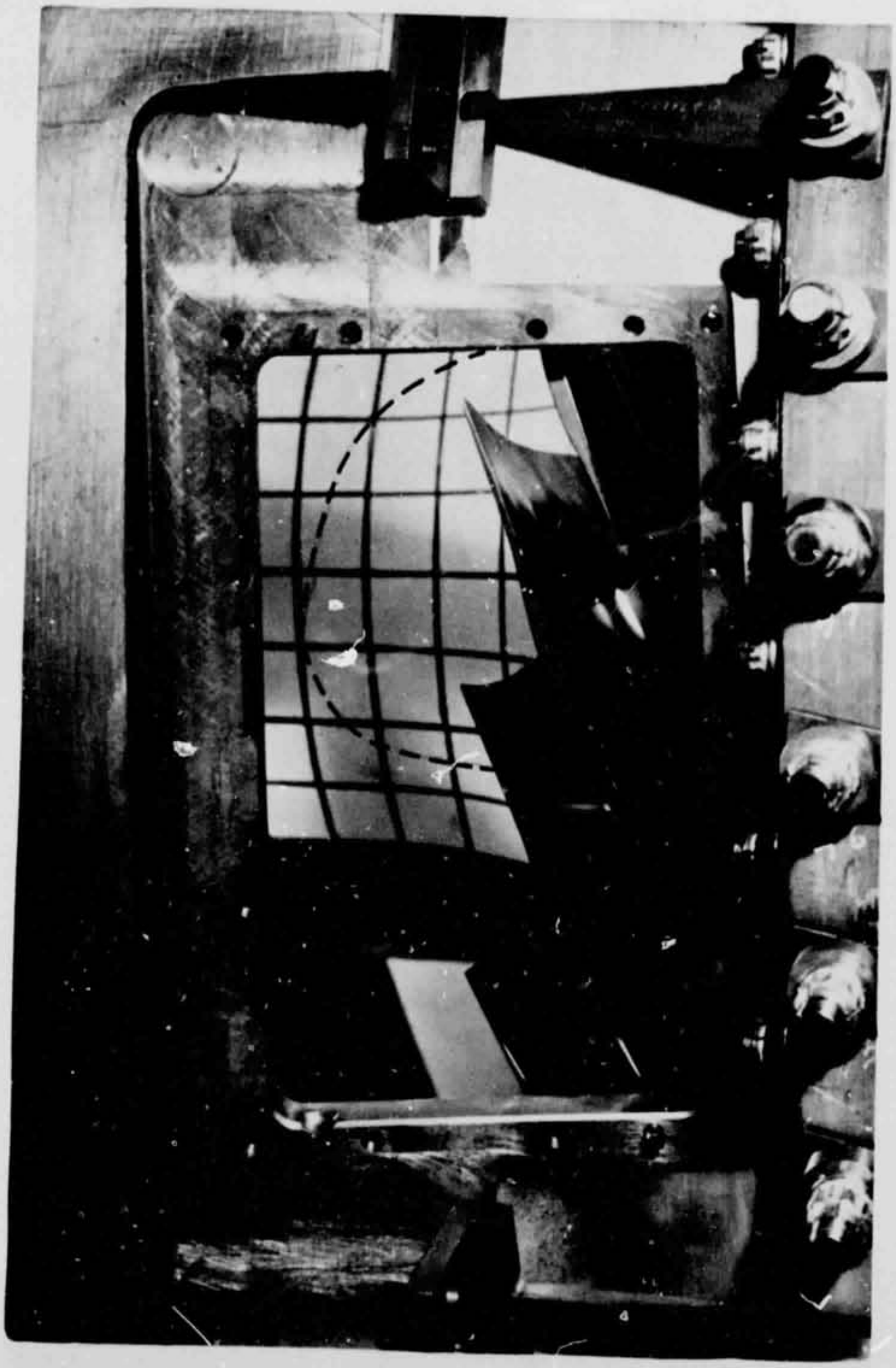

Figure 14 Interior of NASA Fan Rig as Seen Without Window in Place

Figure 15 Interior of NASA Fan Rig as Seen With Window in Place

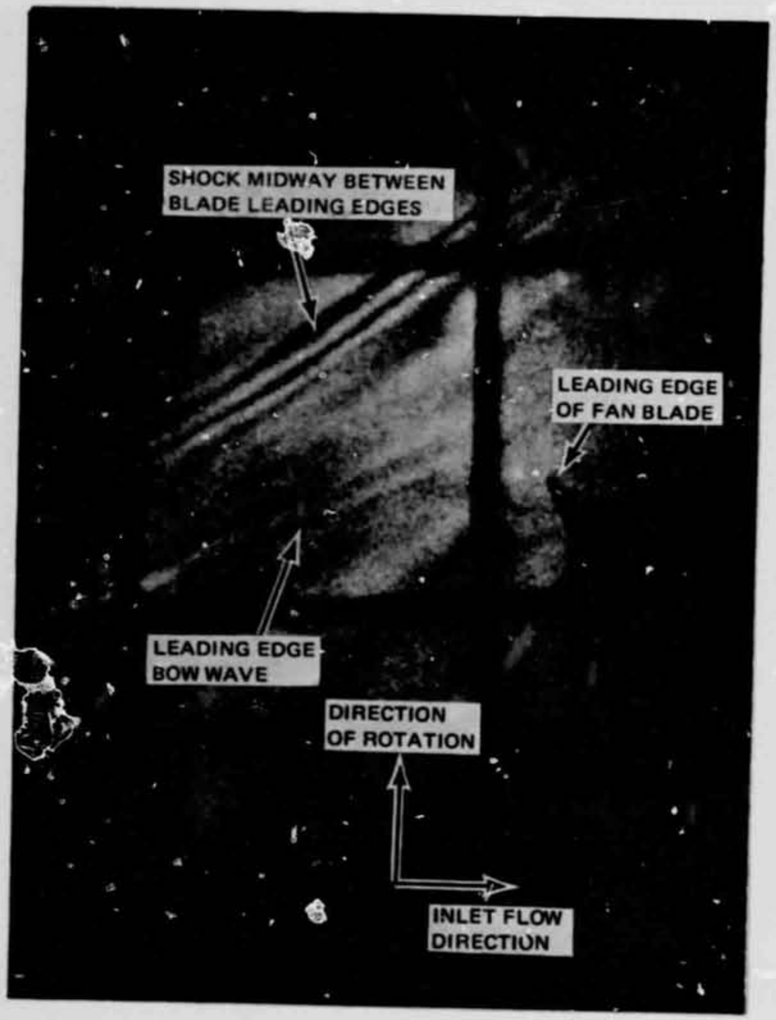

Figure 16 Photograph of Hologram #8, Taken at the 70% Speed Line, Near Stall Flow (Camera Focused Near Tip, f 5.6)

Figure 17 Photograph of Hologram #13, Taken at the 70% Speed Line, Intermediate Flow (Camera Focused Near Tip, f 11)

Figure 18a Photograph of Hologram #1, Taken at the 100% Speed Line, Maximum Flow (Camera Focused 1½" Below Tip, f 11)

Figure 18b Photograph of Hologram #1, Taken at the 100% Speed Line, Maximum Flow (Camera Focused 3" Below Tip, f 5.6)

Figure 19 Photograph of Hologram #3, Taken at the 100% Speed Line, Maximum Flow (Camera Focused 1½" Below Tip, f 11)

Figure 20a Photograph of Hologram #21, Taken at the 100% Speed Line, Near Stall Flow (Camera Focused at Tip, f 11)

Figure 20b Photograph of Hologram #21, Taken at the 100% Speed Line, Near Stall (Camera Focused 2" Below the Tip, f 11)

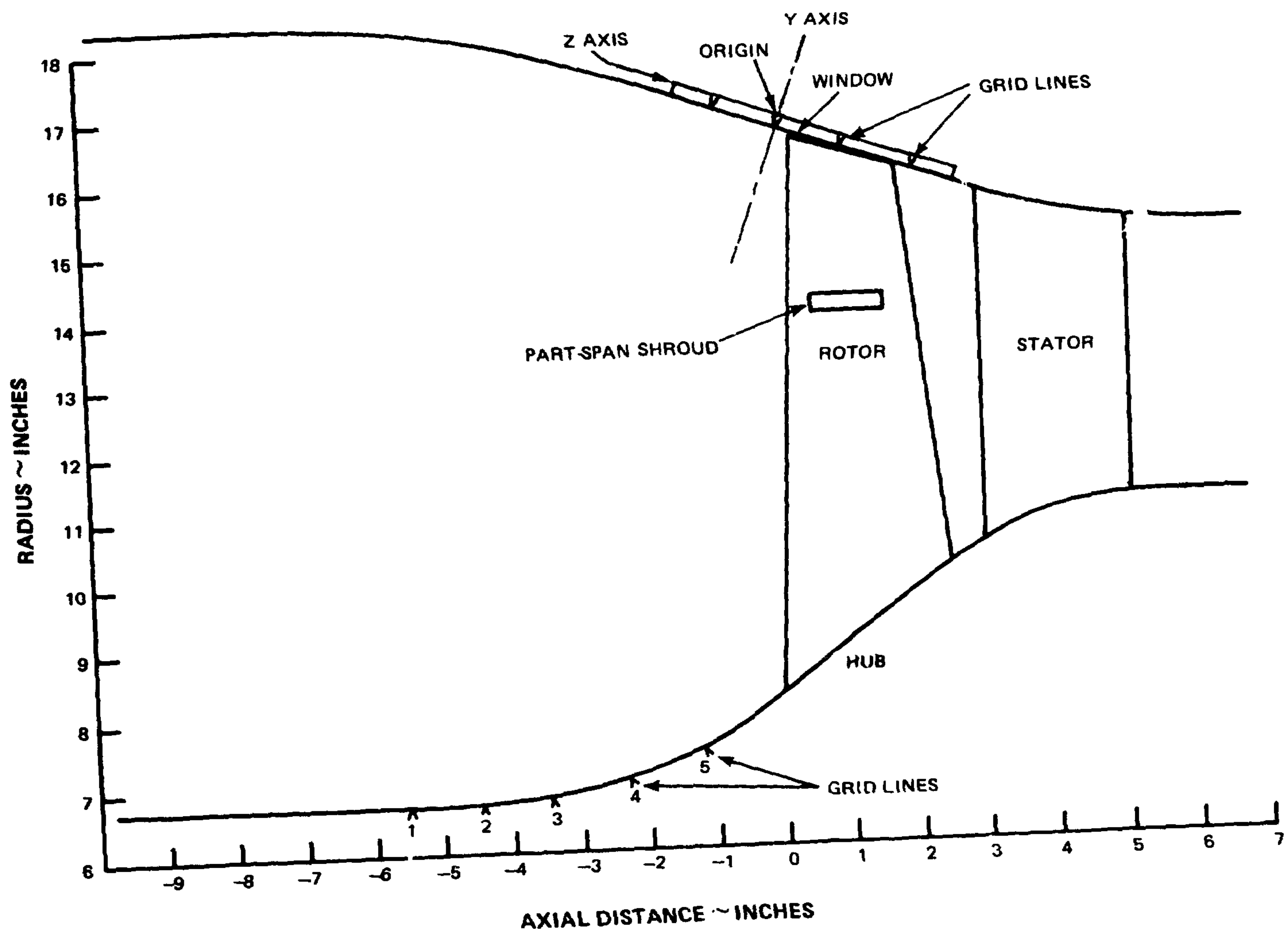

Figure 21 Meridional View of Compressor

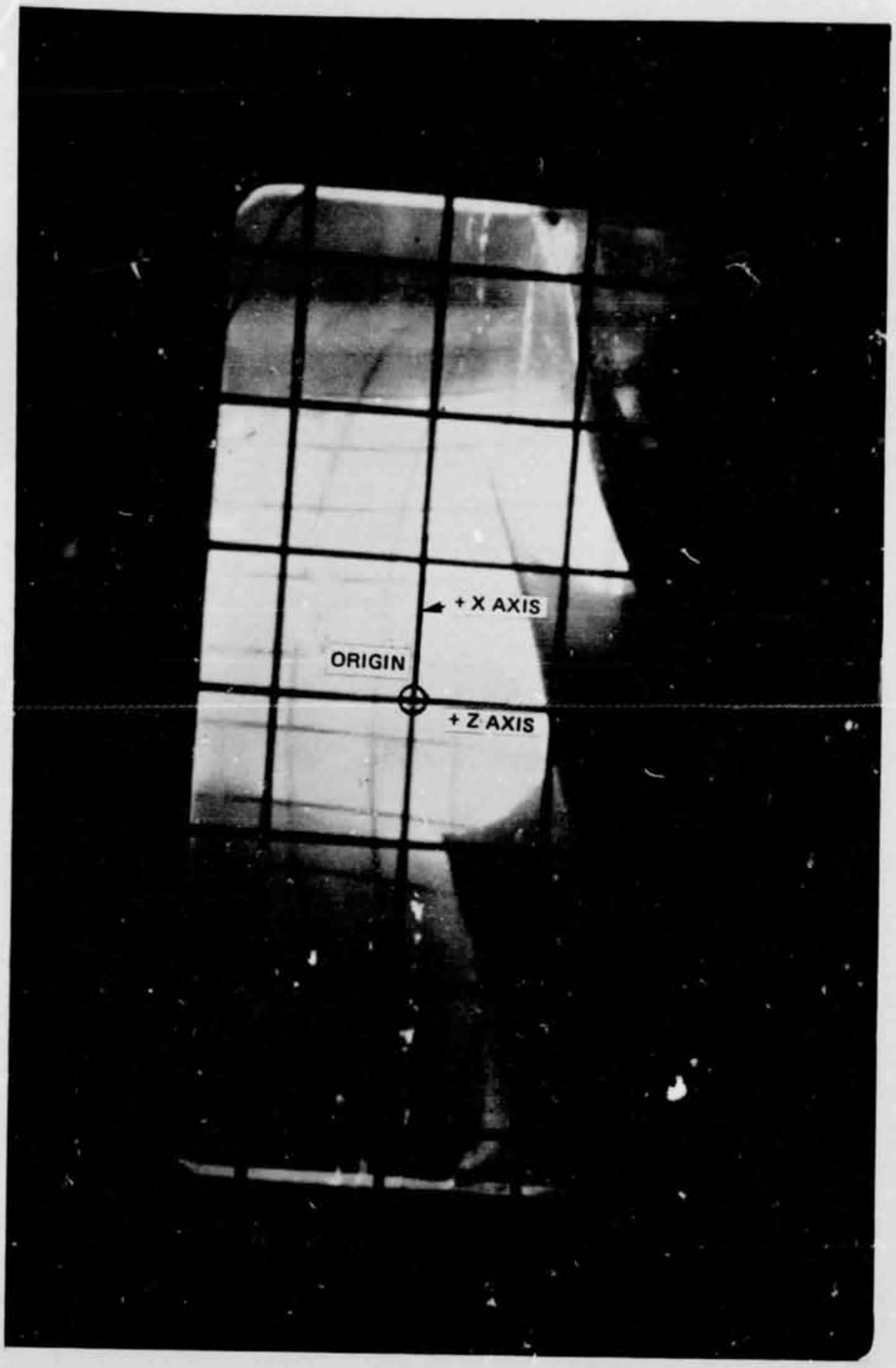

Figure 22 The X-Axis and Z-Axis as Defined on the Window

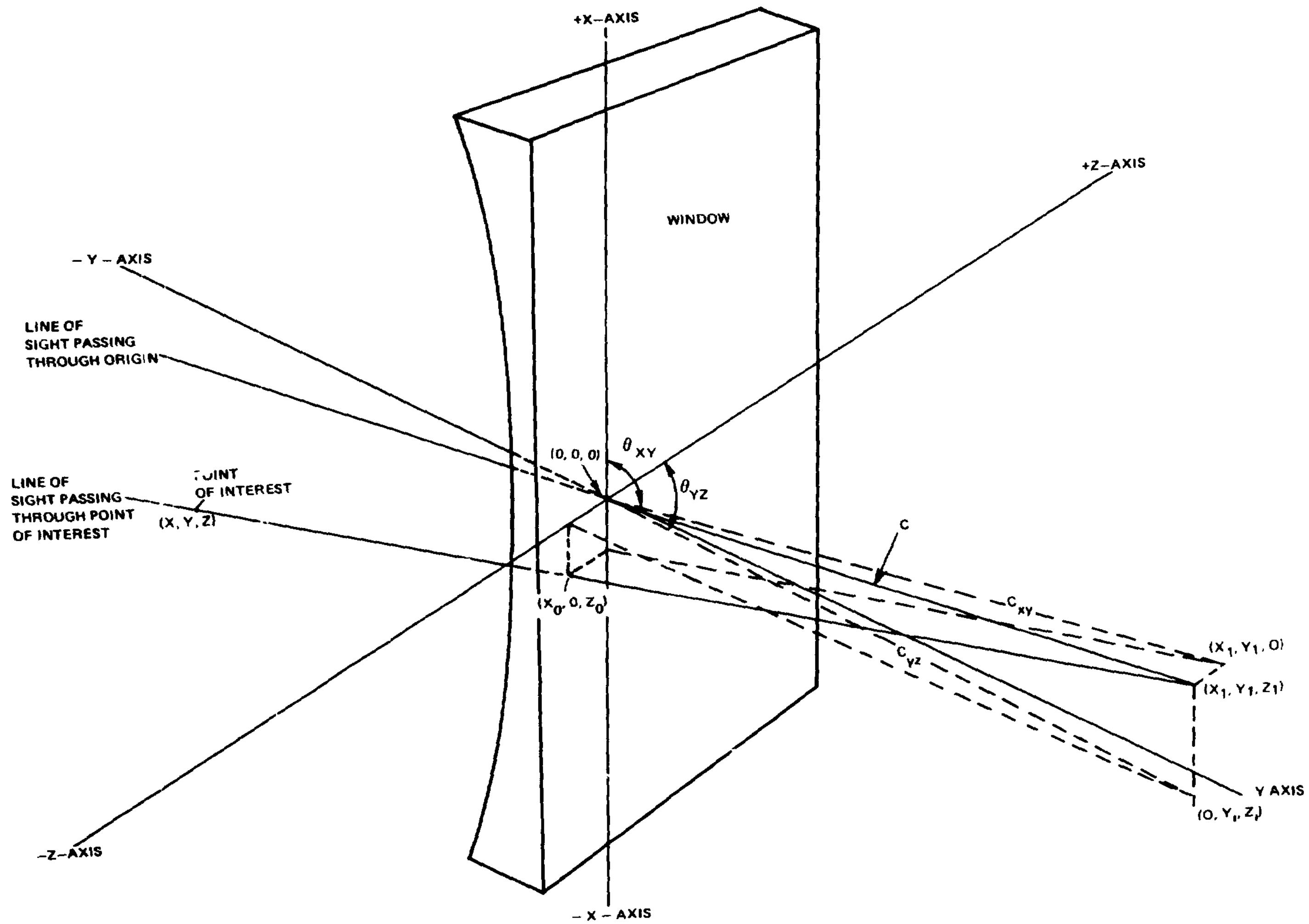

Figure 23   Coordinate System and Geometry Used in Triangulation Procedure

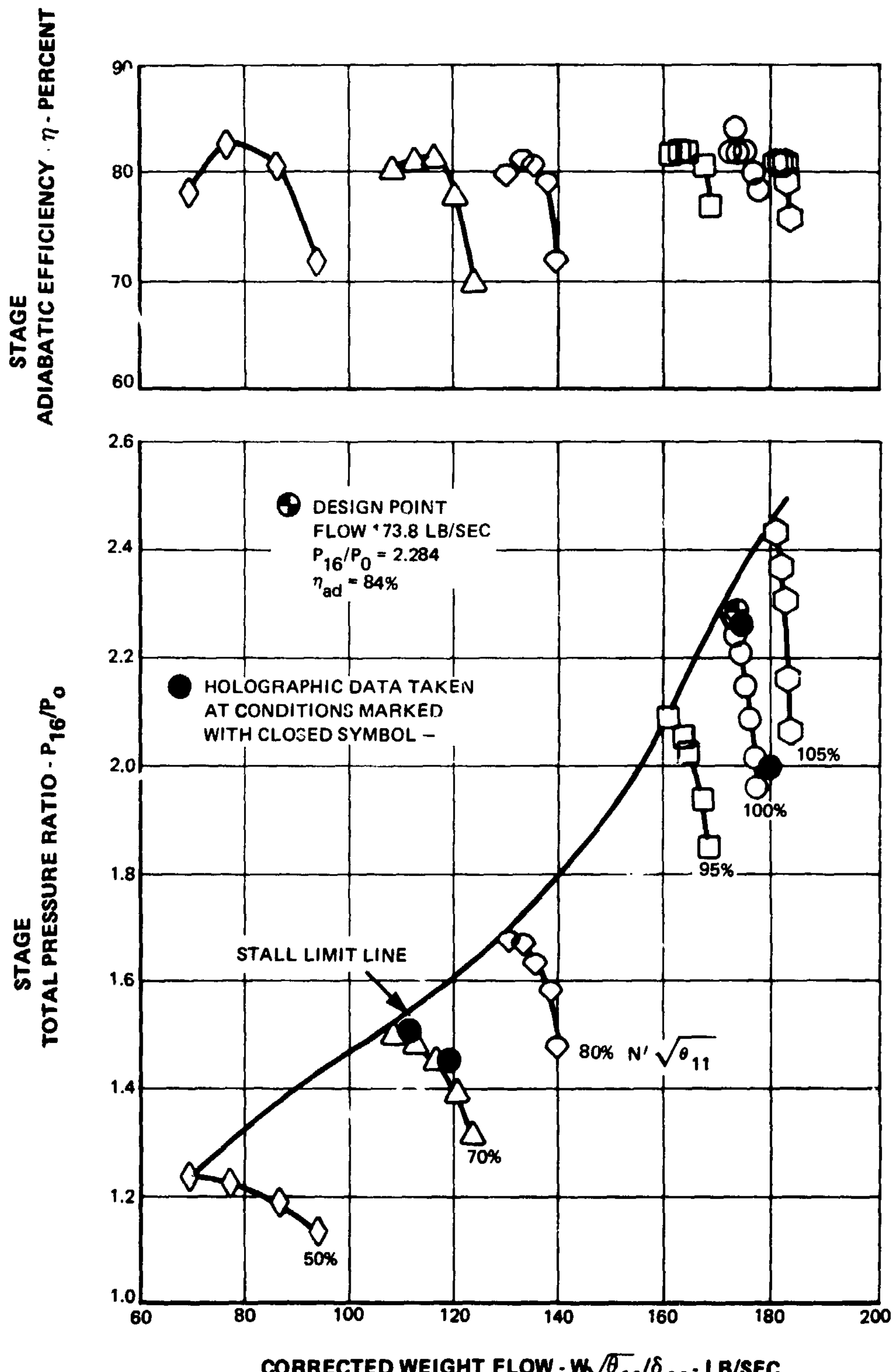

Figure 24 Stage Overall Performance with Uniform Inlet Flow

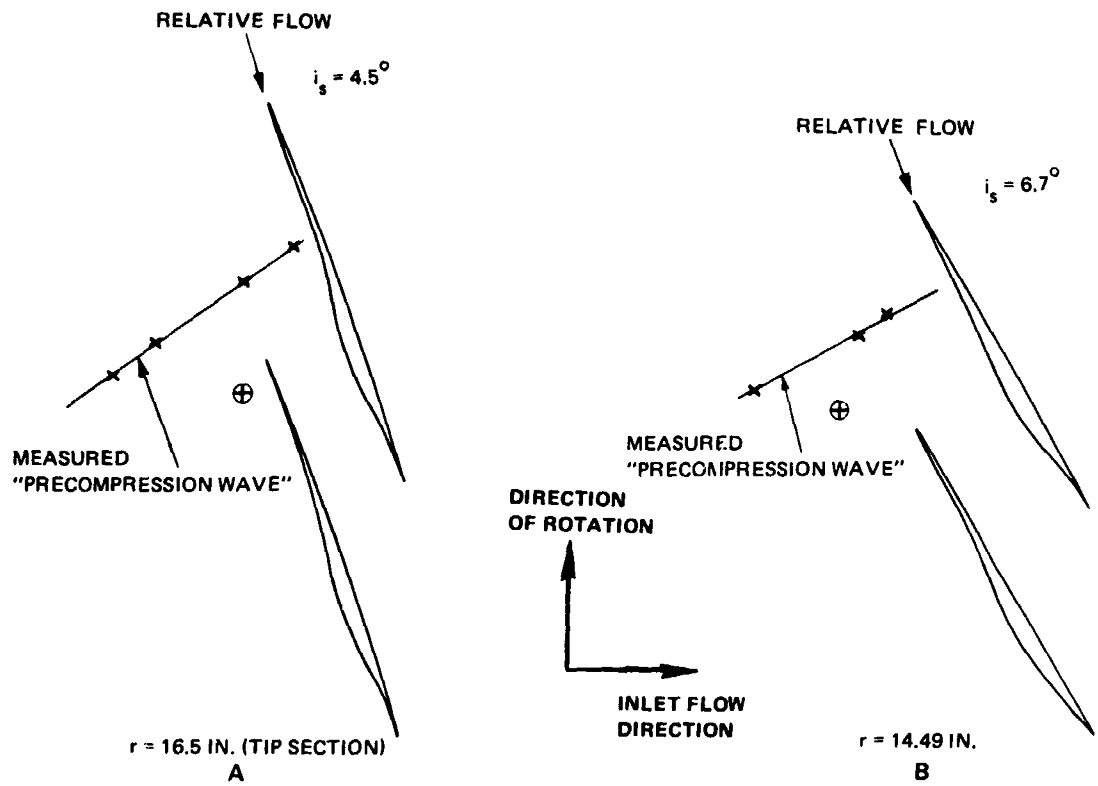

Figure 25 Rotor Shock Patterns from Hologram 8, 70% Design Speed, Near Stall Flow

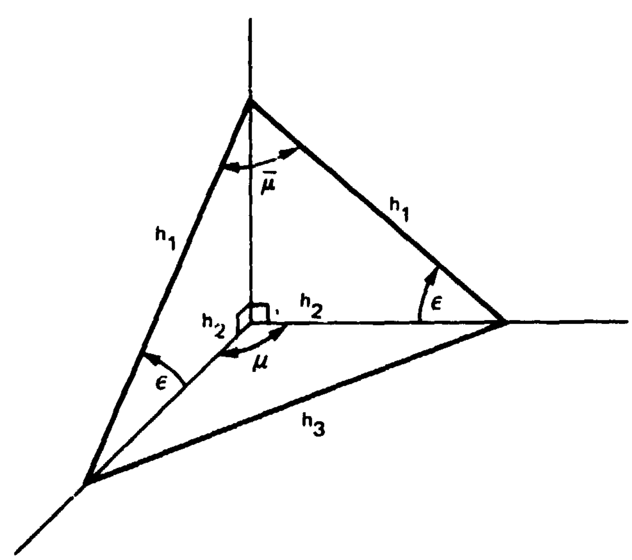

Figure 26 Projection of Included Angle from Conical to Radial Plane

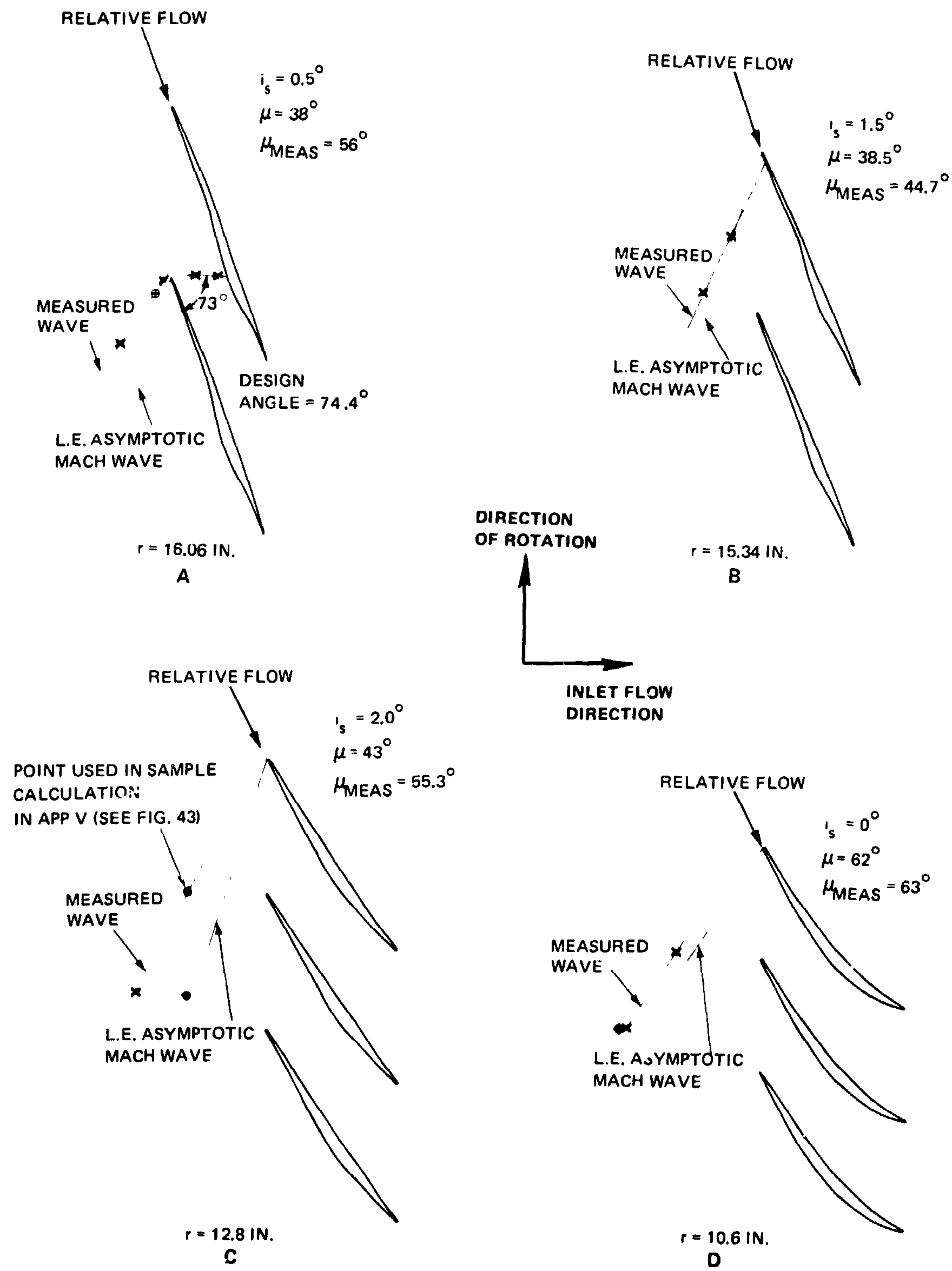

Figure 27 Rotor Shock Patterns from Hologram 21, 100% Design Speed, Near Stall Flow

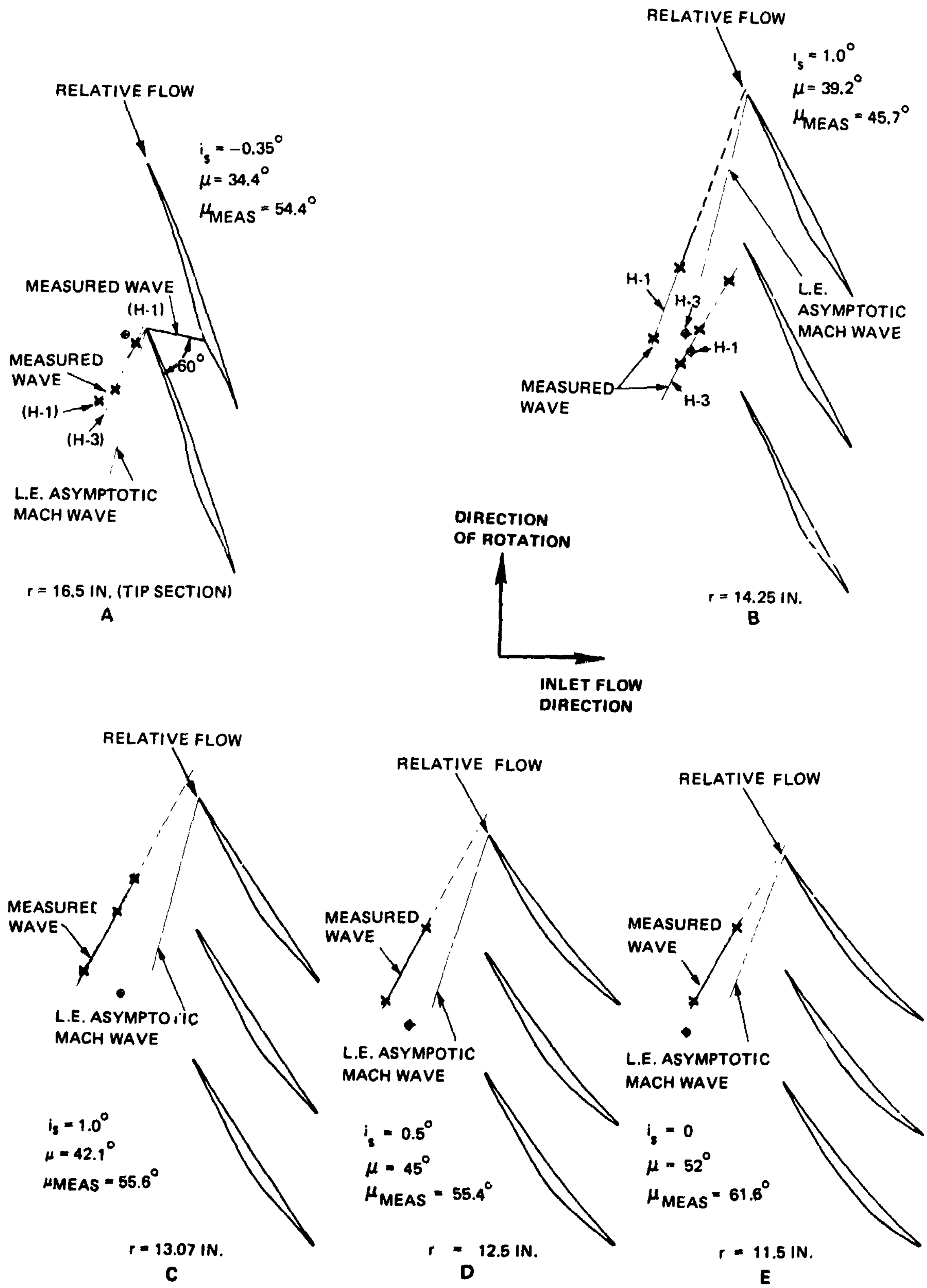

Figure 28 Rotor Sh·ck Patterns from Holograms 1 and 3,
100% D· ı Speed, Maximum Flow

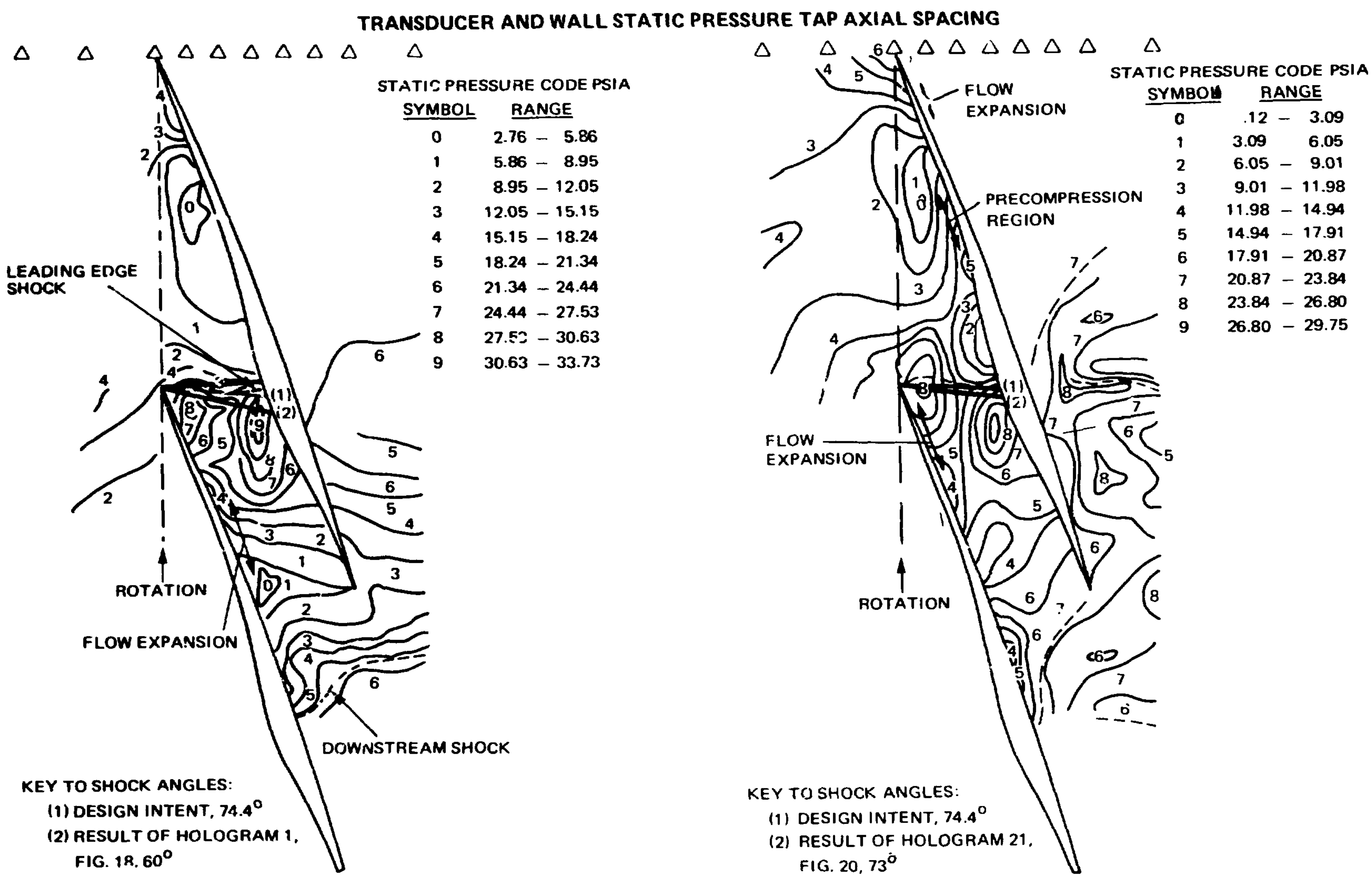

(a) Maximum Flow, $W\sqrt{\theta}/\delta$ = 177.8 lbm/sec

(b) Near Stall Flow, $W\sqrt{\theta}/\delta$ = 173.2 lbm/sec

Figure 29 Rotor Blade Tip Static Pressure Contours, 100% Speed

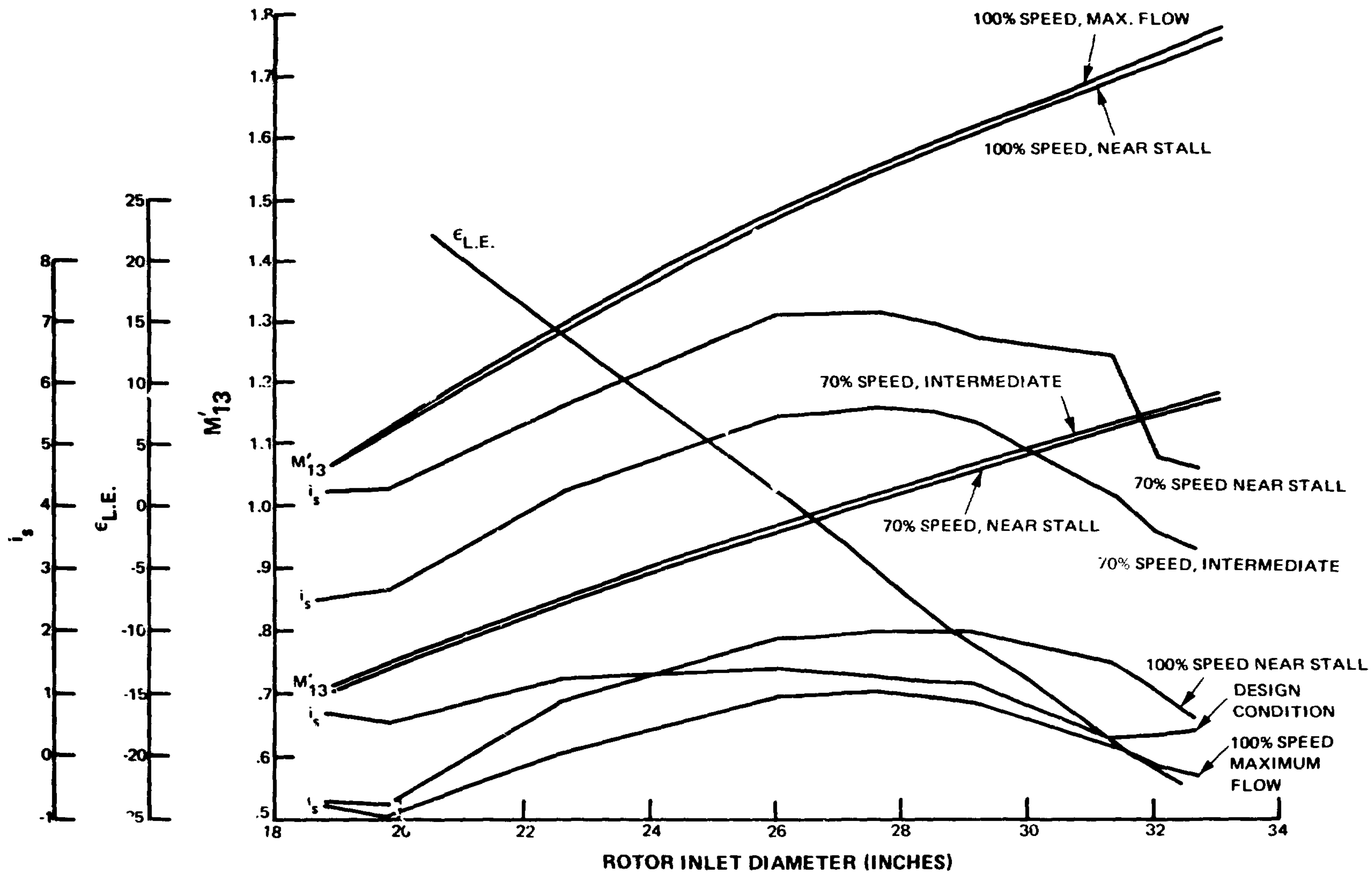

Figure 30 Rotor Leading Relative Mach Number, Incidence, and Meridional Streamline Angle

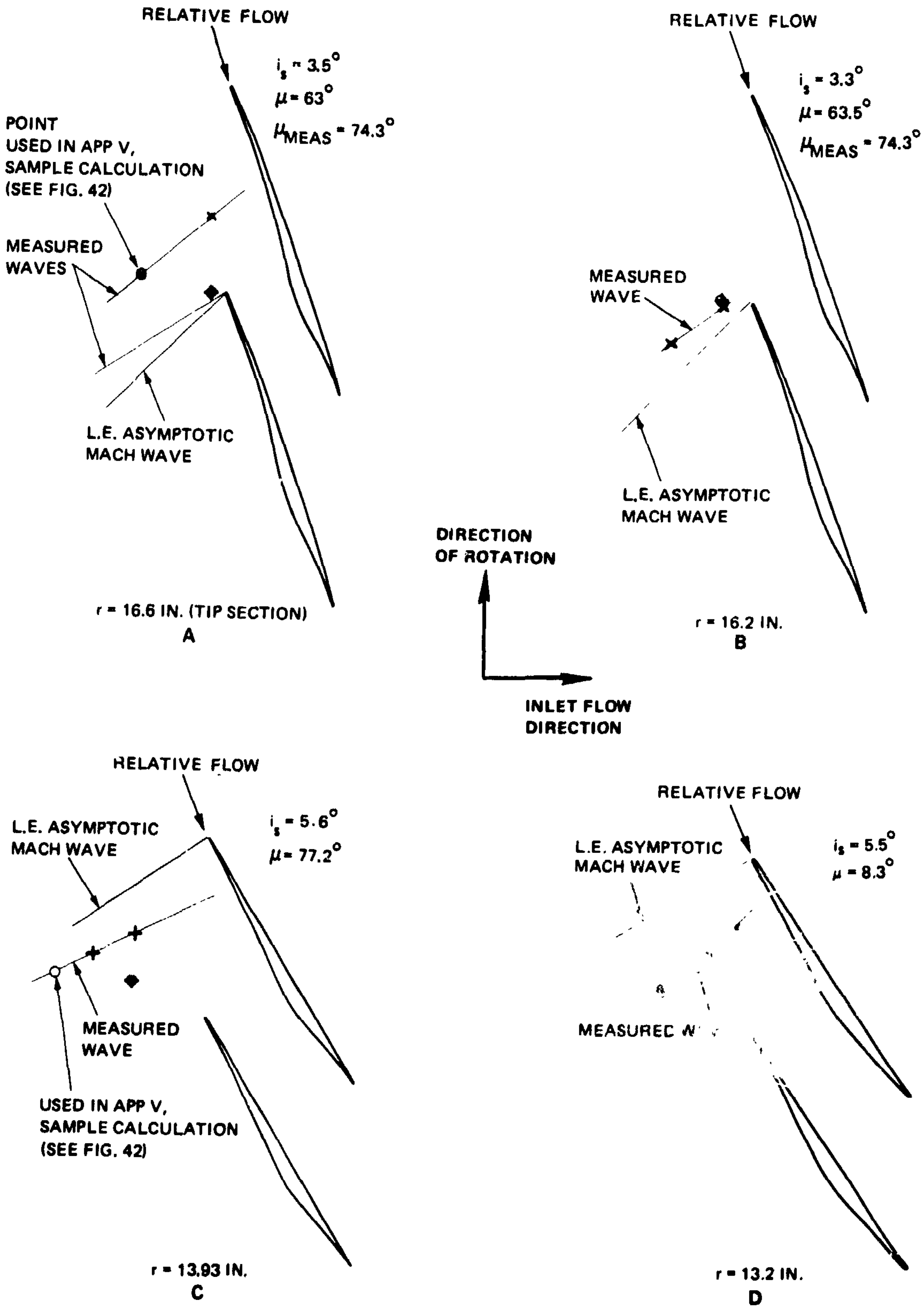

Figure 31 Rotor Shock Patterns from Hologram 13, 70% Design Speed, Intermediate Flow

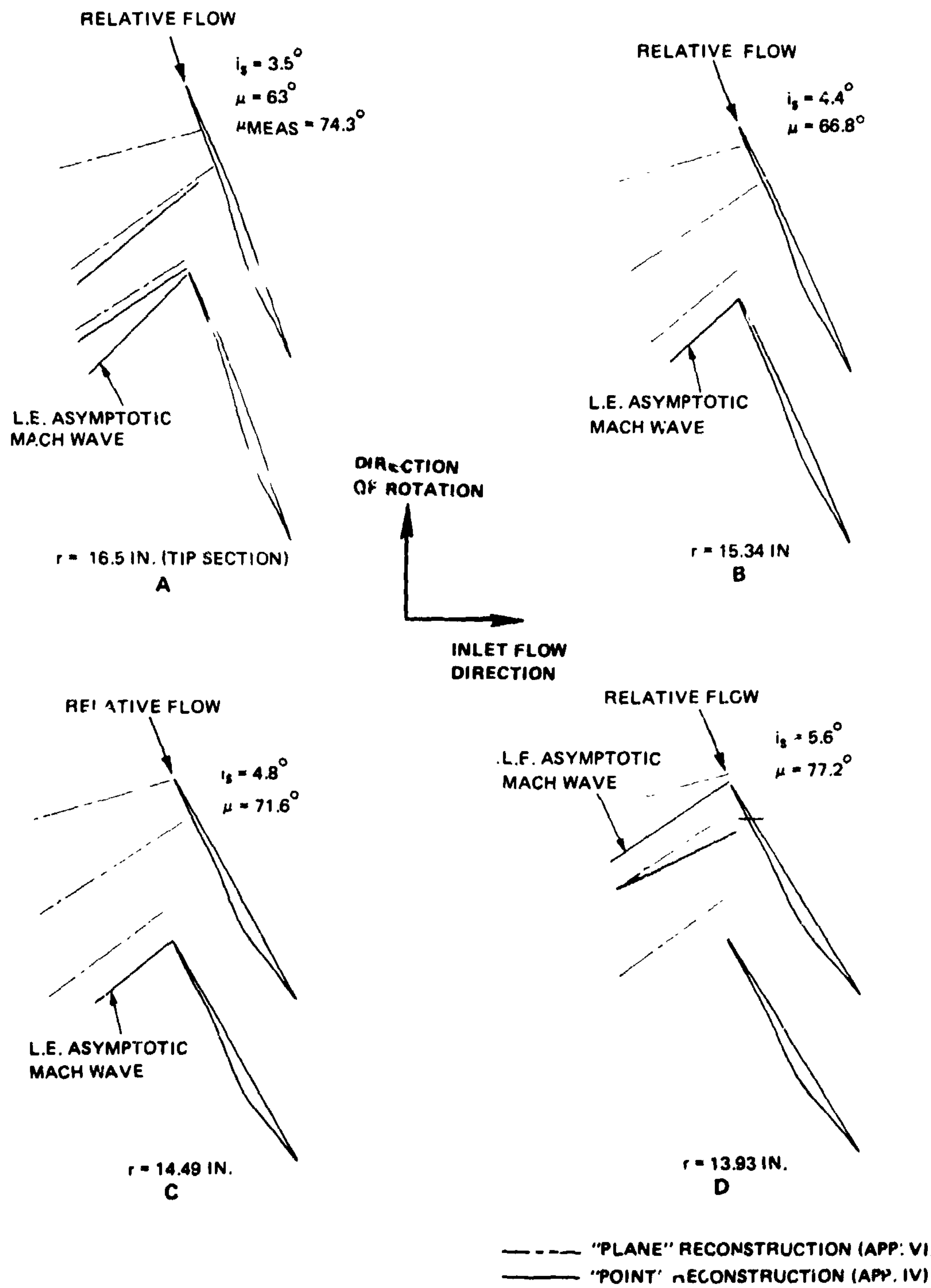

Figure 32 Rotor Shock Patterns from Hologram 13, 70% Design Speed, Intermediate Flow

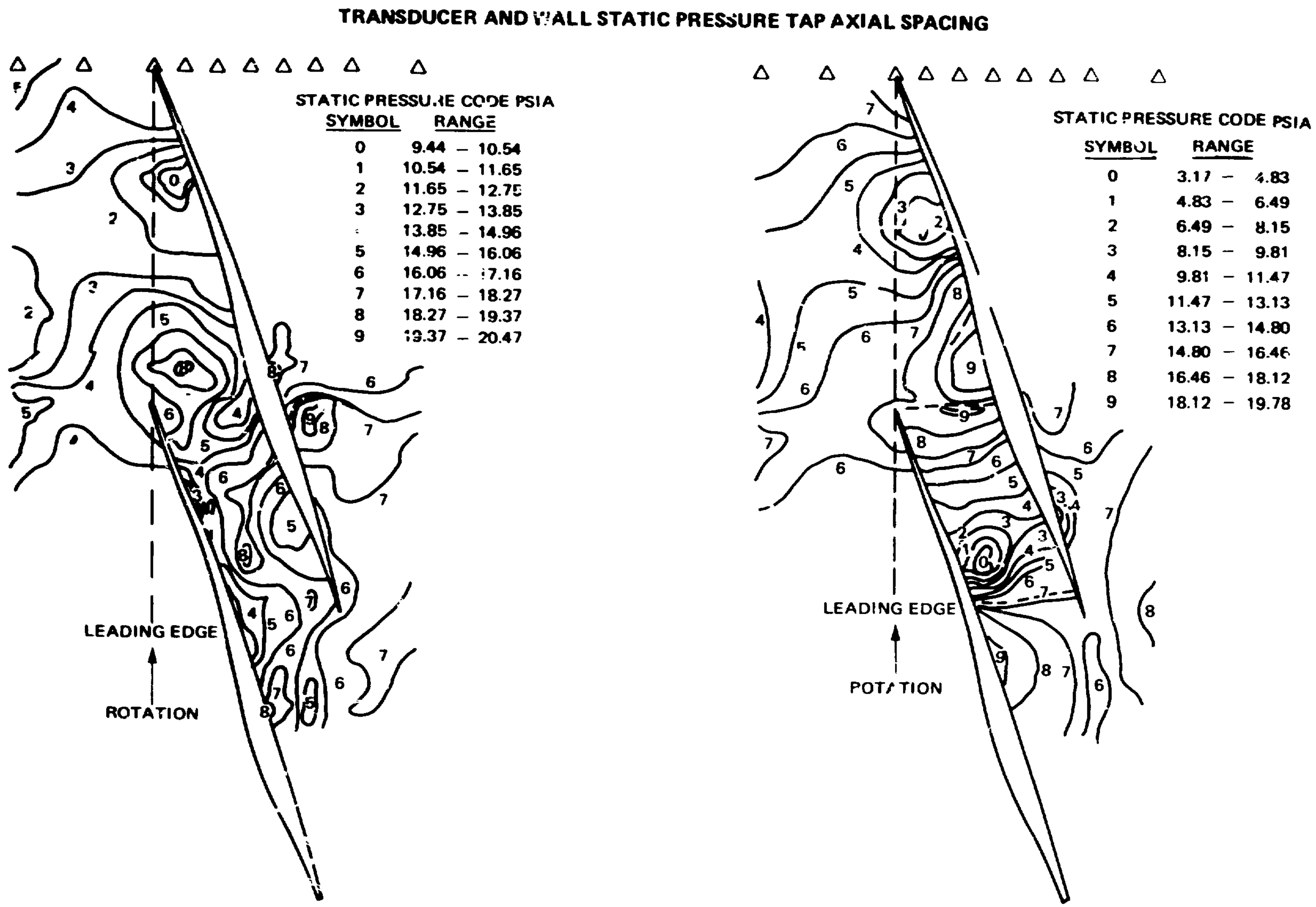

(a) Near Stall Flow, $W\sqrt{\theta}/\delta$ = 108.9 lbm/sec

(b) Intermediate Flow, $W\sqrt{\theta}/\delta$ = 120.8 lbm/sec

Figure 33 Rotor Blade Tip Static Pressure Contours, 70% Speed

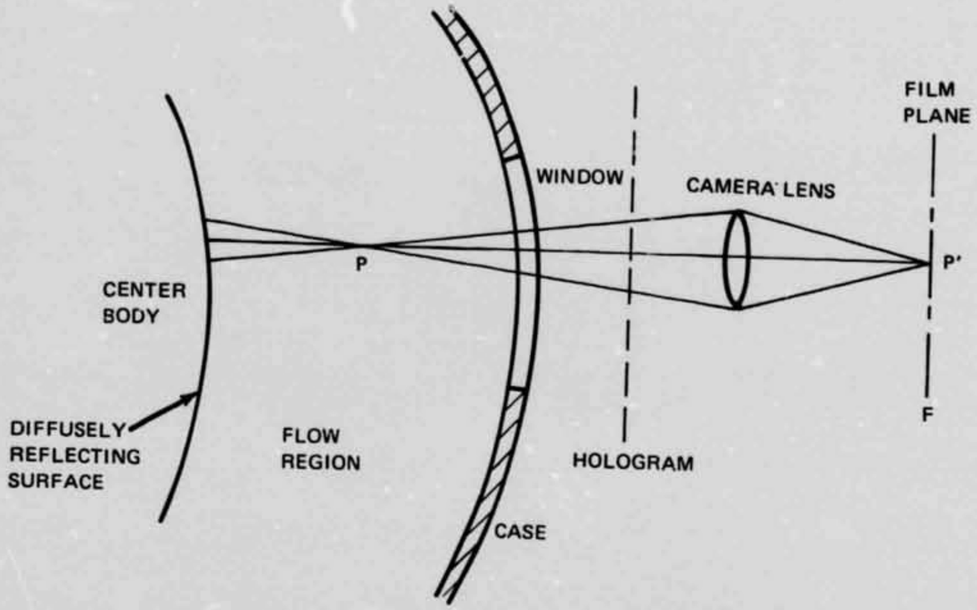

Figure 34 Simplified Diagram of Holographic Reconstruction of the Test Section

Figure 35 Picture of a Holographic Interferogram of a Flame

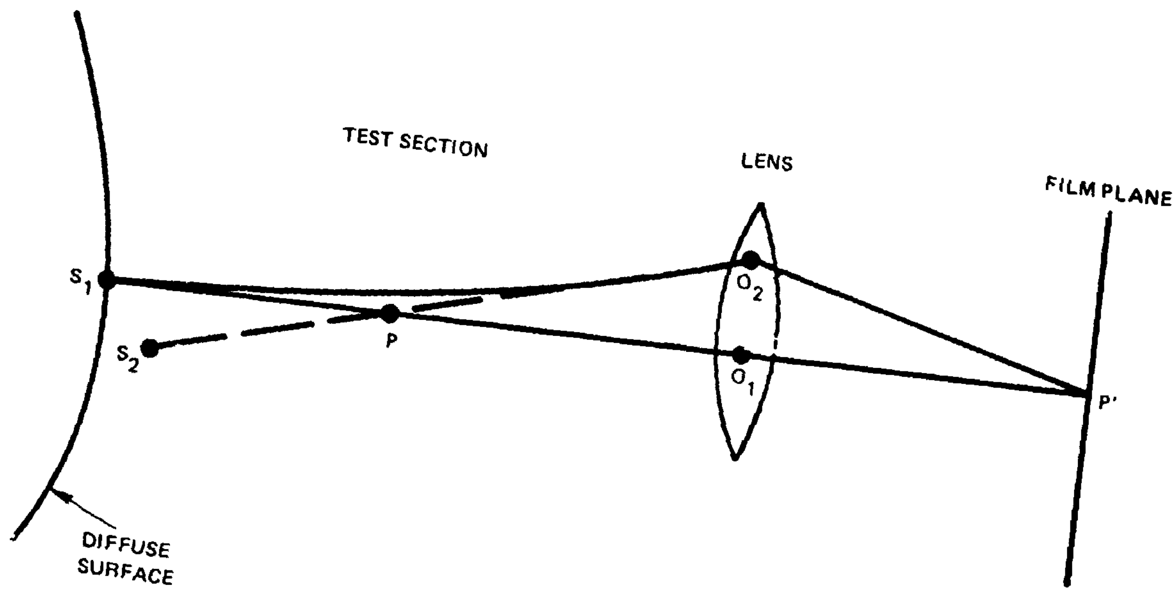

Figure 36 Ray Diagram

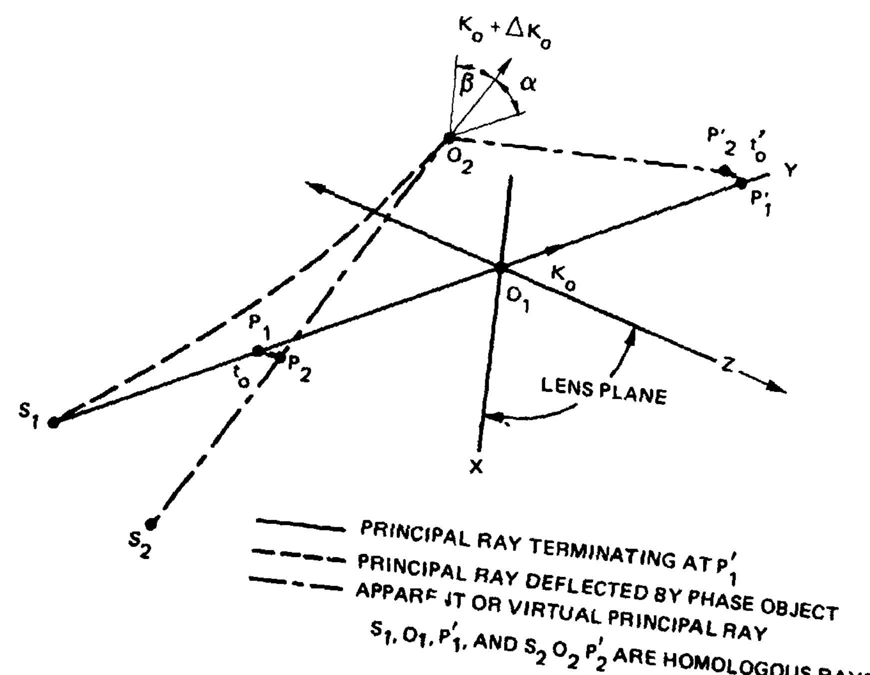

Figure 37 Principal Homologous Ray Diagram

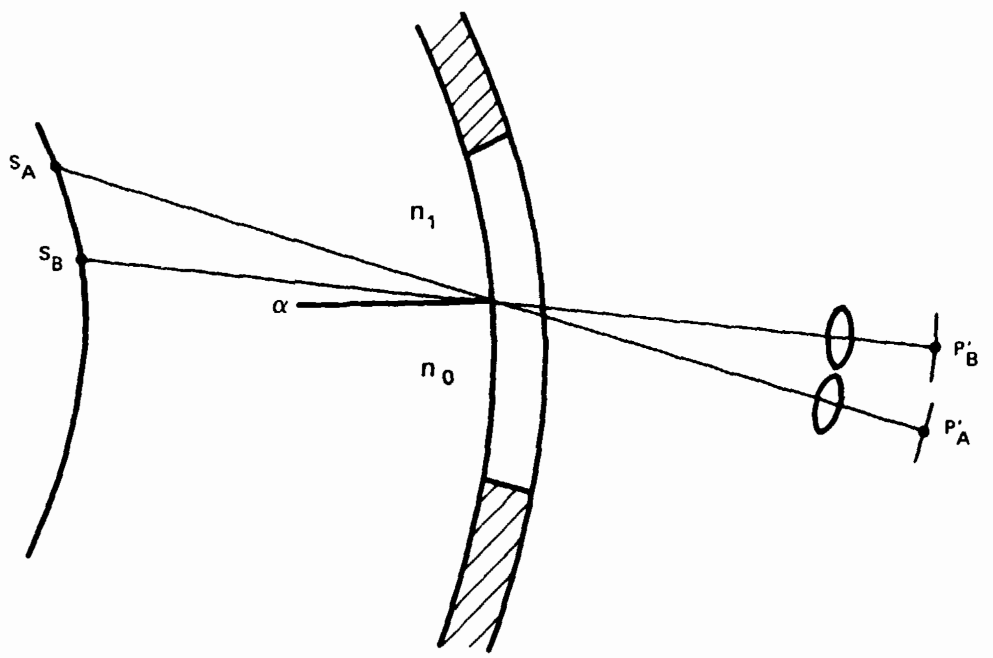

Figure 38 Central Rays for Two Views Through the Tip of a Shock

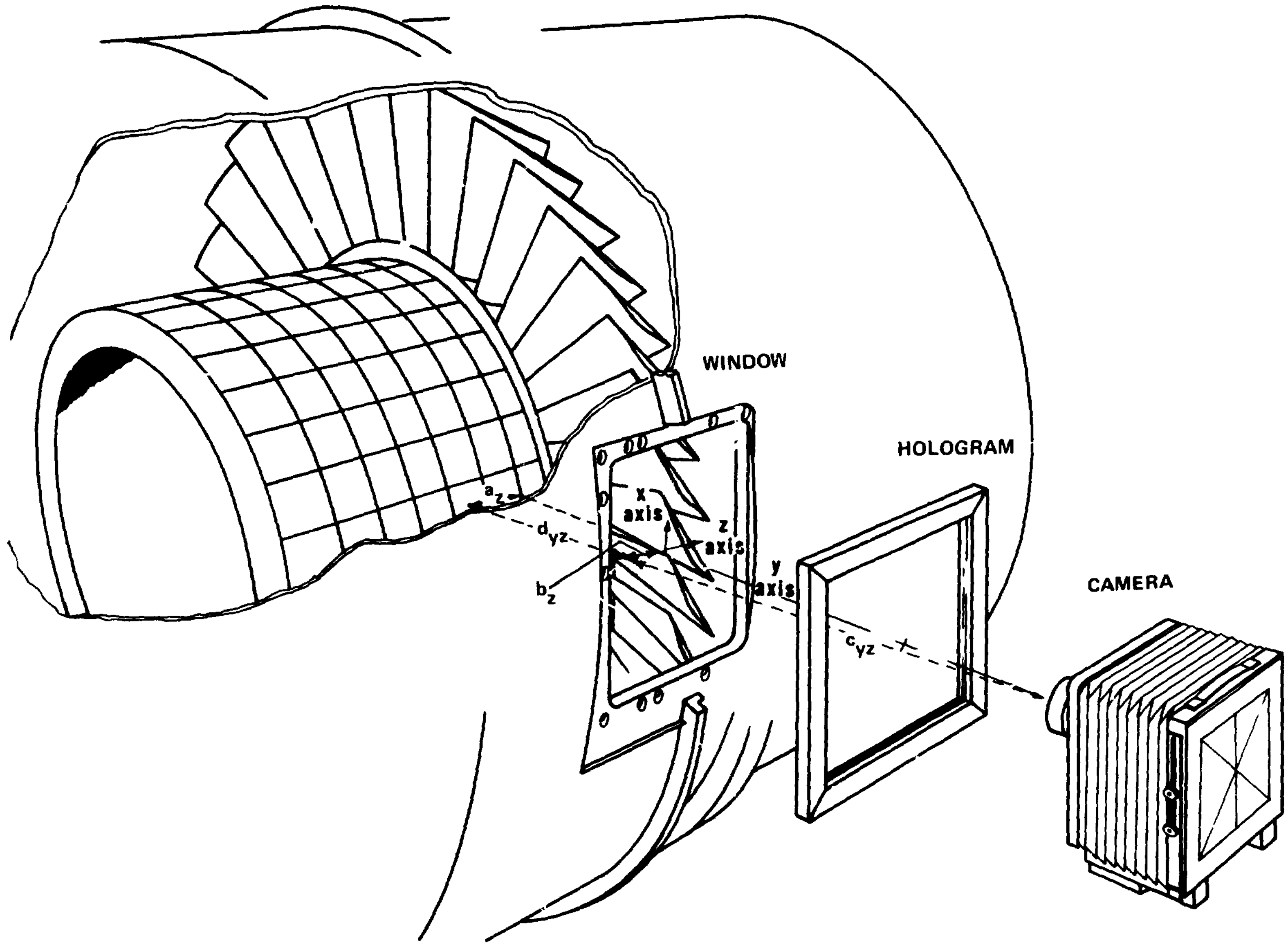

Figure 39 Relative Positions of the Rig Window, Hologram, and Recording Camera; Geometric Relations of the Length Parameters (Appendix IV)

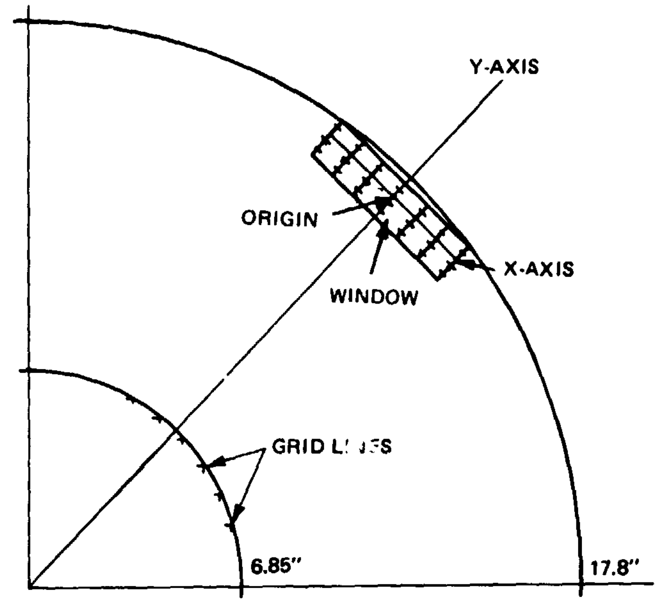

CROSS-SECTION CORRESPONDING TO GRID LINE 3, FIG. 21
FIGURE 40A

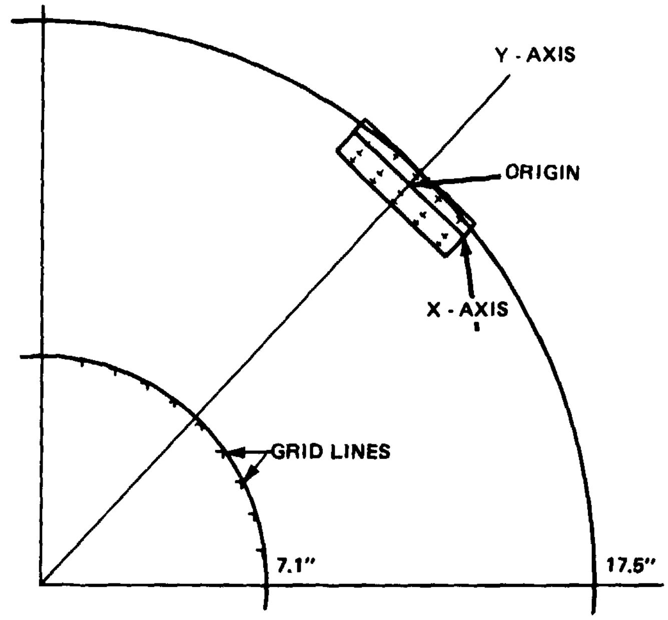

CROSS-SECTION CORRESPONDING TO GRID LINE 4, FIG. 21
FIGURE 40B

Figure 40 NASA Fan Rig, View Along Axis of Rotation

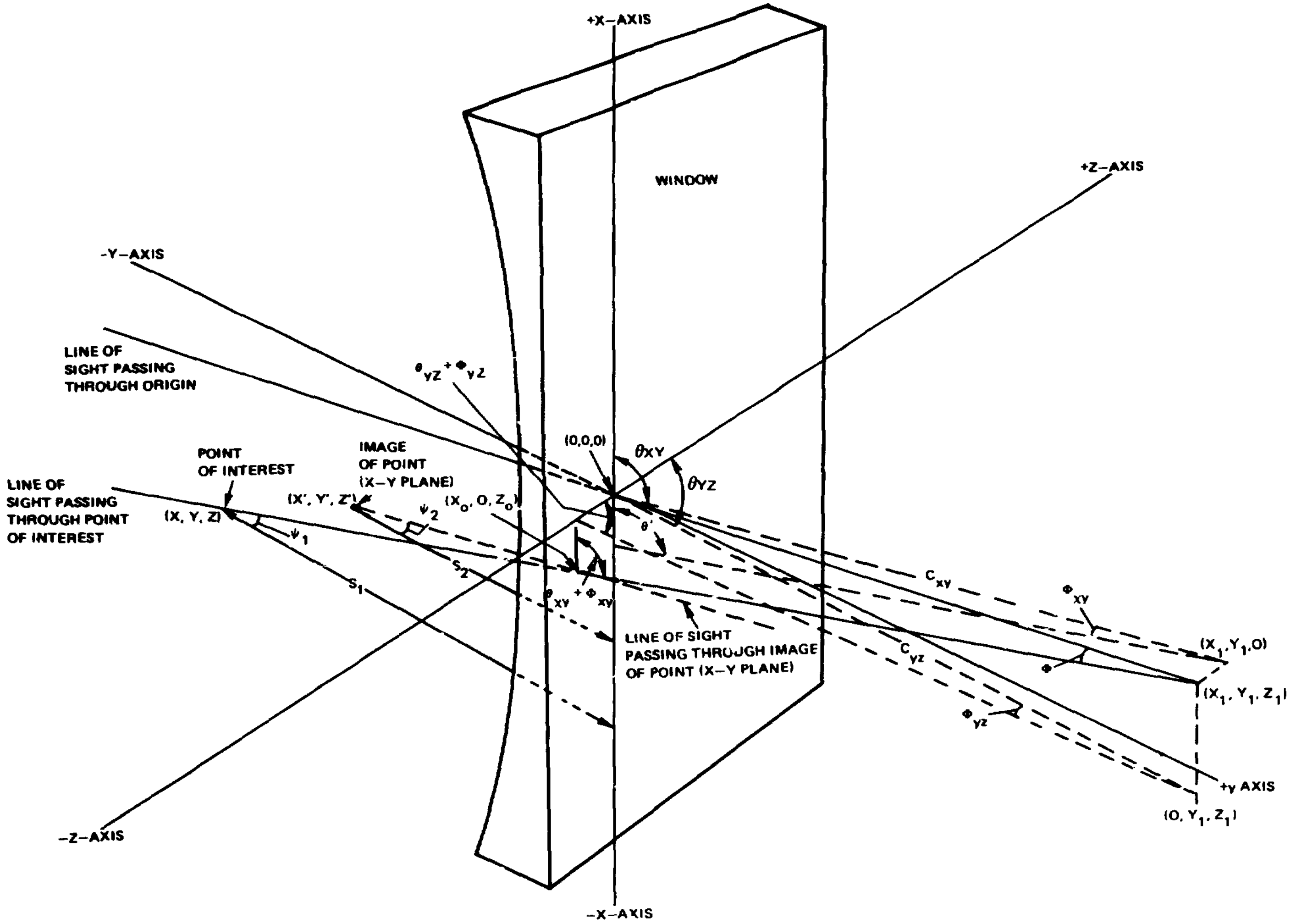

Figure 41 Coordinate System and Geometry Used in the Determination of the Triangulation Equations

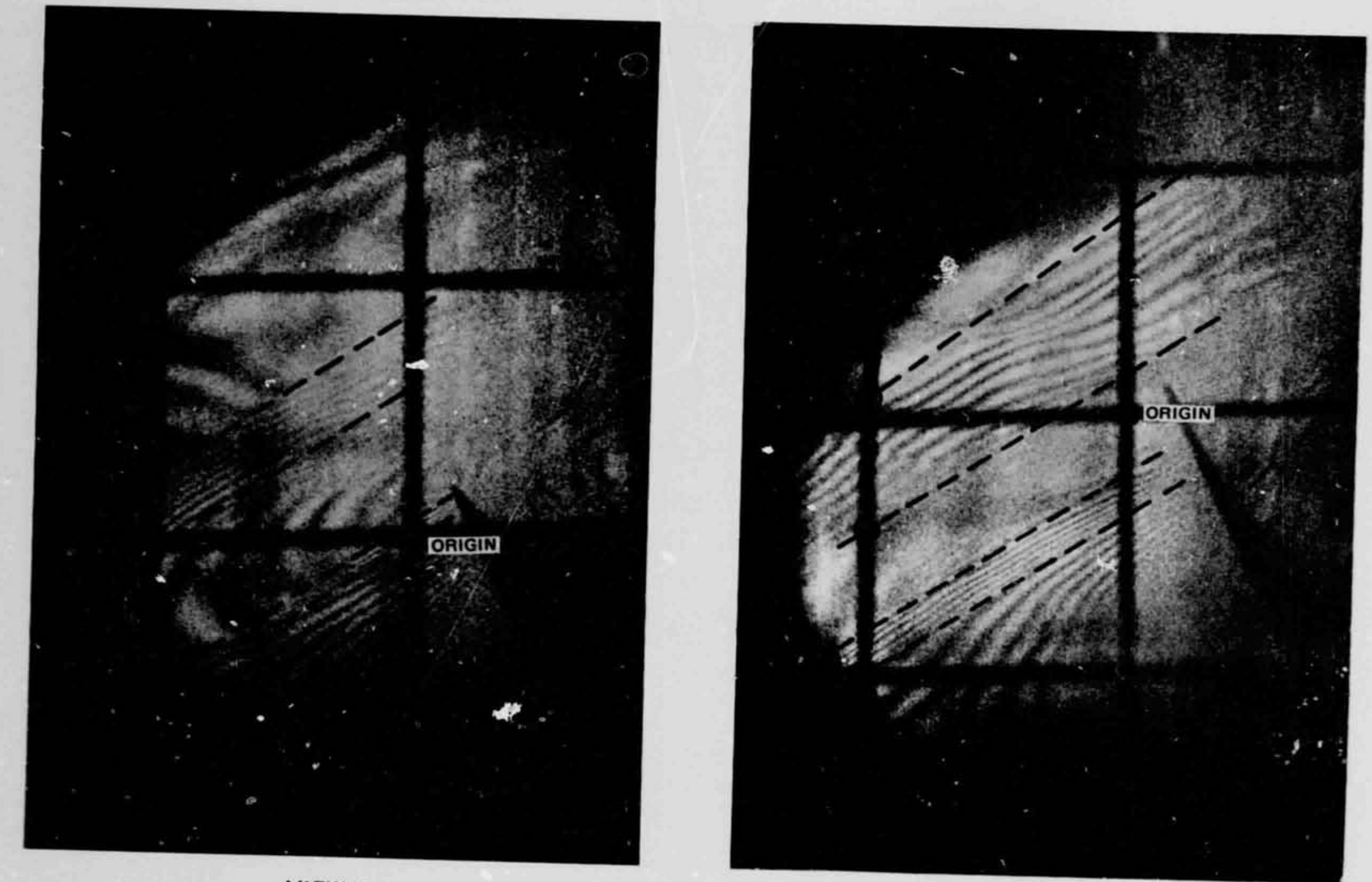

VIEW A

VIEW B

Figure 42 Photograph of Hologram #13, Taken at the 70% Speed Line, Intermediate Flow

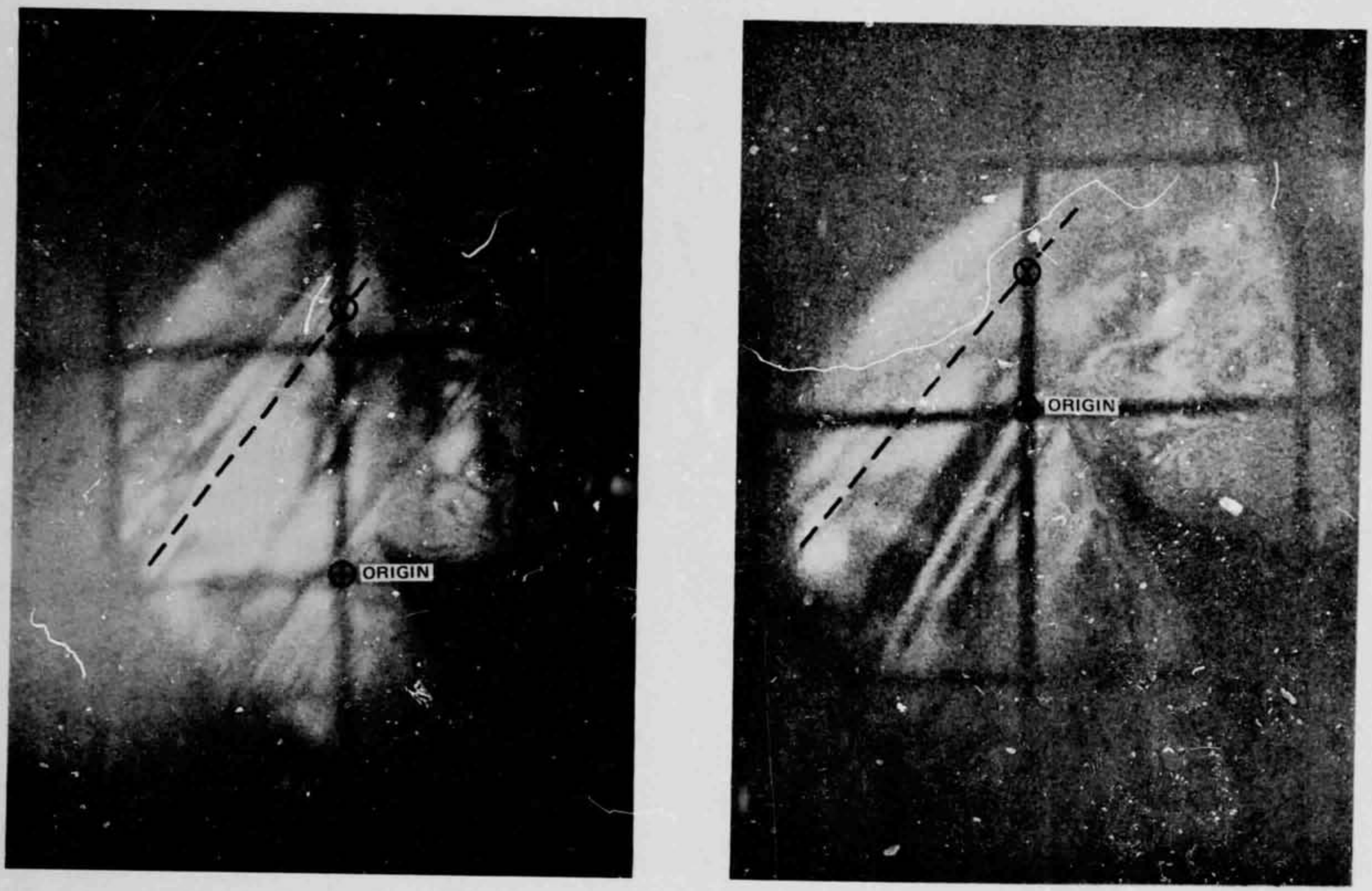

VIEW A

VIEW B

Figure 43 Photograph of Hologram #21, Taken at the 100% Speed Line, Near Stall Flow

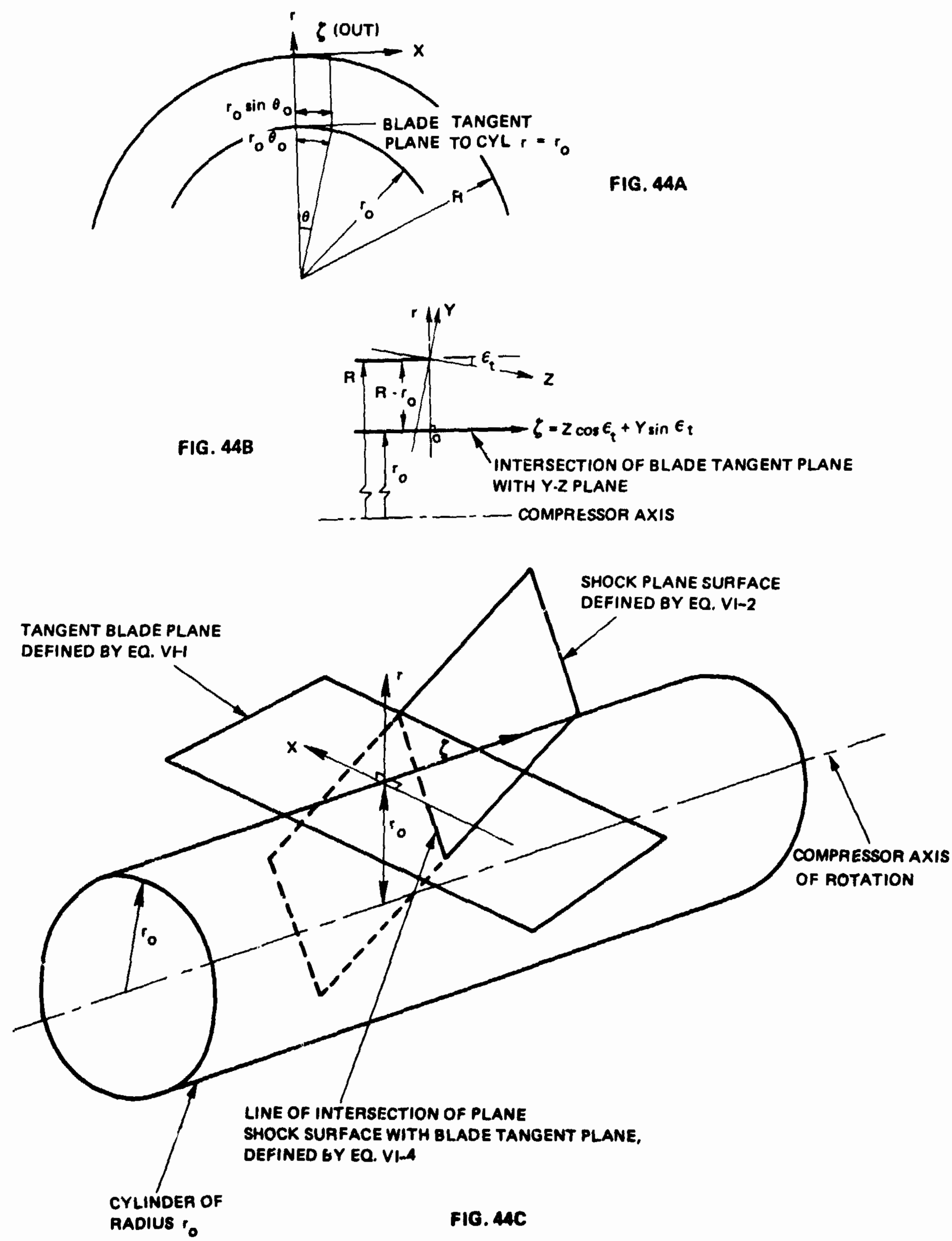

Figure 44 Geometry Used for Plane Reconstruction of Shock Waves from the Holographic Analysis